IMAGE ANALYSIS ON HYPERSPECTRAL CORNEAL EPITHELIUM INJURIES USING A NEW IMAGE ENHANCEMENT AND A NOVEL MIXING KERNEL

By

Siti Salwa Binti Md Noor

In the fulfilment of the requirement
for the degree of Doctor of Philosophy

Centre for Signal & Image Processing
Department of Electronic & Electrical Engineering
University of Strathclyde

Supervised By
Professor Stephen Marshall
Doctor Jinchang Ren

June 2019

DECLARATION AND COPYRIGHT

This thesis is the result of the author's original research. It has been composed by the author and has not been previously submitted for examination which has led to the award of a degree.

Signed:

Date: 5/06/2019

ACKNOWLEDGEMENTS

PhD is a long journey which cannot be completed without the help and support of others. Hence, there are a number of people that I would like to thank for their support throughout the duration of my studies.

For me, there are no enough words that can express my gratitude to everyone who have directly and indirectly contributed to the completion of this thesis. First, I would like to express my deepest gratitude to my supervisors, Prof. Stephen Marshall and Dr. Jinchang Ren. Prof. Steve was the first person who responded to my PhD application to become a student at the University of Strathclyde. He spared his time to listen and attend to me whenever necessary despite his heavy commitments. The moral support he extended to me is without doubt a boost that helped me to build and write this research work. Most importantly, Steve was always understanding and supportive by guiding me to overcome the hurdles I had to face throughout my study time in both academic and life matters.

My special thanks are meant for all the staffs at the German Malaysian Institute who directly or indirectly supported me and helped me in every way possible. My deepest gratitude is extended to many people who have helped me, especially to Syed Nizam Syed Idris as the head of section, Jamilah Mohamad Ali as the head of department, Fuznim Abd Ghaffar from the human resources, and to all my friends and colleagues.

I would like to gratefully acknowledge the financial sponsorship provided by Majlis Amanah Rakyat (MARA) located in Kuala Lumpur and London for their support throughout my study.

I am also indebted to both individuals who work at Glasgow Centre for Ophthalmic Research, Gartnavel General Hospital, Glasgow. The first one is Dr. Stuart Park who was full of advice and made my research journey possible. My sincere heartfelt goes to Dr. Kaleena Michael who had been acting as my research partner for her kindness, sincerity, and encouragement which have excellently facilitated the successful completion of my work.

A special thanks goes to Julius Tschannerl who introduced and trained me on how to use the hyperspectral imaging system in the lab. Thanks for being very committed in sharing your knowledge and never get tired of assisting me.

On a more personal note, my loving gratitude goes to my family. First and foremost, no words can ever describe how grateful I am towards my beloved husband Azizan Abu who always wiped my tears and encouraged me to strive for the best in life. His endless patience, support, and sacrifices throughout this wonderful journey has made me believe in my ability, especially when I doubt it myself. Not to forget, I cannot thank my mother Hasnah Abdul Kadir enough for her continuous prayers, understanding, and endurance as well as the constant inspiration given by my late father Md Noor Tahir. I am forever grateful to my parents in-law Abu Jamel and Inon Sulaiman, my family members, and last but not least to both of my sons, Tarmizi and Haikal. A sincere thank you from my heart for all of you.

Finally, I would like to thank all of my friends at the University of Strathclyde, the academic and non-academic person, and my Malaysian friends all over Glasgow, Scotland. THANK YOU.

ABSTRACT

The work presented in this thesis is to improve the evaluation of corneal injuries with the aim of eliminating the application of eye stains. In the case of this study, a new algorithm of image enhancement, mixture deep learning classification, and a novel mixing kernel for support vector machine are proposed to provide objective measurements. The proposed algorithms of image enhancement and the mixing kernel in this study are to provide a new contribution to knowledge in the field of ophthalmology and machine learning.

To the authors’ knowledge, this is the first analysis of 25 corneal epithelium of porcine eyes using hyperspectral imaging combined with image processing algorithm. In addition, four series of experiments on the cornea were carried out with and without eye staining through the HSI scanning method. The analysis mainly focused on the eyes without staining, while the stained eyes were used as the ground truth images for the purpose of identifying the injured area.

In this study, a new 8-Step Hyperspectral Image Enhancement (8-SHIE) was developed to differentiate the injured and healthy corneas. The results showed that the proposed algorithm was able to clearly highlight the boundary of the injury. This algorithm was further tested on the existing remote-sensing Indian Pines dataset in order to ascertain that it can work well with other hyperspectral images. Moreover, the algorithm can also be used to monitor the cornea healing process considering that the injured boundary can be viewed from band-to-band. Overall, it can be concluded that this algorithm is able to successfully separates the ten varying classes despite its main purpose of distinguishing the two classes. All the enhanced images are then classified using mixture deep-learning technique.

This study also introduced a novel design of mixing kernels (3-ConvSvm) for binary classification in support vector machine classifier. Three standard kernels, namely RBF, polynomial, and RQK are combined in order to provide more learning flexibility due to the various parameters setting. The algorithms proposed aim to minimise the generalisation error during the classification when one or more parameters is tuned. Apart from that, the numerical experiments also showed that the new kernel performs similarly and sometimes even better than the standard kernels (RBF, polynomial, RQK, mixed two-kernels). Finally, the results revealed that the performance of 3-ConvSvm able to reduce the error loss by tuned the kernel parameters.

TABLE OF CONTENTS

Declaration and Copyright .... **i**
Acknowledgements .... **ii**
Abstract .... **iv**
Table of Contents .... **vi**
List of Acronyms .... **ix**
List of Tables .... **xi**
List of Figures .... **xii**

CHAPTER 1 .... **1**
Introduction **1**
1.1 Research Objectives – Original Contribution 4
1.2 Research Aim and Limitations 12
1.3 Organisation of Thesis 13

CHAPTER 2 .... **15**
Literature Review **15**
2.1 Corneal Injuries 16
  2.1.1 Eye Properties – Corneal Histology 16
  2.1.2 Corneal Assessment – Current Technologies and Methods 18
2.2 Hyperspectral Imaging (HSI) Overview 21
  2.2.1 General Applications of HSI 21
  2.2.2 HSI Technology, Image Acquisition System and Methods 23
  2.2.3 Medical Applications of HSI 32
2.3 Previous Work Related to the Eyes 35
2.4 Summary 38

CHAPTER 3 .... **40**
Research Background **40**
3.1 Hyperspectral Corneal Image Collection using Pushbroom Technique 40
  3.1.1 System Set-Up and Calibration 40

3.1.2 HSI Corneal Epithelium Image and Data Collection 47
3.1.3 Preliminary Analysis - Properties of Corneal Epithelium Layer Based on Hyperspectral Images.. 49
3.2 Digital Image Enhancement for Hyperspectral Image 59
3.2.1 HSI Image Normalisation 59
3.2.2 Brightness and Contrast Adjustment 60
3.2.3 Morphological Transformation 61
3.2.4 Laplacian of Gaussian Filter (LoG).. 63
3.2.5 Image Subtraction.. 64
3.3 The Dimensional Reduction of Hyperspectral Image... 66
3.3.1 Principal Component Analysis (PCA).. 66
3.4 Digital Image Classification.. 70
3.4.1 Image Feature Extraction.. 70
3.4.2 Support Vector Machine – Gaussian Radial Basis Function (SVM-GRBF)70
3.4.3 Convolutional Neural Networks (AlexNet) 72
3.5 Summary 79

CHAPTER 4.. 80
A New Hyperspectral Image Enhancement (8-SHIE).. 80
4.1 Spectral Bands Post-Processing 81
4.1.1 Spectral Binning 81
4.1.2 Image and Reflectance Normalisation.. 82
4.1.3 Bad Band Removal.. 85
4.2 The 8-Step Image Enhancement for Corneal Epithelium Injuries 86
4.2.1 The 8-SHIE Applied on Indian Pines 94
4.3 Performance Measure using Contrast to Noise Ratio (CNR) 101
4.4 Summary 103

CHAPTER 5... 105
Mixture Deep-Learning Classification of Corneal Epithelium Injuries 105
5.1 Building a Deep Learning Convolutional Neural Networks............................. 108
5.2 Histogram Feature Extraction with SVM-GRBF Classifier 110

5.3 Transfer Learning Using Pretrained AlexNet with a Fine-Tuned Model........... 112
5.4 Mixture AlexNet and SVM-Linear.. 116
5.5 Results and Performance.. 119
5.6 Parameter of Injured Boundary 123
5.7 Summary 126

CHAPTER 6.. 128

A New Mixing Kernel for Support Vector Machine Classifier (3-ConvSVM)..... 128

6.1 Developing New Kernel from Old Function.. 131
    6.1.1 Standard Kernel Functions and Covariance Function Characteristics 131
6.2 Proposed 3-Convex Kernels Combinations (3-ConvSvm) 136
    6.2.1 Kernel Coefficient Selection for 3-Convex Combination 138
6.3 Performance of the New Mixing Kernel.. 140
6.4 Summary 151

CHAPTER 7.. 152

Conclusions and Further Works 152

7.1 The 8-SHIE 154
7.2 Mixture Deep-Learning Classification 156
7.3 The 3-ConvSvm.. 158
7.4 Further Works... 160

References 162

Publications by the Author.. 173

LIST OF ACRONYMS

2D	Two dimensional
3D	Three dimensional
3-ConvSvm	3-convex SVM kernel function proposed in this thesis
8-SHIE	8-Step hyperspectral image enhancement proposed in this thesis
AUC	Area under the curve
AVIRIS	Airborne visible/infrared imaging spectrometer
CCD	Charge coupled device
CMOS	Complementary metal oxide semiconductor
CNR	Contrast to noise ratio
ECG	Electrocardiogram
ENVI	Environments of visualising images
FC	Fully connected
FFT	Fast Fourier transform
FIR	Far infrared
FN	False negative
FP	False positive
FPR	False positive rate
GA	Genetic algorithms
GPU	Graphic processing unit
GRBF/ RBF	Gaussian radial basis function
HSI	Hyperspectral imaging
HSV	Hue, saturation, value
ILSVR2010	ImageNet large scale visual recognition challenge 2010
IR	Infrared
LCTF	Liquid crystal tuneable filter
LED	Light emitting diode
LoG	Laplacian of Gaussian
MHSI	Medical hyperspectral imaging

MIR	Mid infrared
MM	Mathematical morphological
NIR	Near infrared
OCT	Optical coherence tomography
PCA	Principal component analysis
PCs	Principal components
Poly	Polynomial kernel
PRBF	Polynomial radial basis kernel function
PSO	Particle swarm optimization
RGB	Red, Green, Blue
ROC	Receiver operating characteristics
RQK	Rational quadratic kernel function
SC-PCA	Structured covariance PCA
SE	Structuring element
SVM	Support vector machine
SWIR	Short wavelength infrared
TN	True negative
TP	True positive
TPR	True positive rate
UV	Ultraviolet
VIS	Visible

LIST OF TABLES

Table 2.1: Current methods/technologies used in corneal assessment. 19

Table 2.2: Full optical spectral ranges (UV to IR). 27

Table 2.3: Summary of medical applications using hyperspectral imaging for the year 1988 to 2013 (summarised from [48]). 33

Table 2.4: Comparison of the present study with the previous research works on eyes. 36

Table 3.1: List of experimental works. 44

Table 3.2: Computational size requirement for the three types of PCA 69

Table 4.1: Classification accuracies (%) of the Indian Pines image obtained by eight classifiers. Table source [90]. 100

Table 5.1: 4-features computed from image histogram for 25 eyes. 111

Table 5.2: AlexNet parameters with fine-tuned network for transfer learning on cornea images. 113

Table 5.3: Four features classification using SVM-GRBF. 119

Table 5.4: Confusion Matrix. 120

Table 5.5: Quantification of eye injury (comparison of human and machine segmentation). 125

Table 6.1: Possible combination for the convex kernel coefficient............................ 139

Table 6.2: Classifiers performance on the eye dataset.. 145

Table 6.3: Classifiers performance on the iris dataset. 145

Table 6.4: Classifiers performance on the breast dataset.. 146

Table 6.5: Classifiers performance on the diabetes dataset. 146

Table 6.6: Classifiers performance on the heart dataset. 147

Table 6.7: Classifiers performance on the liver dataset... 147

Table 6.8: Classifiers performance on the satellite dataset. 148

Table 6.9: Generalisation ability... 149

LIST OF FIGURES

Figure 1.1: System block diagram. 2

Figure 1.2: Framework fusion of corneal epithelium analysis using hyperspectral imaging and image processing algorithms. 5

Figure 2.1: Cross-sectional of human cornea (healthy) using OCT and schematic diagram of corneal layers. 17

Figure 2.2: Pushbroom hyperspectral imaging. 24

Figure 2.3: Fundamental components of an HSI system. 27

Figure 2.4: Spectral response for halogen and LED lamp. 28

Figure 2.5: Anatomy section of the human eyeball. 37

Figure 3.1: Hyperspectral corneal image collection. 41

Figure 3.2: Halogen lamp covered with paper filter. 42

Figure 3.3: Hyperspectral imaging system. 43

Figure 3.4: Staining process. 45

Figure 3.5: Blue lamp illumination source for the stained eye. 46

Figure 3.6: White tile and checkerboard paper for calibration. 47

Figure 3.7: 25 hyperspectral images sliced at band-100. All images were normalised and resized to 100 by 100 pixels. (a) Rows 1 and 2 are images of healthy Corneas. (b) Rows 3 and 4 are images of corneas with induced epithelial injuries. (c) Row 5 shows the ground truth images. 48

Figure 3.8: An identical sample is captured using the digital camera (on the left) and scanned with the hyperspectral camera (on the right) with their respective histogram. 49

Figure 3.9: Sample of eye that consisted of normal and injured cornea. 51

Figure 3.10: Sample of eye with normal cornea. 51

Figure 3.11: (a) Image sliced at band-150 (638 nm), selected pixels of two surfaces: 52

Figure 3.12: (a) Left: Sample of healthy eye, image sliced at band-150 (638 nm), 53

Figure 3.13: Signature reflectance of healthy eyes. 54

Figure 3.14: Signature reflectance of injured eyes without stains. 55

Figure 3.15: Signature reflectance of injured eyes with stains. 56

Figure 3.16: Images sliced at bands 518 nm, 698 nm, 758 nm, and 818 nm at first column of (a), (c), (e), and (g) represent grey scale images. The second column of (b), (d), (f), and (h) represent HSV colour images. 58

Figure 3.17: Illustration of flat-field correction procedure: (a) original image, (b) flat-field background, and (c) processed image [69]. 60

Figure 3.18: Gamma correction [70]. 61

Figure 3.19: Eroded Image. (a) Original image. (b) Eroded with ‘disk’ SE. (c) Eroded with ‘spherical’ SE....63

Figure 3.20: LoG operation with different value of sigma [76]....64

Figure 3.21: Pre and postcontrast enhanced MRI images with fat suppression (A and B) of the pelvis in female patient showing a large ovarian lesion exhibiting a hyperintense signal in both images. Subtraction image (C) shows multiple mural solid enhancing nodules seen along the wall of the lesion (arrows). The possibility of a mucinous ovarian cystic neoplasm probably of malignant nature was suggested and was confirmed histopathologically [77]....65

Figure 3.22: AlexNet architecture....74

Figure 3.23: Example of pre-trained with transfer learning approach [90]....75

Figure 3.24: Convolution layer image output [91]....76

Figure 3.25: Max pooling process [92]....77

Figure 3.26: Rectified linear units (ReLU) function [92]....77

Figure 3.27: CNN with fully connected (FC) and softmax layer. Model 1 has a FC layer of 1024 neurons, while Model 2 presents 32 neurons [93]....78

Figure 3.28: Neural network without and with dropout....78

Figure 4.1: Image sliced at band-150 (638 nm). Mean reflectance of original image at pixel ‘X’ as labelled....81

Figure 4.2:Spectral Binning. The number of across-track spatial pixels is preserved whereas the bands (0,1,2) are binned to form band (0), bands (3,4) will form band 1 and so on [94]....82

Figure 4.3: (a) Spectral signature for 302-band. (b) Spectral signature for 151-band. (c) Spectral signature with normalised image and reflectance between band-15 and band-110....83

Figure 4.4: Visual interpretation on single band....85

Figure 4.5: Block diagram of HSI image enhancement....87

Figure 4.6: Ten principal components (PC) of eleven eyes transformed with PCA. Clinical information was noted in several PCs, particularly for EYE8 until EYE11, as these images were stained. In contrast, EYE1 to EYE7, which were not stained, appeared similar although EYE4 to EYE7 displayed abnormal corneal epithelium....88

Figure 4.7: Template matching-FFT based correlation. (a) Input image. (b) Template image. (c) Correlation plot. (d) Template matched....89

Figure 4.8: Output image at bands 1-50, 50-100, 100-150, 150-200, and 200-250. Image at row 2 column 3 is the ground truth image....91

Figure 4.9: Four output image with different parameter setting ([5,5], [3 3], 0.1), ([15,15], [5 5], 0.1), ([25,25], [7 7], 0.1), and ([50,50], [9 9], 0.1). Image at row 2 column 2 is the ground truth image....93

Figure 4.10: (a) Image enhanced. (b) Ground truth image....94

Figure 4.11: Image comparison before and after enhancement. (a) Original image without stain. (b) After image enhancement (without stain). (c) Ground truth image with stain....94

Figure 4.12: Indian Pines before apply image enhancement. 96

Figure 4.13: Indian Pines after apply image enhancement. 98

Figure 4.14: Spectral signature of Indian Pines data for ten classes after image enhancement. From top are woods, buildings, wheat, and corn in a group. Next is oats followed by alfalfa and hay in a group. Final signatures in a group are steel tower, soybean, and grass. 99

Figure 4.15: Images of healthy cornea with the histogram underneath respectively. Images were normalised and resized to 100 x 100. (a) Original image sliced at band-100 (CNR: 33.1256), (b) Image after PC subtraction before enhancement (CNR: 27.276), and (c) Image after PC subtraction and enhancement (CNR: 77.3276). 101

Figure 4.16: Images of injured cornea with the histogram underneath respectively. Images were normalised and resized to 100 x 100. (a) Original image sliced at band-100 (CNR: 46.4635), (b) Image after PC subtraction before enhancement (CNR: 36.1354), and (c) Image after PC subtraction and enhancement (CNR: 93.6535). 102

Figure 4.17: All the images were normalised and resized to 100 x 100. Rows 1 and 2 represent healthy eyes, while rows 3 and 4 denote injured eyes. 102

Figure 5.1: Framework of three classification approaches. 106

Figure 5.2: Injured cornea with image augmentation. 114

Figure 5.3: Healthy cornea without image augmentation. 114

Figure 5.4: Feature extraction with pretrained AlexNet on cornea images classification using SVM. 116

Figure 5.5: Sample of features extraction. (a); Conv1 (56 channels); (b); Conv5 (30 channels); and (c) FC8 layer (channel 1). 118

Figure 5.6: Decision boundary and support vector for mean vs skewness (testing data). 120

Figure 5.7: ROC curve for 2D-features classification by SVM-GRBF with C = 500, and Sigma = 1.658...121

Figure 5.8: The accuracy of AlexNet and AlexNet-SVM classifier. 122

Figure 5.9: The time consumption of AlexNet and AlexNet-SVM linear classifiers. 122

Figure 5.10: Image in size 100 x 100. Row 1: Human segmentation using selected image from one PCs. Row 2: Machine/colour image segmentation using RGB image selected from three PCs. 125

Figure 6.1: Framework of new mixing kernel for SVM..130

Figure 6.2: The characteristics curve of polynomial kernel with increased polynomial degree, d. 133

Figure 6.3: The characteristics curve of RBF kernel with increased sigma, σ. 134

Figure 6.4: The characteristics curve of RQK kernel with increased sigma, σ with same value of C=1...135

Figure 6.5: The characteristics curve of mixed RBF and polynomial kernel with different kernel parameters, C with test input 0.1. Where, d = 2, σ = 0.25. 137

Figure 6.6: The characteristics curve of 3-ConvSvm kernel with different kernel parameters with $C = 1$. The kernel coefficient is set as:...138

Figure 6.7: The accuracy of 32 convex kernel combination...139

Figure 6.8: Pig's Eyes dataset (total:25, training: 19, testing: 6)..141

Figure 6.9: Iris dataset (total: 100, training: 80, testing: 20). 141

Figure 6.10: Breast dataset (total: 683, training: 543, testing: 140)..141

Figure 6.11: Diabetes dataset (total: 768, training: 614, testing: 154). 142

Figure 6.12: Heart dataset (total:297, training:238, testing:59)..142

Figure 6.13: Liver dataset (total:345, training:276, testing:69). 142

Figure 6.14: Satellite dataset (total:1333, training:858, testing:475). 143

Figure 6.15: Adding class noise in the dataset...143

Figure 6.16: Adding attribute noise in the dataset. 144

Figure 6.17: Samples distribution of heart dataset as training and iris dataset for testing. 149

CHAPTER 1

INTRODUCTION

There are various causes of visual defects which can be broadly categorised into infectious and non-infectious [1]. It is estimated that about 285 million people worldwide are either visually impaired or blind, out of which, approximately 80% of them are thought to have a preventable causes [1]. Blindness inflicted by the diseases of cornea, (the outermost layer of the eye) plays a significant role in these statistics, second only to cataracts in the overall importance [2]. Nevertheless, the diagnosis of corneal diseases remains challenging even amongst eye specialists. Therefore, the advances in the assistive technologies for the specialists and non-specialists to detect any corneal disorders at the earliest stage possible are crucial in reducing the prevalence of blindness worldwide.

Hyperspectral imaging (HSI) is a relatively new, yet advanced, biomedical technology that combines imaging with spectroscopy. Initially developed for earth remote sensing [3], the technology underwent major advances to conform to the different challenges in the various industries, including space exploration [4], food safety and quality control [5], [6], [7], [8], [9], and archaeology for conservation and authentication [10]. More importantly, this technology has recently become an integral part of healthcare, in the clinical diagnostics and surgical guidance.

An excellent example of the viability of this technology in biomedicine is HELICoiD [11], a European collaborative project. The project was co-funded by the European Union and established to support the HSI technology in real-time detection of malignant primary brain tumours during surgery. In addition, HSI has been adopted at a research level in quantifying the degrees of skin burns [12], demonstrating its potential role to guide the clinicians in monitoring the healing process of their patients during treatment. In surgery, HSI has also been trialled to enhance visualisation during operations by improving the tissue visibility [13], [14] and detect local pathological tissues without any invasive tissue biopsies [14], [15].

There are several ways for an eye specialist to investigate the corneal injuries or diseases. Common methods include the slit lamp [16], the confocal microscopy [17], and the optical coherence tomography (OCT) [18], [19], all of which require a corneal staining prior to the procedures [20]. Despite their usefulness, these methods pose some challenges in the real-life setting because they usually involve heavy and complex machinery. Furthermore, they are costly and highly operator-dependent whereby a specialist is usually required.

This thesis has proposed a non-invasive system which could overcome the above challenges and allow clinicians to evaluate the corneal epithelial injuries in a more objective manner. The overall system has been summarised in **Figure 1.1**.

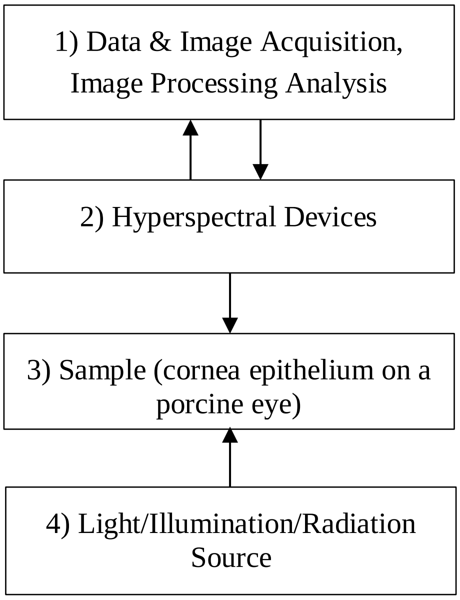

Figure 1.1: System block diagram.

The block diagram comprises four main components: (1) an image acquisition via capturing and processing of the image; (2) an imaging device to provide spatial resolution and spectral signatures of reflectance; (3) a subject/sample to be observed (the corneal epithelium on a porcine eye), and; (4) a light source to ensure sufficient illumination on the subject of interest. Further details such as the system set-up and calibration are discussed in Chapter 3.

At present, the dye test (fluorescein, rose bengal, or lissamine green) coupled with the use of a slit lamp machine is the most commonly used method to assess the corneal epithelial damage. This method allows the clinicians to assess the extent of damage despite often without any robust scale or objective measures [21]. The efforts to objectively quantify the corneal epithelial cell damage are still scant in the existing literature.

Therefore, this research proposes the technique of combining HSI and image processing as an approach to visualise and classify the normal and abnormal cornea. The research aims to provide objective measurements by proposing an image enhancement and mixing kernel for classification, which could potentially improve the current investigations for corneal injuries and eliminate the application of eye staining. To the best knowledge of the author, the findings and the proposed algorithms presented in this thesis could contribute to the body of knowledge and provide important insight into the evaluation of corneal epithelial injuries using HSI.

1.1 Research Objectives – Original Contribution

This research aims to improve the evaluation of corneal injuries in eliminating the application of eye stains, by proposing an image enhancement and design a new mixing kernel to provide objective measurements. Currently, it is common clinical practice to administer a dye onto a patient’s cornea before performing a cobalt-blue light or a slit-lamp eye examination. These tests, while useful in diagnosing a corneal problem, may cause a great discomfort to the patient.

This study, therefore, explores the potential of the combination of HSI and image processing in visualizing and classifying the normal and abnormal cornea specifically to the epithelial layer. The proposed framework illustrated in **Figure 1.2** in this thesis to study the corneal epithelial injuries using HSI could be a new contribution in the field of ophthalmology and optometry.

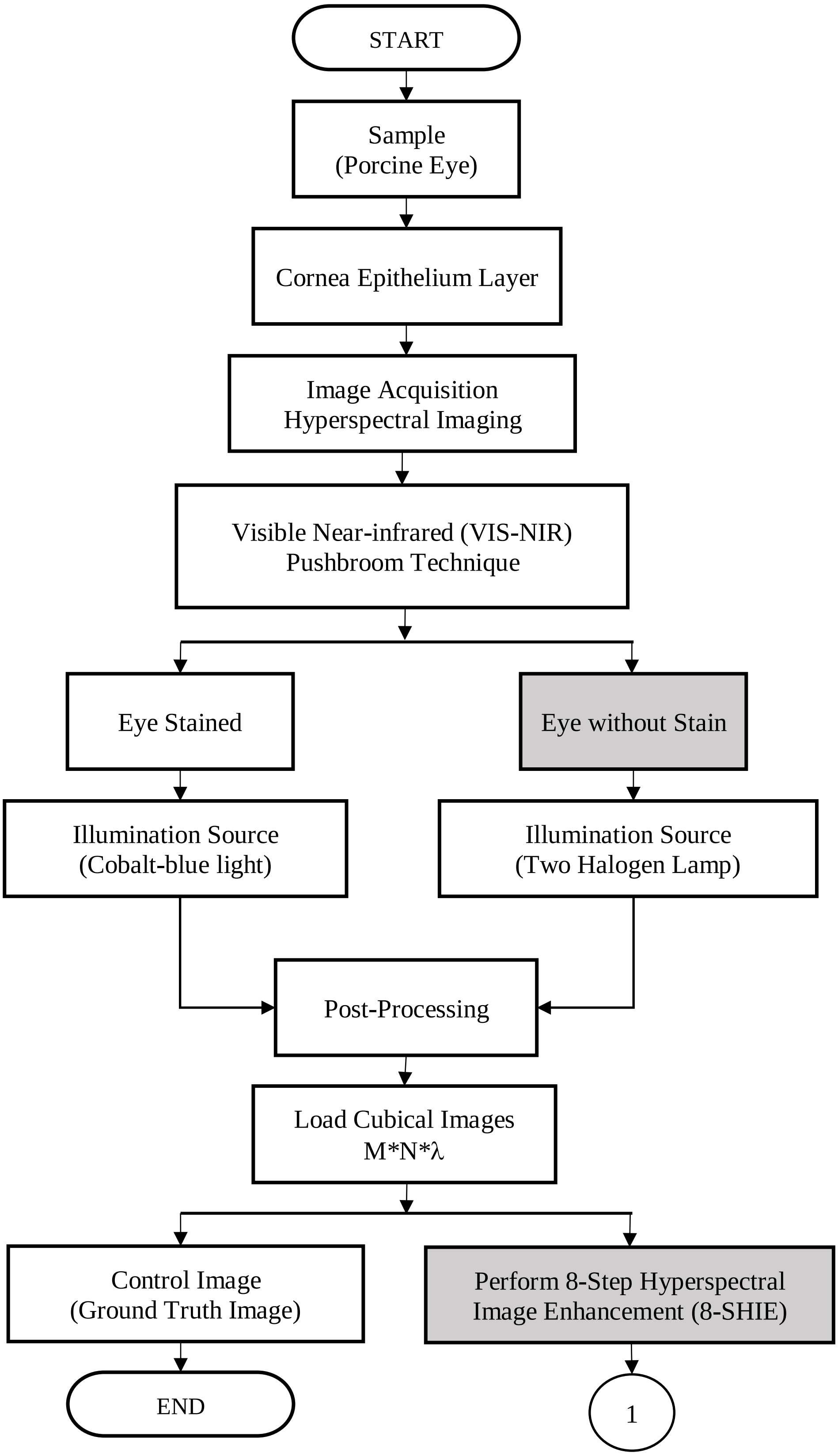

Figure 1.2: Framework fusion of corneal epithelium analysis using hyperspectral imaging and image processing algorithms.

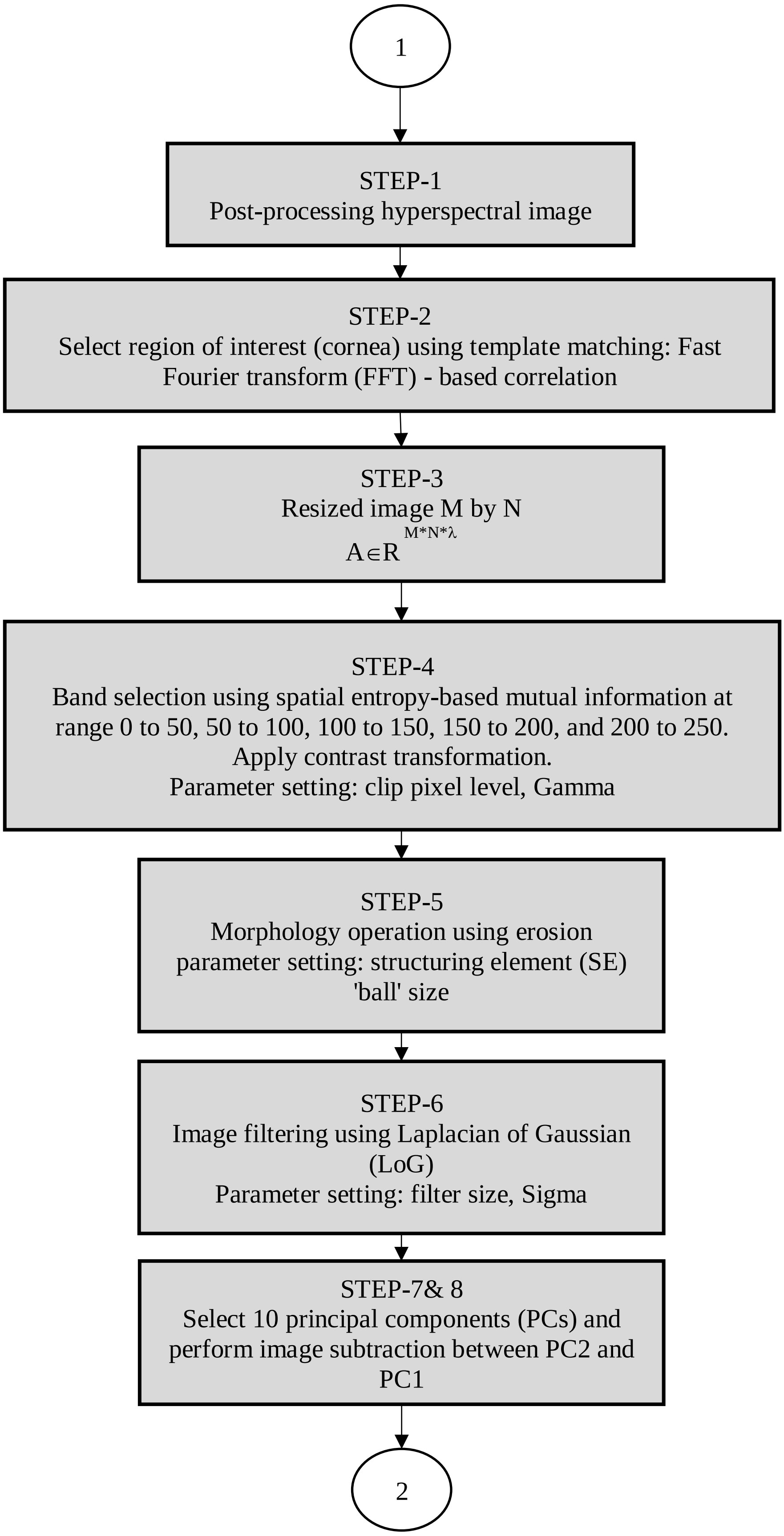

Figure 1.2: ***Cont.***

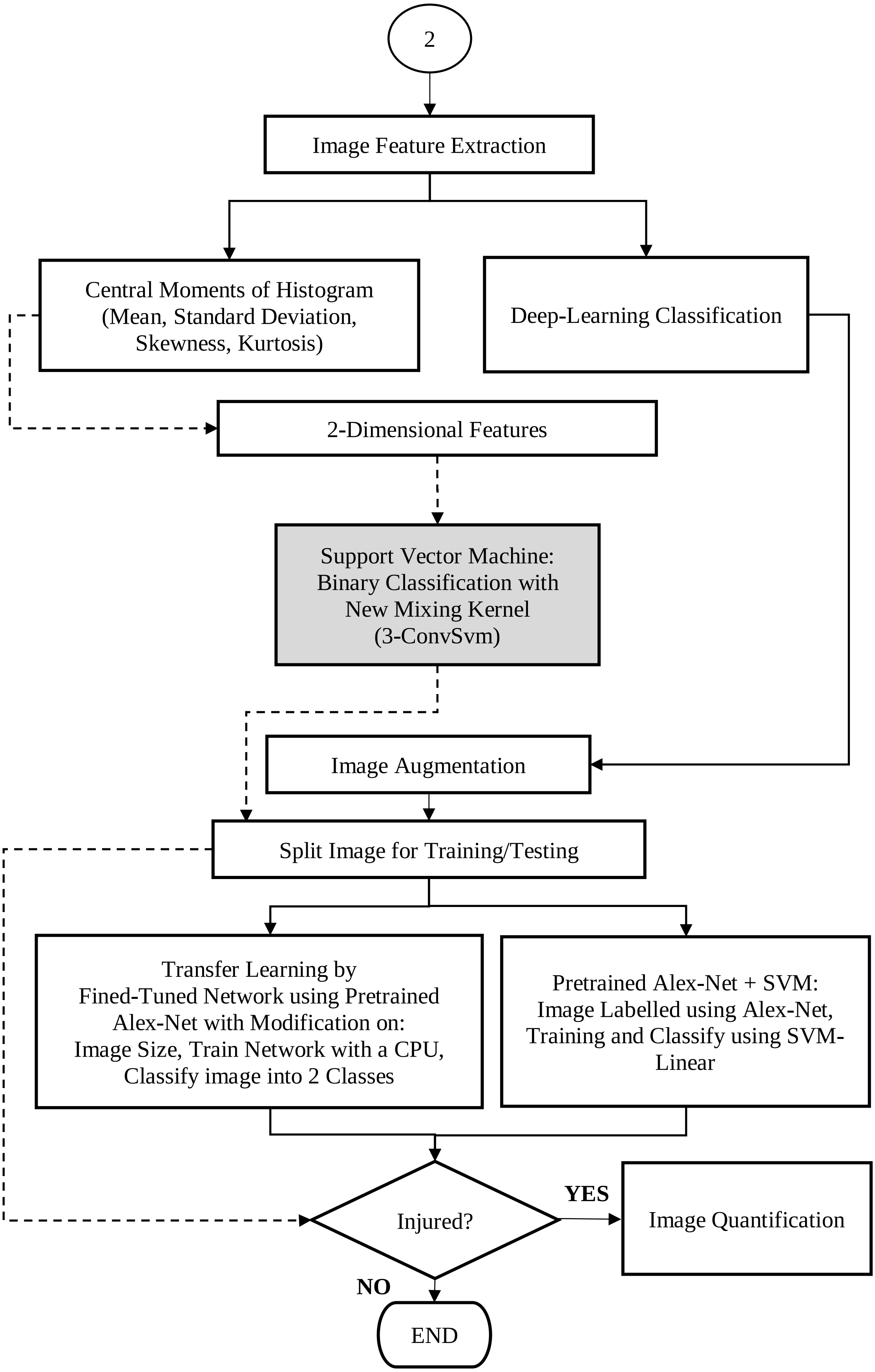

Figure 1.2: ***Cont.***

Details explanation about **Figure 1.2** is separated into chapter 3, 4, 5, and 6. Chapter 3 provides a new hyperspectral image collection of cornea epithelium on pig's eyes. Chapter 4 introduces a new algorithms of hyperspectral image enhancement. Chapter 5 defines mixture deep learning classifier. Chapter 6 designs a novel mixing kernel for support vector machine.

This thesis can be viewed from two perspectives. First, from the perspective of bio-medical engineering, and second, from the perspective of image processing. This research work is the first to describe in detail the use of HSI in investigating the corneal epithelial injuries by using the porcine eye. This empirical research provides novel contributions through the following:

From the perspective of bio-medical engineering:

1 – A new hyperspectral image collection of the cornea would be beneficial to the researchers in the eye diagnosis (Chapter 3).

2 – A new conceptual framework in extracting and analyse data from the corneal tissues through the hyperspectral imaging.

From the perspective of image processing:

3 – Develop a new 8-step algorithms to enhance image for the analysis of the corneal epithelial injuries and named it as 8-SHIE (Chapter 4).

4 – A technique to classify the injured and healthy corneal epithelium using the Gaussian radial basis function in the support vector machine (SVM), as well as the mixture deep-learning classifier by modifying the network parameters (Chapter 5).

5 – A new mixing kernels with three convex combinations for the SVM classifier (3-ConSvm) (Chapter 6).

Each of these contributions will be explained in more detail:

In Chapter 3 of this thesis, a new dataset of hyperspectral images of porcine cornea is presented as the first research contribution. Corneal abrasion resulting in a partial loss of the epithelium has been chosen as the clinical problem of this research work. The loss of the epithelial layer is frequently undetected by the assessors, and is often only visible after the corneal surface is treated with diluted 1% fluorescein drops and viewed under the cobalt blue lighting. Thus, to provide objective measurement to the assessors and to avoid eye staining procedure, the application of HSI for corneal epithelium injuries is proposed. Two types of camera were used, namely VIS-NIR and NIR, to visualise images in different wavelength range. The hyperspectral image acquisition has been performed through the HSI system, whereby the line scanning method has been employed for the collection of images in the series of experiments.

The second contribution is the first detail conceptual framework of cornea injury assessment using HSI. The framework consists of image acquisition using HSI pushbroom technique, a new image enhancement algorithm, mixing deep-learning image classification, and a novel mixing kernel for SVM classifier.

The third novel contribution to knowledge of this work is 8-SHIE which helps to enhance an image to provide objective interpretation. Eight steps of combined algorithms had been performed to obtain distinction and visualisation of both normal and abnormal corneal epithelium. The proposed method has been tested on a new image collection and existing hyperspectral datasets.

The fourth contribution to knowledge of this work is the mixture deep learning classification presented in Chapter 5. Three types of classification approaches were used and discussed in this chapter. First approach is histogram feature extraction with SVM-GRBF classifier. A total of four features were extracted, namely mean, standard deviation (square root of the variance), skewness, and kurtosis which were calculated using the probability distribution of the intensity levels in the histogram bins. For the second and third approaches, image augmentation with flipping and rotation was applied in order to obtain more images. Next approach is transfer learning using pretrained AlexNet with a fine-tuned model. The final approach is feature extraction with pretrained AlexNet (mixture AlexNet and SVM-Linear). The fusion of AlexNet and SVM-linear classifier was used for comparison to the standalone AlexNet. The combination of AlexNet and SVM-linear showed good performance, where AlexNet performs the high-level feature extraction, while SVM-linear carries out the classification. A performance comparison of these approaches is provided.

The new mixing kernel (3-ConvSvm) described in the Chapter 6 is the fifth contribution to knowledge in this thesis. This kernel is combination of three existing kernels known as Poly, RBF, and RQK. The proposed method was applied with numerical experiments on several number of selected datasets. In particular, different type of datasets which include medical, general, and hyperspectral as well as the level of samples complexity were employed in this study for the purpose of producing the generalisation ability for the proposed mixing kernels. A comparison analysis was carried out between the accuracy of 3-convex kernel after tuned loss and the single-kernel and 2-convex kernel combination.

Overall, this research intends to explore the novelty of HSI in investigating the corneal injuries and reveal its potential for further development and translation into biomedical application, especially in the ocular clinical diagnostics.

1.2 Research Aim and Limitations

This study aims to explore the clinical role of the technique combining HSI with image processing in assessing the corneal injuries of patients. However, the porcine eyes have been used as the sample subjects instead of the human eyes because a research involving human subjects usually requires a longer time to obtain the regulatory and ethical approval. The 25 corneal samples in this study have been divided into three groups: the healthy eyes, the injured eyes with stains, and the injured eyes without stains, where the corneal injuries have been made visible using the HSI. The sample size in this research is not easily controllable as it depends on the quality and freshness of the porcine eyes obtained from the resources.

In addition, a high-resolution camera with an optimal illumination control has been used to produce an image of good quality. Therefore, only certain eyes and images are suitable for further processing. This research focuses on the new data collection for eye assessment, algorithms for image enhancement, mixtures deep-learning classification, and newly-designed mixing kernels for SVM classification of corneal epithelial injuries.

1.3 Organisation of Thesis

This thesis comprises of seven chapters.

Chapter 2 provides a review of the literature regarding the problem addressed in this study. The literature review divided into two main topics which are related to the cornea injuries and hyperspectral imaging overview. A discussion for the first main topic is narrowed down into the cornea histology, current technologies in cornea assessment, and previous related to the eyes. The latter topic is covered on hyperspectral imaging in general and medical applications, also the image acquisition systems and approaches.

Chapter 3 defines the background of study, methodology and procedures used for data collection and analysis.

The following three chapters present the three contributions to knowledge in this study consist of image analysis and the results related to the corneal epithelial injuries. These chapters are in continuation with each other, starting with the image visualization, spatial and spectral analysis followed by the image enhancement, feature extraction and selection, classification, quantification, and lastly the mixing kernels for SVM classifier.

Chapter 4 determines if hyperspectral imaging is possible in providing and revealing significant information from the cornea in general and especially to the epithelium layer. This chapter also presents how hyperspectral images were processed from raw images that contained massive information into formatted data file to minimise storage space. The analyses on spatial and spectral signatures are presented towards image enhancement so as to provide objective interpretation.

Chapter 5 describes and compares the three classification approaches with the purpose of figuring out the best accuracy and low time consumption for the cornea assessment. The three classification approaches are histogram feature extraction with SVM-GRBF classifier, transfer learning using pretrained AlexNet with a fine-tuned model, and feature extraction with pretrained AlexNet (Mixture AlexNet and SVM-Linear).

Chapter 6 introduces a new 3-convex combination kernels function for the binary SVM classifier. In fact, it is important to note that kernel development for SVM has received considerable attention in the last few years for hyperspectral image classification. The purpose of choosing binary classification in the current observation is due to the fact that most medical data are commonly classified into two-class problems, namely benign or malignant which is helpful in detecting breast cancer, healthy or disorder in liver diagnosis, injured or no injury in eyes disease, and present or absent of diabetes and heart assessments.

Chapter 7 offers a summary and discussion of the findings of this research. Additionally, the implications for practice and recommendations for future research are delineated

CHAPTER 2

LITERATURE REVIEW

This chapter is divided into four subsections. Section 2.1 defines the clinical problem related to the corneal injuries, and also the current technologies used for the corneal assessment. Section 2.2 presents the background of hyperspectral imaging system and its applications. The general applications of HSI are defined followed by the outline of its applications in the medical field. In addition, a comparison of the HSI image acquisition methods is made. Section 2.3 is about previous works related to the corneal epithelial injuries.

There are numerous studies surrounding these topics. Nevertheless, each study is only referred to as appropriate or briefly reviewed with the discussion mainly being focused on the analysis of corneal epithelial injuries using HSI and image processing techniques. This chapter ends with Section 2.4 where a summary of the key findings from the literature review is presented.

2.1 Corneal Injuries

2.1.1 Eye Properties – Corneal Histology

In general, an eye consists of two main parts, the cornea and the retina. The cornea is the foreground which refracts the light rays, while the retina is the background which contains the sensory receptors for vision.

The cornea is a crystal clear (transparent) tissue that covers the front of the eyeball. Its translucent property allows the light to enter the eye. As shown in **Figure 2.1**, it is comprised of five essential layers: the epithelium which is the outermost layer; the stroma which is in the middle layer; the endothelium which is the innermost layer; the Bowman membrane which separates the epithelium and the stroma; the Descemet membrane which lies between the stroma and the endothelium. The vital roles of the cornea are protection, transmission, and refraction [22]. While serving as a protective membrane, cornea also works with the lens of the eye to focus images on the retina.

The corneal epithelium is a tight and protective layer firmly attached to the underlying stroma which typically comprises five to seven layers of stratified squamous cells [22]. The outermost cells are approximately 50 μm in width [23] and they provide protection to the underlying layers. Being the outermost layer, it is frequently subjected to the external contact, therefore being a common site of injury on the cornea.

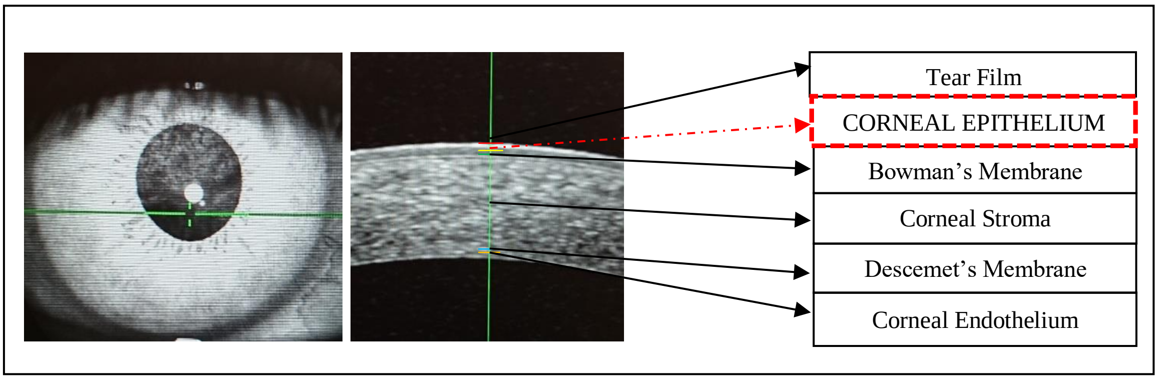

Figure 2.1: Cross-sectional of human cornea (healthy) using OCT and schematic diagram of corneal layers.

Meanwhile, the stroma constitutes 90% of the overall corneal thickness. It appears as a layer of organised, structured, dense, avascular, and relatively acellular connective tissue mainly comprising collagen and proteoglycans. On the other hand, the corneal endothelium is a 4-6 μm thick monolayer of approximately 400,000 cells arranged in a hexagonal mosaic [22]. This layer plays a significant role in maintaining the transparency and clarity of the cornea by regulating its water content.

Corneal damage can occur at different levels but injuries are often confined to the superficial epithelial layer. Such injuries trigger several mechanisms which contribute to the healing process, including the wound size and depth, the causative agents, and the tear quality [24]. Following a prolonged epithelial injury, the deeper stromal surface may be exposed and become irregular, causing the stroma to swell and cloud. Ulceration and scarring may follow causing the eye to become vulnerable to infection. A repetitive assault to the cornea, either acutely or chronically, is one of the main causes of visual impairment affecting people worldwide [23].

There are several causes of corneal injuries [25], [26], among which are abrasions which refer to any scratches or scrapes on the surface of the cornea, and chemical injuries, which can be caused by almost any fluid that is in contact with the eye. In addition, overuse of the contact lenses, poorly fitted lenses or sensitivity to contact lens care solutions can also harm the cornea. Exposure to foreign bodies such as sand or dust is also a common cause of corneal injuries. Furthermore, high-speed particles, such as chips from the hammering metal on metal are potential eye hazards which may adhere to the surface of the cornea. Rarely, they may penetrate deeper into the eye. Ultraviolet injuries to the eye can be caused by the sunlight, sun lamps, snow or water reflections, and arc-welding. The longer the exposure of the eye to the sunlight or the artificial ultraviolet light, the higher the risk of developing corneal injuries. Lastly, eye infections may also induce damage to the cornea.

2.1.2 Corneal Assessment – Current Technologies and Methods

As portrayed in **Table 2.1**, there are numerous technologies available in current clinical practice and research to acquire information about the cornea, including its morphology, shape, power, and thickness. Based on the literature review, five devices are currently used for corneal assessment, namely slit lamp, specular microscopy, ultrasound pachymetry, optical coherence tomography (OCT), and Scheimpflug imaging.

The slit lamp was first invented by Allvar Gullstrand in 1911 [27] and it has now become the most popular device used by clinicians to illuminate the anterior chamber of the eye. It is used for the direct visualization of a cornea at different magnifications with an independent illumination. With additional condensing lenses, it also enables the clinicians to observe the retinal condition.

Various anterior and posterior corneal disorders can be diagnosed using the different types of illumination setting of a slit lamp, including the diffuse illumination, direct focal illumination (wide or narrow beam), indirect illumination, retro illumination, and sclerotic scatter. However, the slit-lamp examination is time-consuming. Furthermore, there is no objective measurement and its settings, such as the illumination angle, the thickness of the beam, and the level of the illumination depend solely on the experts and therefore result in different assessment outcomes.

Table 2.1: Current methods/technologies used in corneal assessment.

No.	Device	Method/Corneal Assessment	Remark
1.	Slit Lamp Biomicroscopy [27]	- Direct visualization of the cornea at different magnifications with an independent illumination. - Parameters: Illumination angle, thickness of the beam, and level of the illumination.	- No objective measurement, totally depends on the ability of experts. Different assessment from one person to another.
2.	Specular /Confocal Microscopy [28]	- Non-contact optical instruments that use automatic image focusing technology. -Detect and monitor endothelial cell changes.	- Limit visualisation to detect microorganism on stromal tissues (result about 30 to 40%).
3.	Ultrasound Pachymetry [29]	-Use energy emitted from the tip of a probe that is reflected in the form of an echo/ultrasound wave. The time taken to return to the probe tip is used to calculate the corneal thickness.	-It is mandatory to apply topical anesthesia because of the direct contact of the probe with the cornea. -Disadvantage: patient discomfort or difficult repeatability when placing the probe perpendicular to the cornea. -Advantage: ease of use,portability, and low cost.
4.	Optical Coherence Tomography (OCT) [30]	-To obtain an OCT image, multiple scans are obtained at a series of lateral locations to form a composite two-dimensional image.	-Anterior and posterior segment imaging (Cross-sectional evaluation only)
5.	Scheimpflug Imaging [31]	-Provide corneal topography data (anterior and posterior corneal surface).	-Corneal surface measurement, apply to the healthy eye for contact lenses design.

Meanwhile, specular microscopy is mainly used for the corneal thickness measurement and the endothelial analysis. This technique can act as a non-invasive tool specifically for the endothelium analysis before and after an intraocular surgery [28]. Another method which provides the corneal thickness measurement is the ultrasound pachymetry [29]. Despite being low-cost, easy to use, and portable, this tool is invasive as it requires the application of a probe to the cornea throughout the procedure for the calculation process. Even though topical anaesthetics are administered prior to the examination, the direct contact of the probe tip to the cornea may still cause patient discomfort.

OCT was initially used for the imaging of the posterior segment of the eye but has now been improved for the analysis of the anterior segment of the eye as well. The anterior and the posterior segment of an eye can be inspected clearly using an infrared light with 1,310 nm and 800 nm, respectively [30]. To obtain an OCT image, multiple scans are performed at a series of lateral locations to provide cross-sectional evaluation of the cornea.

Lastly, the Scheimpflug imaging technique adopted with the Pentacam instrument is a diagnostic tool for corneal diseases based on the topography concept. In addition to diagnosing the corneal diseases such as cataract, it provides an objective evaluation of the corneal surface and serves as a significant tool for the refractive surgeons and the glaucomatologists [31].

2.2 Hyperspectral Imaging (HSI) Overview

2.2.1 General Applications of HSI

HSI was first introduced in 1985 as a remote sensing device. Since then, there has been an increasing research interest in exploring the potential of HSI for other applications. Over the years, it has gained much popularity due to the introduction of new techniques from various disciplines, particularly the development of statistical signal processing in engineering. The fast-growing computational technology and the advances in sensor development have transformed HSI into one of the most promising tools in data exploitation. Despite the data redundancies and the curse of dimensionality, HSI provides hundreds of contiguous spectral bands which constitute subtle information of a material or a tissue in the sample of interest. These diagnostic spectral bands are used for many purposes, including for detection, identification, recognition, discrimination, classification, and quantification. HSI is a non-contact and non-destructive technique which makes it ideal for a wide range of applications. Other non-medical applications are earth remote sensing, food applications, and surveillance monitoring.

As mentioned earlier, the earliest use of HSI was for the remote sensing and earth observation, which allowed different types of material on earth to be identified from the aircraft [3]. This system employed a sensor which had the ability to scan massive data. Goetz et. al [3] studied the Cuprite mining district of Nevada in mineral identification. Two types of mineral, alunite and kaolinite were discovered at 2.0 µm to 2.3 µm wavelength of spectral response. In the study, the spectral normalisation was applied to produce an equal intensity that allowed the direct comparisons of the different wavelength signatures for visual enhancement. For the classification, the authors proposed a binary encoding technique to achieve a rapid cross-correlation for signature matching, and applied the Hamming distance to measure the similarity between the two binary spectral vectors.

Further applications of hyperspectral remote sensing are in the vegetation and water resources [32], wetland vegetation [33], and geological [34]. Traditional methods for landscape-scale vegetation mapping require expensive time and intensive field surveys. Moreover, most of the land cover is grouped and the identification of individual species using the traditional methods is difficult. On the contrary, the remotely sensed data for the classification and mapping of vegetation provide a detailed and accurate in a timely and cost-effective manner. Furthermore, the availability of satellite and airborne hyperspectral data with its increased spatial and spectral resolution could enhance the classification and mapping of land use and vegetation. With a large number of wavebands, the image processing would be able to obtain both the biochemical and the structural properties of a vegetation [35]. Considering the limitations of the traditionally available wavebands, HSI is vital to further explore the spectral properties.

In the food industrial applications [5], [7], [36], normal machine vision systems have limited ability to conduct a quantitative analysis and capture a wide range of spectral information of the internal features. These internal features, such as texture, colour, tenderness, moisture, and fat and protein contents are important to maintain the quality and safety of the food. A traditional assessment involves the human visual inspection of the food products which is tedious, time-consuming, and even destructive. With the current increasing demand for a lower production cost and a higher efficiency, HSI is accurate, fast, real-time, and non-invasive seems, and it to be an ideal alternative approach to optimize the quality and safety of the food. Other than its usefulness in the food industry, HSI also plays a role in the art authentication to identify counterfeits through colour fidelity [37].

2.2.2 HSI Technology, Image Acquisition System and Methods

HSI is a hybrid modality that combines the imaging and the spectroscopy. By collecting the spectral information at each pixel of a two-dimensional (2D) detector array, HSI generates a three-dimensional (3D) dataset of spatial and spectral information, known as the hypercube.

HSI has been designed to integrate the imaging (spatial) and the spectroscopic (spectral) techniques into an imaging device [38]. Clearly, both pieces of information cannot be synchronized with each other from the conventional imaging or spectroscopy when they operate individually. Spectroscopy is a tool that acquires the spectral characteristics of a sample of interest to portray different intensities of light, i.e. electromagnetic energy from the object structures at different wavelengths, thus giving a unique spectrum signature to describe different types of elements. Meanwhile, imaging acquires spatial information from the object camera. The combination of these two techniques allows simultaneous acquisition of the spatial and the spectral information from an object. As a result, a 3D data cube can be perceived from the HSI by considering the 2D image as the image data and deriving a third dimension from the spectral information in the wavelength measurement [8].

The principal hardware used to generate hyperspectral images is known as the hyperspectral camera [38], [39]. The camera is combined with a light source and a separate processing device to allow a huge hyperspectral data to store to the next processing stage. For data collection, there are three types of device configurations, namely plane scanning or snapshot/staring, line scanning or pushbroom, and point scanning or whiskbroom.

Figure 2.2 shows the configuration of a line scan system which also known as the pushbroom technique. To capture a contiguous image, either the subject or the camera must be moved whereby the movement between the array detector and the frame acquisition rate requires synchronisation [39].

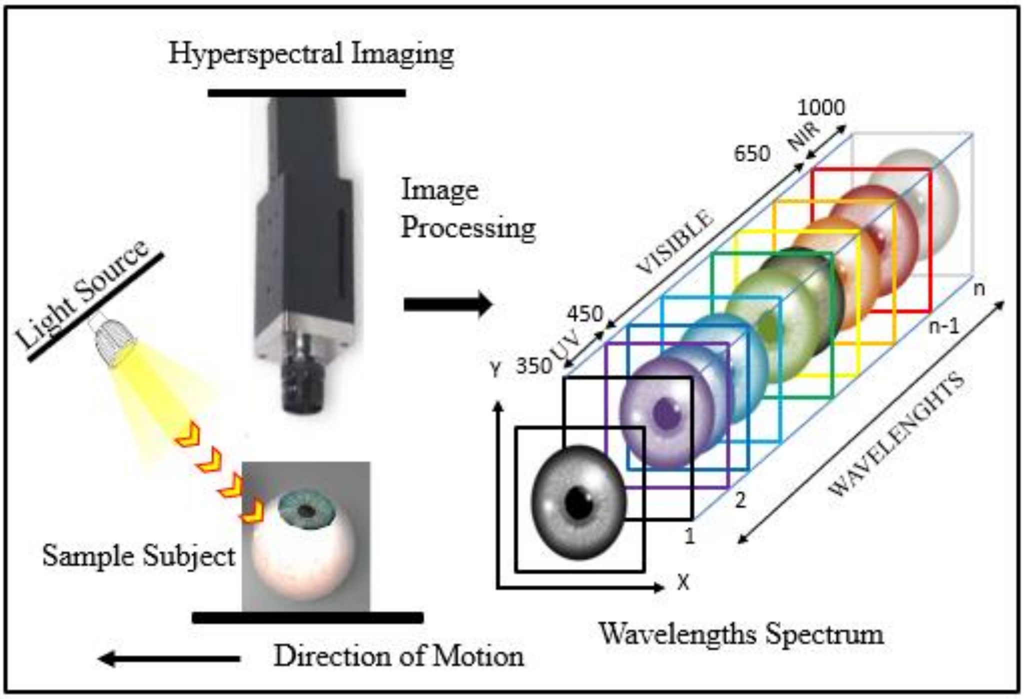

Figure 2.2: Pushbroom hyperspectral imaging.

The collection of data cube image is characterised by two fundamental image resolutions, i.e. spatial resolution, and spectral resolution [32]. Spatial resolution can be interpreted as the spatial quality measure in an image being observed. The higher the resolution, the clearer and the more detailed the image element is. The spatial feature of an image is related to the design of the sensor in terms of its field of view and the distance at which it operates above the surface [40]. Each of the detectors in a remote sensor measures the electromagnetic energy received from a limited patch on the sample surface. The smaller the individual patches, the higher the spatial resolution and the more detailed one can spatially interpret. On the other hand, spectral resolution can be interpreted as the ability of an imaging to discriminate different parts in the range of the measured wavelength intervals. Specifically, it measures the narrowest spectral feature that can be resolved by an HSI system. A higher spectral resolution can potentially provide a more accurate spectral signature of a sample.

With the rapid evolution of technology, several imaging technologies, each with its own strengths and limitations, have been applied and proposed to be used in the imaging system. These technologies include the conventional spectroscopy, conventional imaging, multispectral imaging, hyperspectral imaging, ultra-spectral imaging, and full spectral imaging, which have different range of wavelength.

Conventional spectroscopy has no spatial information to be captured. The main components are the light source, wavelength dispersion device, and point detector. It only collects the spectral resolution from dozens to hundreds of wavelengths of the sample. The measurement cannot cover large or small areas with a high spatial resolution due to the size limitation of the point detector. Meanwhile, conventional imaging consisting of a light source and an area detector do not have number of spectral bands which means there is no spectral resolution. The sensitivity depends on the area detector of the spectral response which has the capability of adjusting the image brightness/intensity by obtaining the spatial information from the sample in the form of a monochrome or RGB image.

These two devices have merged to form a system that is able to collect both spatial and spectral information from the sample. It is known as multispectral and hyperspectral imaging. Multispectral comprises of 3 to 10 spectral bands, and the spectral resolution is about tens nanometres.

The image acquisition performance is optimised through the hyperspectral where it is capable of acquiring hundreds to thousands spectral bands, and the spectral resolution is narrow into few nanometres. Compared to the multispectral, hyperspectral has able to identifies solids and liquids features from their respective reflectance or transmission signature [32]. Therefore, hyperspectral has the potential to capture the subtle spectral differences to provide detailed information for diagnostic purposes.

On the other hand, the ultra-spectral imaging has emerged as a recent advanced technology which contains thousands of spectral bands with a very narrow spectral resolution. This technology can detect and identify solids, liquids, and gasses. Nevertheless, it is costly and still under development. Another proposed data processing system is the full spectral imaging which has similar abilities to the ultra-spectral imaging. It contains thousands of continuous spectra over a full optical spectral range from the ultraviolet to the infrared (**Table 2.2**).

The more the spectral features available, the higher the potential information about the object that can be extracted. Thus, to achieve this goal, it is desirable to maximise the spectral resolution and coverage. However, the selection of the spectral range still depends on the application being observed.

Table 2.2: Full optical spectral ranges (UV to IR).

Range Name	Wavelength Range (nm)
Ultraviolet (UV)	200 to 400
Visible (VIS)	400 to 780
Near Infrared (NIR)	780 to 2500
Mid Infrared (MIR)	2500 to 25,000
Far Infrared (FIR)	25,000 to 1000000

The fundamental components of an HSI system (**Figure 2.3**) include the illumination sources (incoming light), the area detectors (image sensor), and the wavelength dispersion devices (prism or grating).

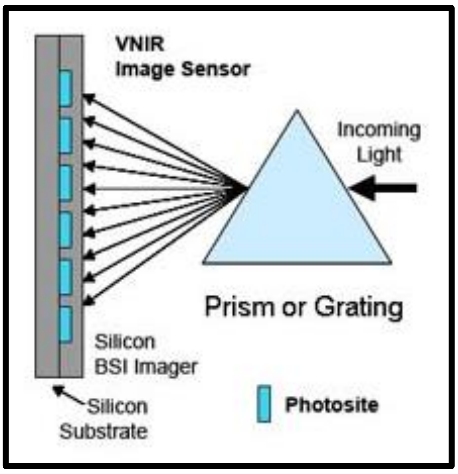

Figure 2.3: Fundamental components of an HSI system.
(source: https://www.teledynedalsa.com/en/learn/markets-and applications/aerospace/hyperspectral/)

Light source functions as a scene illumination and it is essential for a successful capturing of the wavelength variations that are reflected from or transmitted to the object of interest. There are three types of light sources commonly used in the HSI, namely halogen, light emitting diode (LED), and laser [41]. These light sources have been widely used in various medical devices for diagnosis of diseases, with each having its own pros and cons. LED [42], [43] is cheaper and safer for the eyes because it has less heat and no wavelength coverage at the UV range. Halogen produces heat but it has a smooth spectrum ranging from the visible to the infrared. Meanwhile, laser [44] is expensive but it has highly concentrated energy, a perfect directionality, and a true monochromatic emission.

The excitation wavelength of light over the full spectral range of the HSI system is highly desirable and it is expected to be as spectrally uniform as possible. As illustrated in **Figure 2.4**, the LED spectral response does not cover the full wavelength compared to the halogen spectrum.

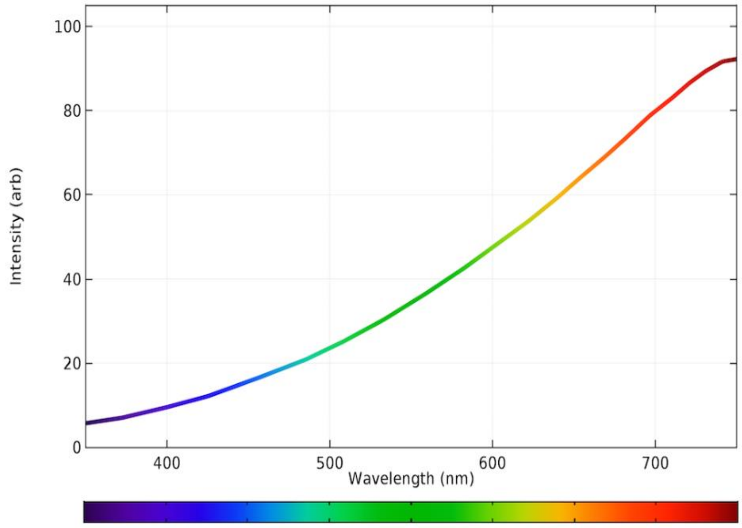

(a) Halogen Spectrum

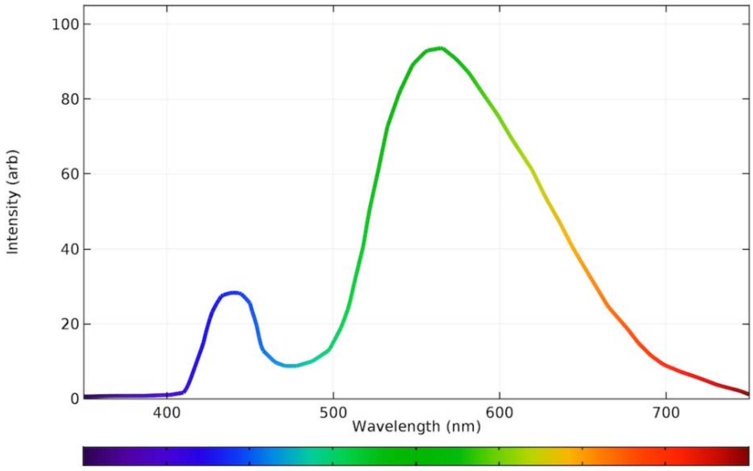

(b) LED Spectrum

Figure 2.4: Spectral response for halogen and LED lamp.
(*Source: http://www.specim.fi/iq/manual/software/iq/topics/illumination.html.*)

A good illumination plays a vital role in the spectral imaging and it can be evaluated based on three main parameters, namely intensity, spectral response, and uniformity. In terms of the light intensity, high light leads to a loss of information, while low light introduces noise peaks. An ideal spectral response should have a continuous spectrum to cover a full wavelength range. Meanwhile, shadow effects can be eliminated by uniformity [45], [46] whereby two or four light sources are used instead of one.

Another important component of HSI system is the area detector used to acquire the intensity of light transmitted from the dispersive devices. It measures the spectrum at each pixel by converting the light energy into the electrical signal. The area detector which is most widely used is the silicon charge coupled device (CCD) in the visible (VIS) and near-infrared (NIR) regions. The other example is the InGaAs detector which has a high-quantum efficiency and is well applied in the short wavelength infrared (SWIR) imaging. In addition, the complementary metal oxide semiconductor (CMOS) [47] is a recently designed area detector which can be used in the hyperspectral medium wave infrared imaging. In comparison to the CCD, CMOS has a lower cost and requires a lower power supply but it has a higher dark current and generates more noises.

Wavelength dispersion devices are the core components of an HSI system. The devices disperse the incident broadband light into different wavelengths and transfer the dispersed light to the area detector. The various types of the dispersive devices can be categorized into (1) monochromators, such as prism and diffraction grating which have been used in the push broom mode; (2) optical bandpass filters, such as the fixed or the tunable filter which have been widely used in the area scanning method, and; (3) single shot imager which is used in the snapshot HSI system [48].

There are three typical approaches for the hyperspectral sensing modes measurement to acquire spatial and spectral information, namely reflectance, transmittance, and interactance [49]. Reflectance mode is where the field of view of the light detector includes parts of the sample surface directly illuminated by a light source. Without the reflection of light, human eyes would be unable to perceive colour or texture of objects. Nevertheless, in the context of a spectrometer, reflection is simply a fraction of light reflected from a surface as the function of the wavelength.

While reflectance is the most commonly used in agriculture and food industry, transmittance is also used to detect the internal defects such as bruises in fruits (apple, pear, pickling cucumber, honeydew melon, and kiwi) [41]. This feature makes HSI suitable to be used in the medical field for detection of an internal disorder. Using the transmittance mode, the object viewed by the detector is diametrically opposite to the illuminated surface. However, its measurements are influenced by factors such as object geometry and size. Furthermore, in implementing the transmittance mode, it is important for sufficient light to penetrate the entire object of interest without causing any damage.

In relation to the interactance measurement, the field of view of the detector is separated from the illuminated surface by a light sealed in contact with the object surface. The path length of the light transmitted into the sample can be controlled, thus allowing the sensing mode to obtain more representative measurements of the sample. Nevertheless, an interactance mode is more complicated than the reflectance and the transmittance. Among the three modes, the reflectance is the easiest to obtain as it requires no contact with the object. Therefore, the most suitable sensing mode in this research is the reflectance measurement.

Spectral and spatial information can be acquired through several ways. Four image acquisition methods have been used in the previous studies [39], with each method demonstrating both pros and cons when being applied in the analysis of the biological tissues.

The first method is the point scanning or whiskbroom approach, which scans along two spatial dimensions by moving either the sample or the detector. This method usually requires two-axis motorised positioning tables to finish the data acquisition. The process is usually slow as the data are accumulated pixel by pixel in an exhaustive manner. However, this method employs a dispersive element to split the light and a factor to obtain a uniformly high efficiency. Furthermore, it has low scatter and it is less costly.

Secondly, the images can be acquired via the area scanning or staring approach, whereby the entire scene (x, y) is captured onto the focal plane, with one spectral band at one time. Besides, the three-dimensional data cube can be obtained without scanning. While the staring approach may reduce either the spatial or the spectral resolution, it remains suitable for the high-speed applications with its added advantage of producing an artefact-free image (no temporal distortion of the spatial information).

Next, single scanning or snapshot is another image acquisition method which is similar to the staring approach. Using this method, images can be captured at a high speed without any scanning. Nonetheless, its spatial and spectral resolutions are limited as the total number of voxels cannot exceed the total number of pixels on the area detector. In addition, this technique needs further development as there is still a lack of support for its higher resolution.

Lastly, images can be acquired by line scanning or also known as the pushbroom technique. This method is common and has been utilised in this research. It involves scanning an image line by line simultaneously to acquire both the spatial and the spectral information. The time exposure, however, must be short during line scanning to avoid the risk of inconsistencies at the spectral band level. In this study, the sample is moving forward or backward to perform scanning process using a motorised linear stage, while the camera remains stand still to capture the full band of image. Nevertheless, in the real clinical practice to capture an image of the human eyes, the patient remains still while the camera is moved.

Despite the rapid advances in technology, there is still no ‘absolute’ best method currently to select the most suitable image acquisition mode for a specific medical application. In determining the most optimal method for the medical imaging, the features of different tissues and the detection objectives must be considered.

2.2.3 Medical Applications of HSI

As with all other technologies, HSI has advanced over the years and has currently been widely used in the medical applications (see **Table 2.3**), particularly to diagnose diseases at an early stage [50], [48], [51] in both humans and animals. Medical hyperspectral imaging (MHSI) has been explored for its use in several surgeries, such as mastectomy, cholecystectomy, and abdominal surgery [48]. In [52], HSI was employed to monitor the oxygen saturation levels before a kidney transplant operation. In addition, it was used to measure the oxygen saturation in the optic nerve head of the monkey eyes [53].

Table 2.3: Summary of medical applications using hyperspectral imaging for the year 1988 to 2013 (summarised from [48]**).**

No.	Medical Application	Imaging mode	Spectral range (nm)	Measurement Mode	Year
1.	Burn wounds	Staring	400 to 1100	Reflectance	1988
2.	Cervical neoplasia	Staring	200 to 700	Fluorescence and reflectance	2001
3.	Cervical cancer	Staring	330 to 480	Fluorescence and reflectance	2003
4.	Cutaneous wound	Pushbroom	530 to 680	Transmission	2003
5.	Cervical pathology	FTIR	5000 to 10,526	Reflectance	2004
6.	Diabetic foot	Staring	500 to 600	Reflectance	2005
7.	Tumor hypoxia and microvasculature	Staring	400 to 720	Fluorescence	2005
8.	Skin cancer	Staring	440 to 640	Fluorescence and reflectance	2006
9.	Hemorrhagic shock	Staring	500 to 600	Reflectance	2006
10.	Melanoma	Pushbroom	365 to 800	Transmission	2006
11.	Skin bruises	Pushbroom	400 to 1000 900 to 1700 950 to 2500	Reflectance	2006&2012
12.	Ophthalmology-retina	Snapshot	450 to 700	Reflectance	2007
13.	Breast cancer	Staring	450 to 700	Reflectance	2007
14.	Laparoscopic surgery	Staring	650 to 1100	Reflectance	2007
15.	Intestinal ischemia	Pushbroom	400 to 1000 900 to 1700	Reflectance	2010
16.	Gastric cancer	Pushbroom	1000 to 2500	Reflectance	2011
17.	Endoscope	Snapshot	450 to 650	Reflectance	2011
18.	Atherosclerosis	Pushbroom	410 to 1000	Reflectance and fluorescence	2011
19.	Diabetic foot	Staring	400 to 720	Reflectance	2011
20.	Prostate cancer	Staring	450 to 950	Reflectance	2012
21.	Laryngeal disorders	Pushbroom	390 to 680	Reflectance	2012
22.	Cholecystectomy	Staring	650 to 750	Fluorescence and reflectance	2012
23.	Ovarian cancer	Staring	400 to 640	Fluorescence and reflectance	2012
24.	Pharmaceutical	Staring	1000 to 2400	Reflectance	2012
25.	Dental caries	Staring	900 to 1700	Reflectance	2012
26.	Leucocyte pathology	Staring	550 to 950	Transmission	2012
27.	Nerve fiber identification	Staring	550 to 1000	Transmission	2012
28.	Breast cancer	FTIR	2500 to 11,111	-	2013

Note: FTIR, Fourier transform infrared spectroscopy.

Spectral retina imaging was developed [54] by modifying a fundus camera with a spectral imaging device which was achieved by integrating a liquid crystal tuneable filter (LCTF) and a charge-coupled device (CCD). In the study, wavelengths between 500 nm and 650 nm were used to obtain retinal vasculature images for the analysis of arteriole and venule changes. Examples of the application of HSI in retinal imaging were detection of diabetic and non-diabetic based on the spectral difference in the Wistar rats [55] and the retinal tissue oximetry mapping of human eyes [56]. There have been a few studies focusing on the diagnosis of retinal diseases [57], [58], [59] but the investigation of the eyes using HSI particularly on the epithelium is still scant.

2.3 Previous Work Related to the Eyes

Table 2.4 presented a summary of the previous studies regarding the corneal injuries. In 2003, Reynaud et al. [60] investigated the spectral response on the cornea of a rabbit using the HSI interfaced with a confocal microscope. In the study, a highly transparent and healthy cornea was reflected with 410 nm to 918 nm wavelengths to generate an image in 256 spectral bands. The study discovered that the endothelial cell layer and stroma reflected at 440 nm to 730 nm. The combination of HSI and the confocal microscope was proven to be capable of isolating the corneal structures or the individual cells based on the spectral signatures.

On the other hand, Khoobehi et al. [53] evaluated the monkey eyes using HSI attached with a fundus camera to measure the relative changes in the oxygen saturation of the retina. Employing this technique, the study detected the abnormalities of the oxygen saturation in the optic nerve head which allowed an earlier diagnosis of glaucoma.

Another study on retina conducted by Qing Li et al. [55] on 40 healthy Wistar rats which were divided into normal, diabetic without treatment, and diabetic with treatment. The eyes were opened along the ora serrata (which forms the junction between the retina and the ciliary body, **Figure 2.5**), with each retina section being stained and scanned to acquire the desired images. As revealed by their results, the difference between the outer/inner nuclear layer and the inner plexiform layer can be visualised in the different spectral bands.

Table 2.4: Comparison of the present study with the previous research works on eyes.

No.	Title	Method/Corneal Assessment	Remark
1.	Confocal Hyperspectral Imaging of the Cornea. (Hyperspectral Imaging+Confocal Microscope)	-Sample/Object: examined highly transparent and healthy cornea of anesthetized New Zealand white rabbit. -410 nm to 918 nm wavelenghts. -256 spectral bands. -Extract nucleus, cytoplasm, and extracellular compartment.	ARVO Annual Meeting Abstract, May 2003. Reynaud et al. [60]
2.	Hyperspectral Imaging for Measurement of Oxygen Saturation in the Optic Nerve Head.	-Sample/Object: Monkey eyes. -Measured changes in oxygen saturation.	ARVO Journal, September 2003. Khoobehi et al. [53]
3.	Spectral Optical Coherence Tomography:A Novel Technique for Cornea Imaging.	-Sample/Object: 11 of human eyes. - Cross-sectional evaluation of various corneal pathologies.	Cornea-Lippincott Williams & Wilkins, Volume 25,Number 8, September 2006. Kaluzny et al. [18]
4.	New Microscopic Pushbroom Hyperspectral Imaging System for Application in Diabetic Retinopathy Research.	-Sample/Object: 40 healthy Wistar rats. Divided into three groups:10 normal rats,12 diabetic without treatment, and 12 diabetic treated. -400 nm to 800 nm wavelenghts. -To study the pathogenesis of diabetic retinopathy.	Journal of Biomedical Optics. Novembaer 2007. Qing Li et al. [55]
5.	Quantitative Evaluation of Corneal Epithelium Injury Caused by N-Heptanol using a Corneal Resistance Measuring Device In Vivo.	-Sample/object: An Albino rabbit's cornea was exposed to a filter paper immersed in n-heptanol for 1 minute to induce injury to the corneal epithelium. - Injury measured using an electrical corneal resistance device.	Clinical Ophthalmology, 2012. Fukuda and Sasaki [61]
6.	Analysis of Corneal Epithelium Injuries using Hyperspectral Imaging Combined with Image Processing Algorithm.	-Sample: Porcine eyes -Group into three: Healthy, injured with staining, and injured without staining. -Provide hyperspectral image dataset of porcine eyes for future study in ocular clinical diagnostics. -Develop a new/detailed framework for corneal epithelium injuries assessment including image acquisition, pre-processing, enhancement, classification, segmentation, and image quantification. -Develop new mixing kernel for support vector machine classifier.	**Author's approach**.

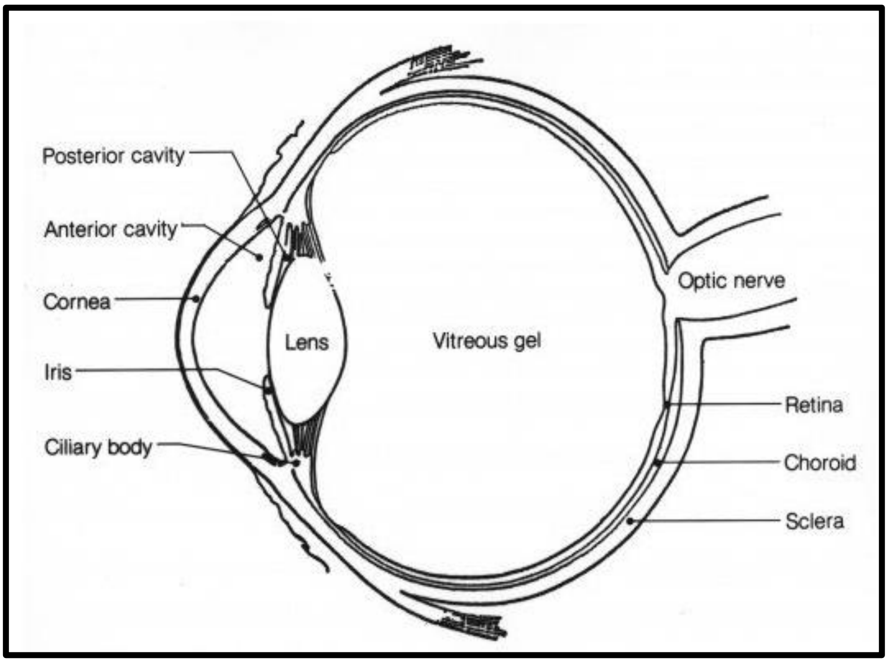

Figure 2.5: Anatomy section of the human eyeball.
(Source: https://owlcation.com/stem/Anatomy-of-the-Eye-Human-Eye-Anatomy)

Next, there was a study conducted by Kaluzny et al. [18] on 11 human eyes to evaluate the cross-sections of various corneal pathologies using the spectral OCT. The fusion of OCT and hyperspectral camera produced an objective assessment of the tissue changed and the shape, size, and location of the pathologies. In addition, the technique allowed the estimation of the epithelial thickness and the depth and width of the injuries. However, two devices were used for the evaluation.

Finally, Fukuda and Sasaki [61] also attempted to develop a device for the quantitative evaluation of the corneal epithelial injuries. In their experiment, n-heptanol was used to induce injury on the corneal epithelium of the albino rabbits. Instead of using the HSI, resistance was used by authors to measure the normal and the abnormal cornea whereby a damaged epithelium was indicated by an increased electric current flow.

2.4 Summary

HSI has first emerged as a better solution for the quality and safety inspection of food and agricultural products. Over the years, it has become an area of interest in the medical field as its application provides a more rapid and objective measurement.

Based on the literature review, the works of Reynaud (2003), Khoobehi (2003), and Kaluzny et al. (2006), employed HSI fused with another device, namely confocal microscope, fundus camera, and OCT, respectively. Meanwhile, the study conducted by Qing Li et al. (2007) acquired images of eyes using the pushbroom approach, which has been similarly employed in the present study. However, the study by Qing Li et al. focused on the pathogenesis of diabetic retinopathy in rats, while this research is about the corneal epithelial injury of the porcine eyes.

At present, the dye test (fluorescein, rose bengal, or lissamine green) coupled with the use of a slit lamp machine is the most commonly used method to assess the corneal epithelial damage. This method allows the clinicians to assess the extent of damage despite often without any robust scale or objective measures [21]. The efforts to objectively quantify the corneal epithelial cell damage are still scant in the existing literature.

Therefore, this research proposes the technique of combining HSI and image processing as an approach to visualise and classify the normal and abnormal cornea. The research aims to provide objective measurements by proposing an image enhancement and mixing kernel for classification, which could potentially improve the current investigations for corneal injuries and eliminate the application of eye staining. To the best knowledge of the author, the findings and the proposed algorithms presented in this thesis could contribute to the body of knowledge and provide important insight into the evaluation of corneal epithelial injuries using HSI.

CHAPTER 3

RESEARCH BACKGROUND

This chapter discusses the system set-up and calibration, hardware specification, image acquisition, and image collection. To the best knowledge of the author, hyperspectral image collection presented in this chapter is a novelty of this study. This is first work to use HSI for corneal epithelium injury detection as shown in **Figure 3.1**. Four groups experiments were performed to obtain high quality of images.

In addition, the background theory of the proposed algorithm is presented, which includes the image enhancement, normalisation, contrast transformation, mathematical morphological (MM), Laplacian of Gaussian filter (LoG), image subtraction, and principal component analysis (PCA). The two types of feature extraction applied in this research are described.

3.1 Hyperspectral Corneal Image Collection using Pushbroom Technique

3.1.1 System Set-Up and Calibration

The HSI system consists of structured frame (aluminium profile) and a spectrograph with the associated cameras. The spectrographs used are SPECIM ImSpector VNIR V10 and V10E, while the attached cameras are Basler piA 1600-35 gm GigE CCD camera with a spatial resolution of 1608 x 1208 pixels and a CCD camera Hamamatsu C8484-05G with a spatial resolution of 1344 x 1024 effective no. of pixels. The lenses are Schneider Xenoplan 1.4/23-0902 and 1.9/35-0901, respectively.

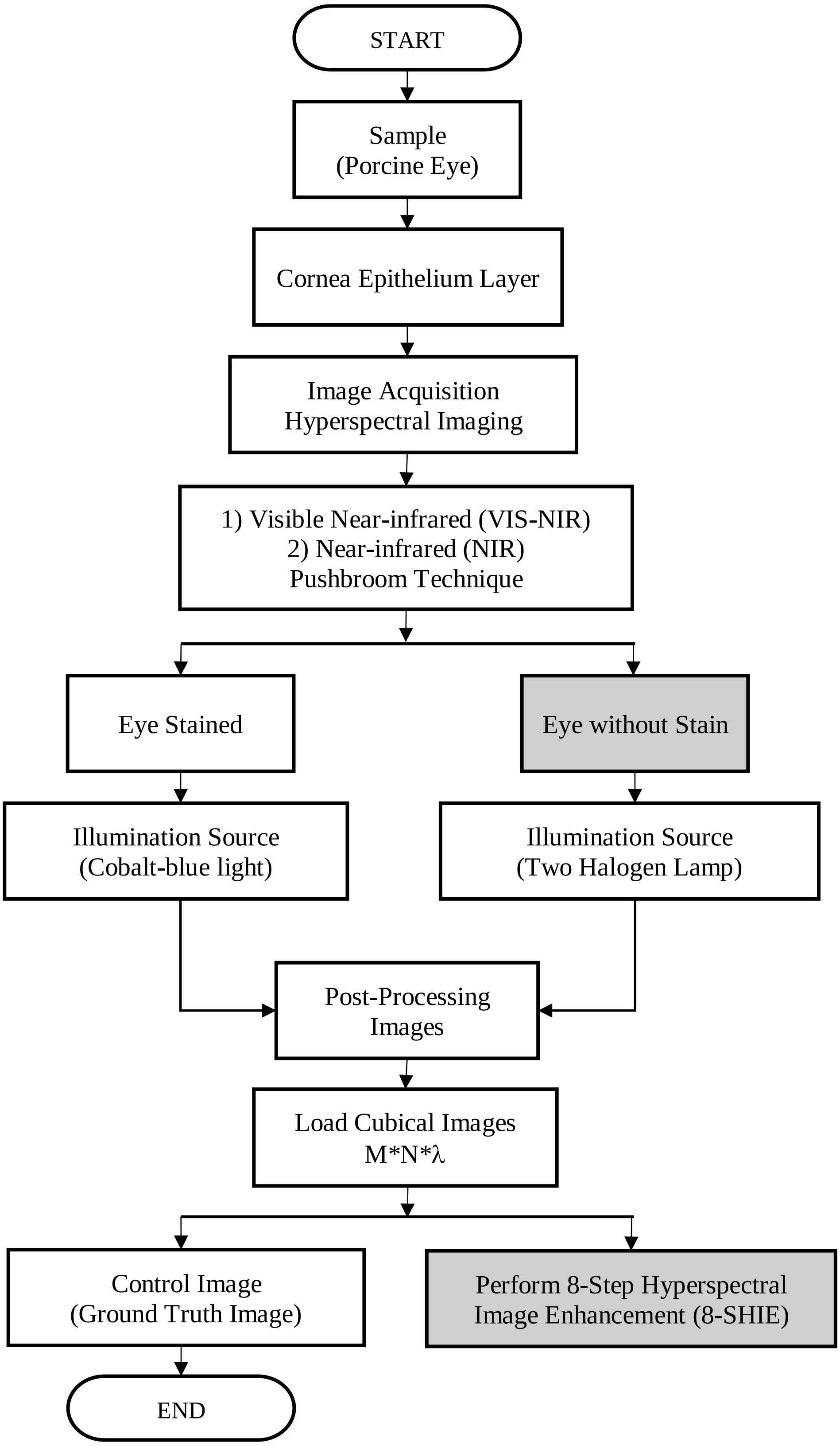

Figure 3.1: Hyperspectral corneal image collection.

In addition, there is a translation stage to move the sample forward and backward with an adjustable speed for line scanning, which is also known as the pushbroom method. There are two light sources: a blue lamp to illuminate the stained eye and a 35-watt halogen dichroic lamp for normal illumination. Two halogen lamps are assembled on the left and the right as an illumination source [62] of reflectance onto the sample. The paper filter is attached in front of lamp (**Figure 3.2**) to avoid an excessive radiation. Meanwhile, a frame is used as a holder for the camera, spectrograph, and lens.

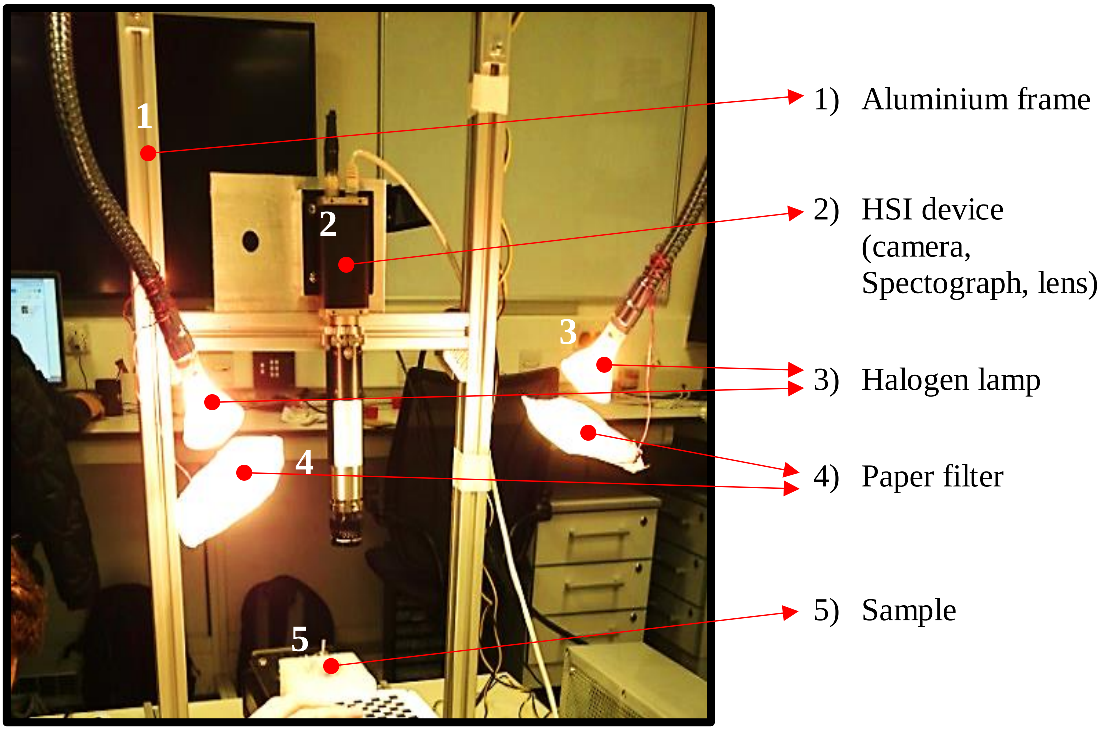

Figure 3.2: Halogen lamp covered with paper filter.

As illustrated in **Figure 3.3**, the hyperspectral image acquisition has been performed through the HSI system, whereby the line scanning (pushbroom) method [36] has been employed for the collection of images in the series group of experiments (**Table 3.1**). Two types of camera were used, namely VIS-NIR (group 1 to 3) and NIR (group 4), to visualise images in different wavelength range.

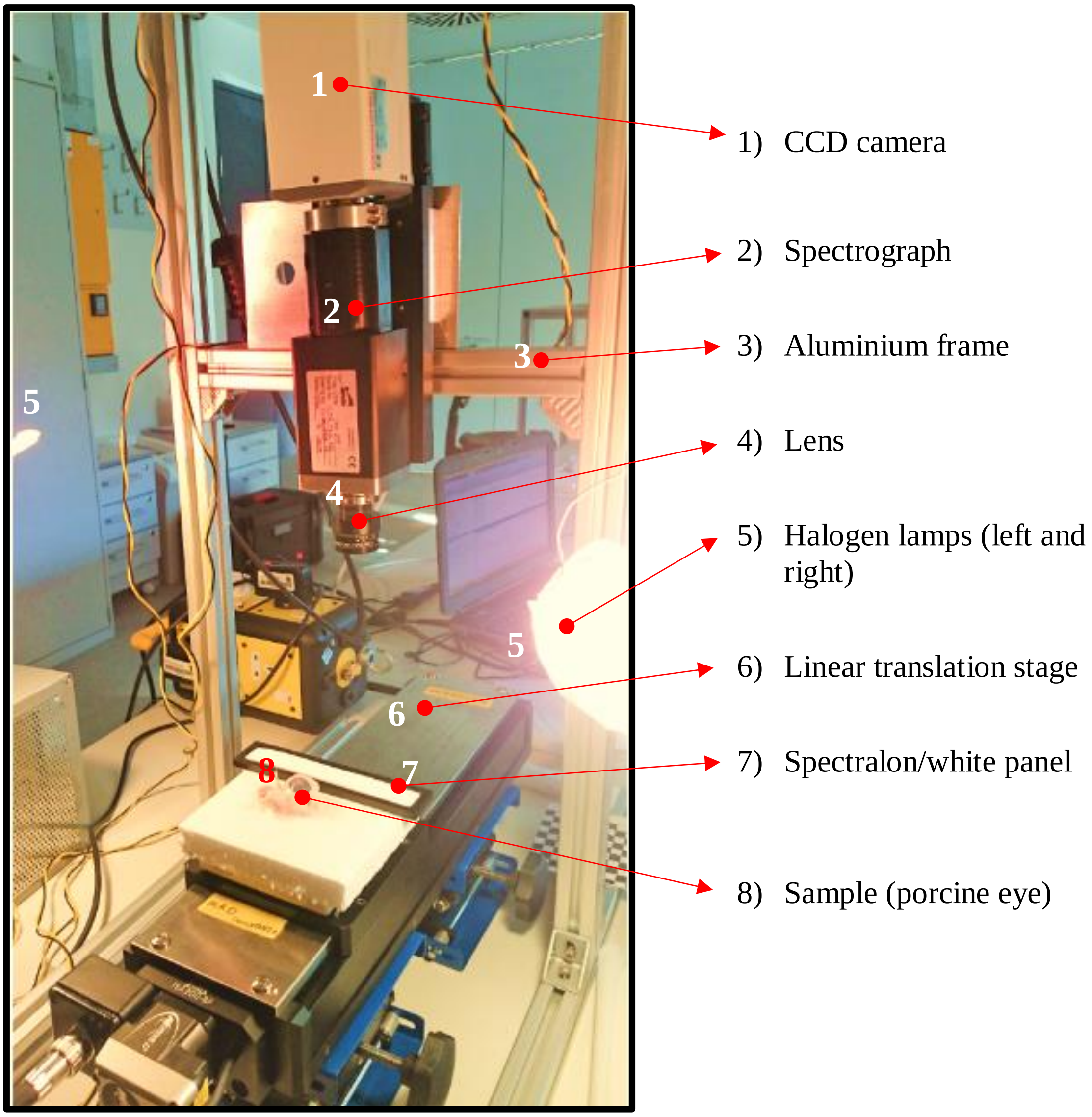

Figure 3.3: Hyperspectral imaging system.

Table 3.1 shows four groups of experiment, group 1 was performed using visible-near infrared camera as preliminary result of this study since there was no similar reference available. Five samples were bought and six were scanned, meaning one healthy eye has been scanned two times. The first time was healthy eye, and the second time was eye with injury (manually created).

Based on the preliminary result, HSI able to capture and record spectral and spatial tissues in tremendous detail. For that reason, the experiment has been continued to group 2 to collect more images. The samples of eye were dead tissues that have been dissected and frozen at resourced site (food industry) before delivery. Therefore, some of the eyes had poor quality. As shown in the group 2, 22 eyes were rejected. During this experiment, each sample has been scanned twice, first scan without eye staining, second scan with diluted 1% fluorescein eye drops. The eye stained is for ground truth purposes.

Table 3.1: List of experimental works.

Group	Quantity	Camera Type	Image Scanned	Remarks
1	Supplier A 5 Porcine Eyes	VIS-NIR (400 nm to 1000 nm)	6 Scanned (3 injured 3 healthy)	Pilot test [50] Image Dimension after binning: 1200 to 1300 × 804 × 302 302 spectral bands.
2	Supplier A 30 Porcine Eyes	VIS-NIR (400 nm to 1000 nm)	17 Scanned (from 8 Eyes) (5 injured + 7 Stained 1 Healthy + 1 Stained 3 No Intact Epithelium) 22 Eyes Rejected	Apply stains on image Dimension after binning: 500 to 700 × 336 × 256 256 spectral bands
3	Supplier B 12 Porcine Eyes	VIS-NIR (400 nm to 1000 nm)	26 Scanned (8 injured + 10 stained 4 healthy + 4 stained)	Apply stains on image Dimension after binning: 250 to 400 × 336 × 256 256 spectral bands
4	Supplier B 10 Porcine Eyes	NIR (950 nm to 1700 nm)	10 scanned (8 injured + 2 healthy)	Dimension after binning: 393 × 336 × 256

Image collection was resumed to group 3, since too many rejection samples (from 30 samples, 22 were rejected) in the group 2 from supplier A, new samples were bought from a new supplier (supplier B). From 12 eyes, 26 were scanned, consists of 8 eyes with injury without staining, 10 eyes were stained, 4 were healthy eyes with and without staining. Then, group 4 was a last group of experiment, and using near infrared camera to compare the results with VIS-NIR camera.

The porcine eye is anatomically and biochemically similar to the human eye, and therefore a common alternative for the wet lab-based research and the surgical training

[63], [64]. Corneal abrasion resulting in a partial loss of the epithelium has been chosen as the clinical problem of this research work. The loss of the epithelial layer is frequently undetected by the assessors and is often only visible after the corneal surface is treated with diluted 1% fluorescein drops (**Figure 3.4**) and viewed under the cobalt blue lighting (**Figure 3.5**). This finding is possible because the abraded areas of the cornea retain the dye and fluoresce brightly under the cobalt blue light.

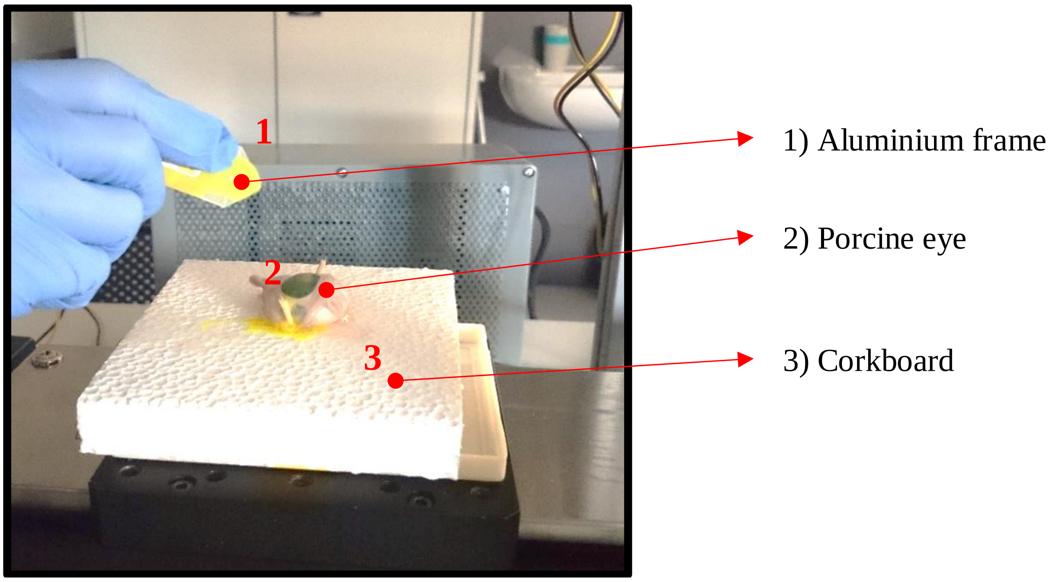

Figure 3.4: Staining process.

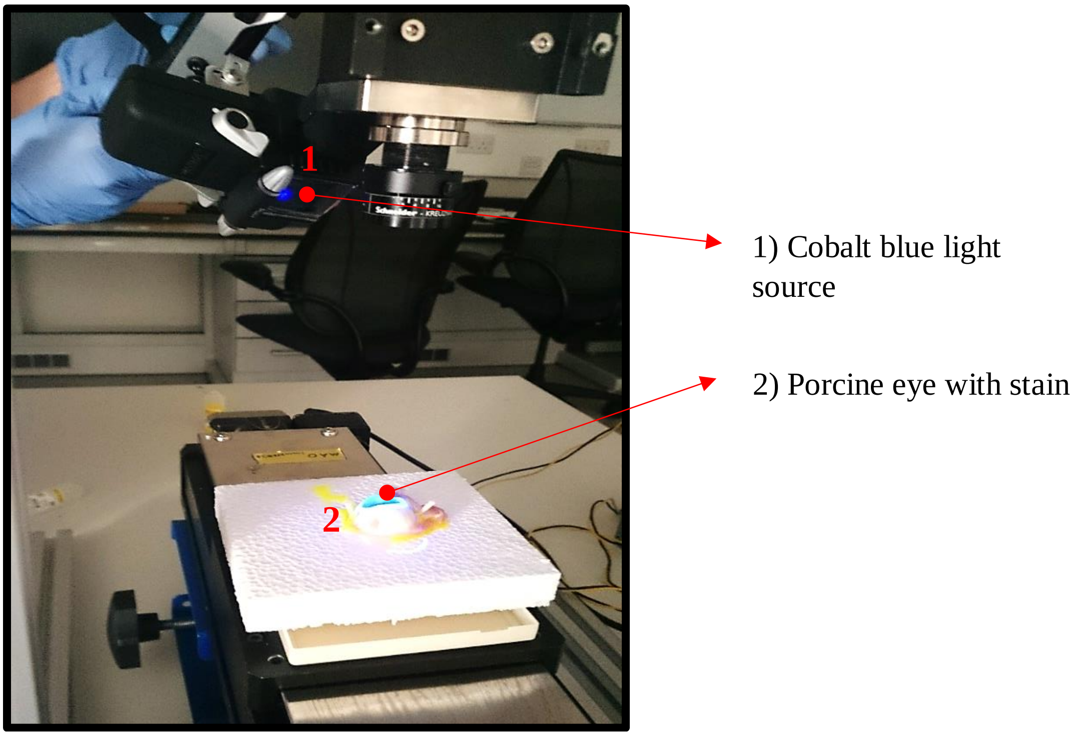

Figure 3.5: Blue lamp illumination source for the stained eye.

During this work, all ethical obligations, refer as safety and health regulation, risk assessment list for researcher, samples, and lab have been complied prior to the experiment works. The lab work sessions have been conducted according to the rules implemented by the governing organisations. All porcine eyes have been resourced from the by-products of the food industry. It means no animal been slaughtered purposely for this study.

The details about the sample preparation used have been previously reported [50]. The sample preparation started with frozen porcine eyes (dead tissues) were defrosted slowly in warm sodium chloride 0.9%. These eyes were moistened with sodium chloride 0.9% regularly throughout the experiment to prevent corneal over drying. When defrosted, they were fixed on a corkboard to minimise movement. The eyes were then placed approximately 10 cm below the camera for optimum image focus. Before image acquisition, the camera was calibrated using a white tile and checkerboard pattern (Figure 3.6) to obtain corrected reflectance data. Camera calibration is important to make sure the true parameters of the camera are correct to achieve high accuracy of image resolution.

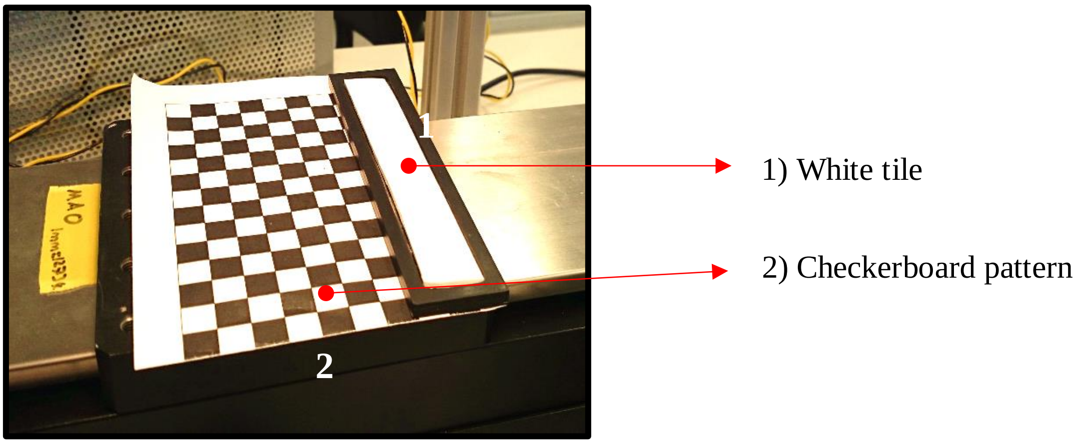

Figure 3.6: White tile and checkerboard paper for calibration.

3.1.2 HSI Corneal Epithelium Image and Data Collection

The image collections from group 1, group 2, and group 3 were captured using VIS-NIR camera have been included as the data of this study. The images from group 4 have been excluded due to the poor quality of the images because the epithelium layer hardly seen through the NIR camera. As shown in **Figure 3.7**, 25 hyperspectral images have been obtained from this study: 14 with corneal epithelial injury (abnormal) and 11 with completely intact corneal epithelium (normal).

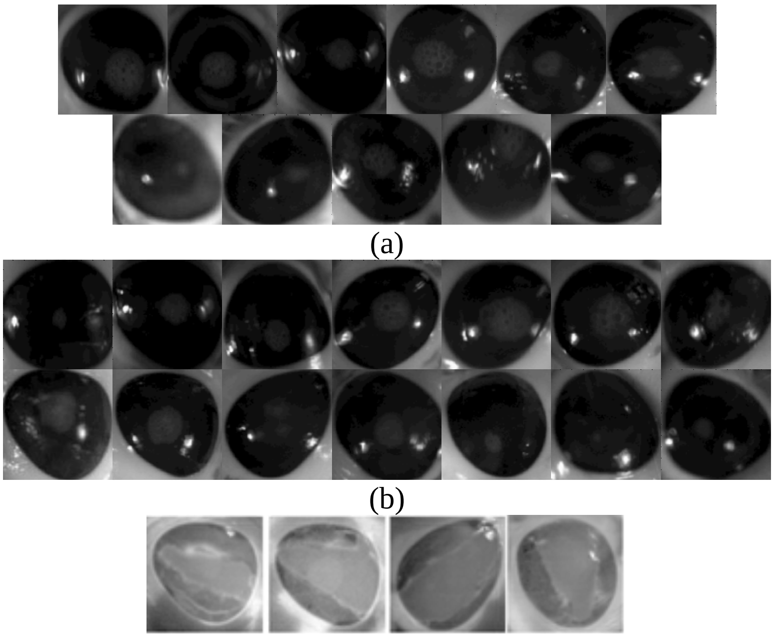

(a)

(b)

(c)

Figure 3.7: 25 hyperspectral images sliced at band-100. All images were normalised and resized to 100 by 100 pixels. (a) Rows 1 and 2 are images of healthy Corneas. (b) Rows 3 and 4 are images of corneas with induced epithelial injuries. (c) Row 5 shows the ground truth images.

All 25 eyes have been scanned without any fluorescein staining. Out of the 14 eyes with abnormal epithelium, four eyes have been randomly selected for the application of fluorescein stain and repeated scanning. The control group (ground truth images) is formed by the images from the stained eyes.

3.1.3 Preliminary Analysis - Properties of Corneal Epithelium Layer Based on Hyperspectral Images.

Biomedical engineering is a unique area that allows fusion between two distinct fields of engineering and medicine. The amalgamation of efforts from both fields promises progress via acquisition of information from tissues, cells, and organs through non-invasive assessment methods. **Figure 3.8** illustrates an identical sample captured by using a digital camera and a hyperspectral camera.

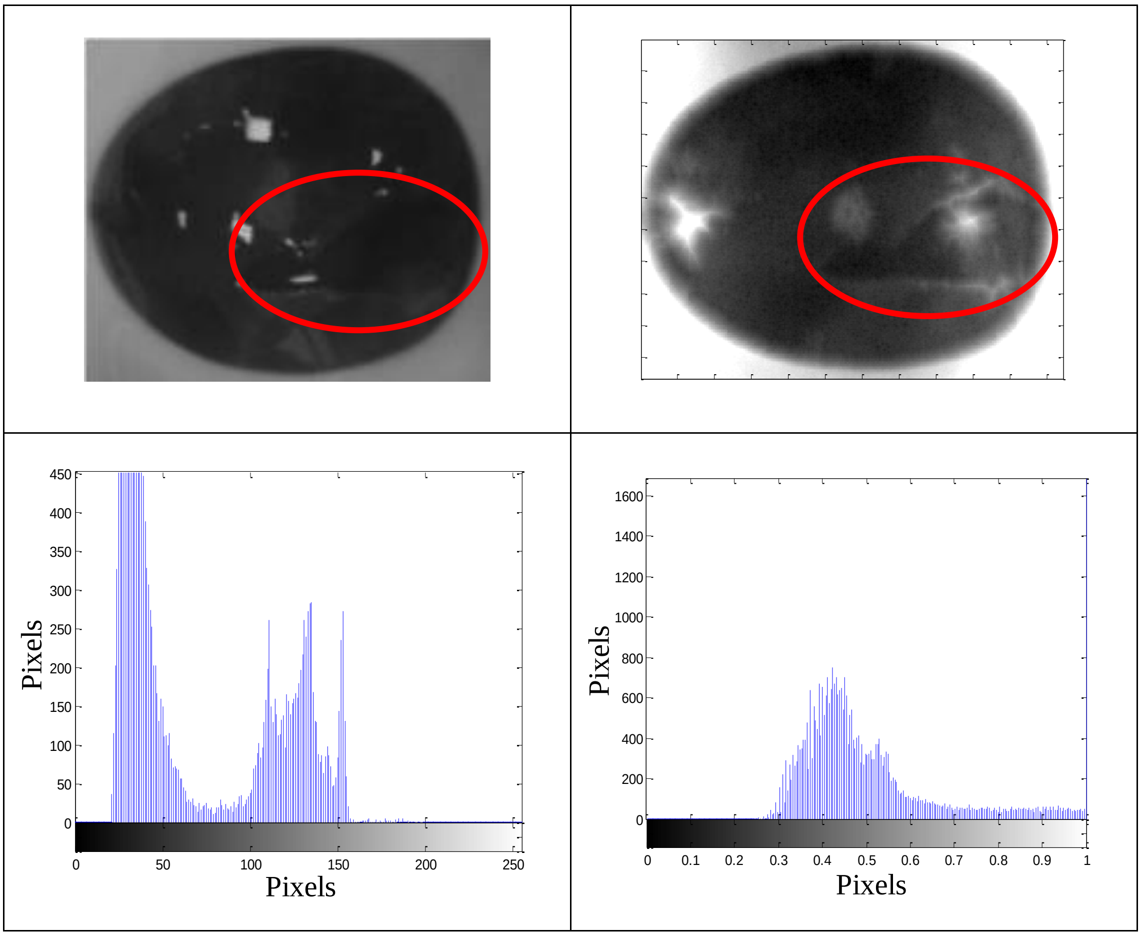

Figure 3.8: An identical sample is captured using the digital camera (on the left) and scanned with the hyperspectral camera (on the right) with their respective histogram.

Both images were compared, and the injured area (in circle) is more apparent and vivid in the hyperspectral image (image had been sliced from the selected band). Here, an investigation on the ability of a hyperspectral device in extracting data from tissues through wavelength spectrum is depicted. This highlights its potential in clinical diagnostics through simplification of procedures that can be carried out by clinicians to detect corneal injuries.

Hyperspectral imaging that ranged from 400 nm to 1000 nm visible wavelength was used to scan five porcine eyes (sample contained both injured and non-injured corneas). Five images were collected and named as group 1. In this experiment, eye staining was omitted as both healthy and injured eyes were identified by an eye expert. All samples were scanned and the raw data were saved into three-dimensional (3D) size of rows, columns, and depths.

The images of all the eyes were processed. The eye portrayed in **Figure 3.9** had been selected as it best represented the data that consisted of both injured and intact epithelium on its surface.

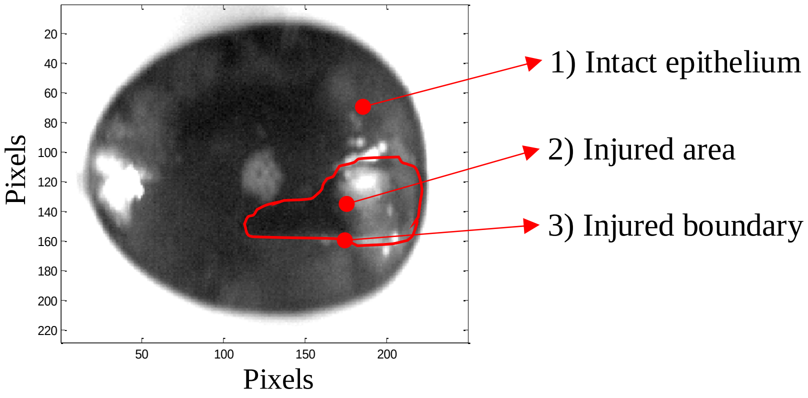

Figure 3.9: Sample of eye that consisted of normal and injured cornea.

Meanwhile, the eye displayed in **Figure 3.10** refers to a reference subject as it showed no identifiable surface injury. As such, reflectance spectrum analysis was performed for both eyes for comparison purpose.

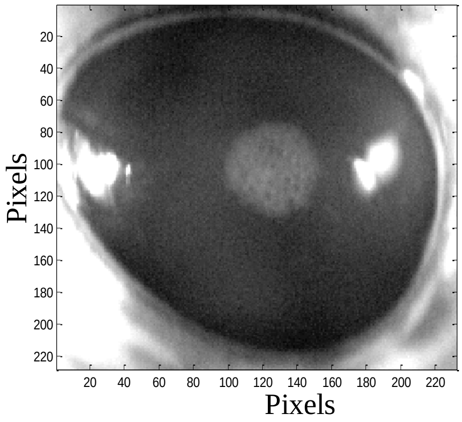

Figure 3.10: Sample of eye with normal cornea.

Figure 3.11 (a) shows random placement of pixels on both the injured area (labelled as 1) and the non-injured area (labelled as 2). The data retrieved from the pixel points of both areas were averaged and plotted, as presented in **Figure 3.11** (b).

Figure 3.11 (b) compares the reflectance spectra derived from both areas. As a result, a similar initial outline was displayed, but with a distinct separation in reflectance values from wavelength 548 nm until 748 nm. The corneal base tissue properties were likely to account for a similar spectrum outline, thus requiring further analysis for verification.

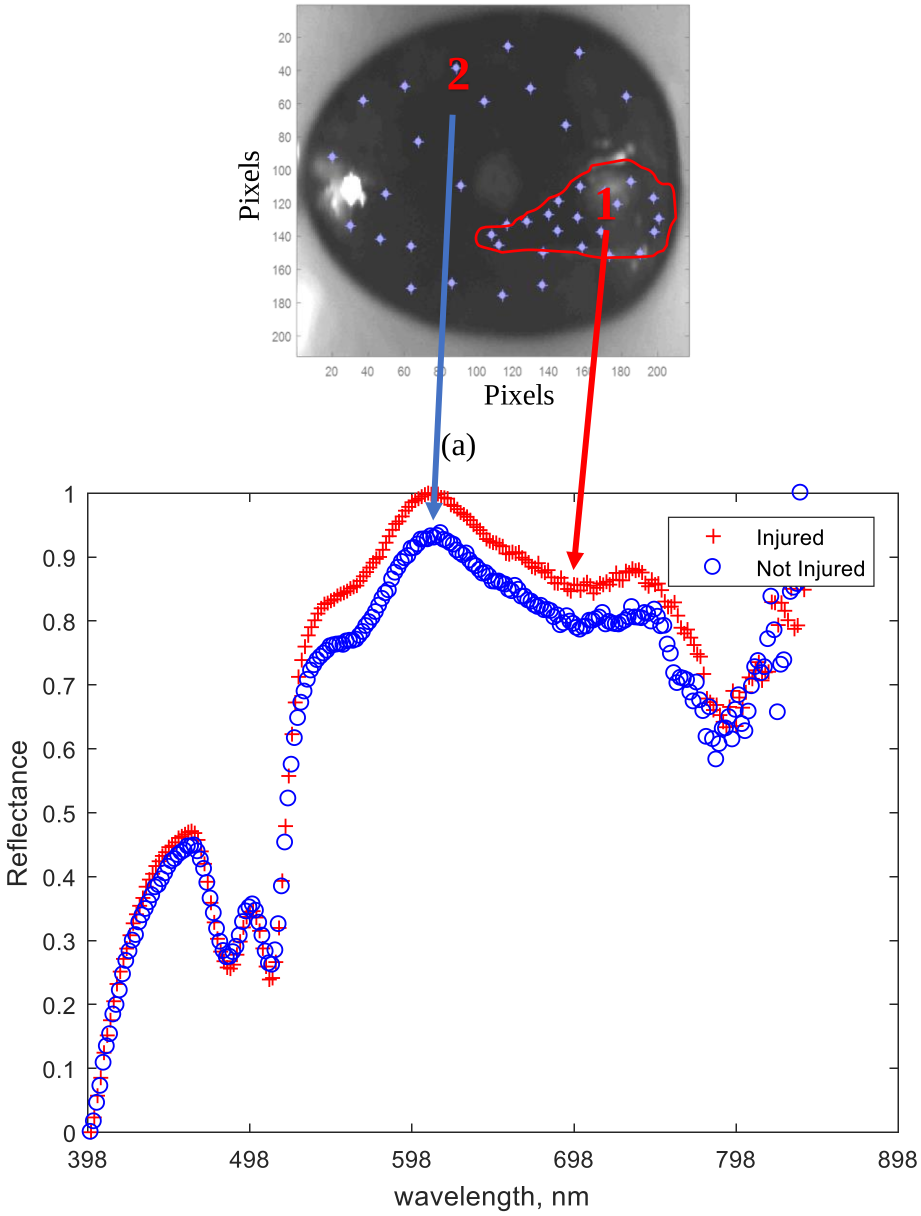

(a)

(b)

Figure 3.11: (a) Image sliced at band-150 (638 nm), selected pixels of two surfaces: 1- Injured surface, and 2- Non-injured surface. (b) Reflectance vs wavelength of both normal and injured surfaces.

On the contrary, when the pixel points were placed and distributed in identical areas on healthy eye, as portrayed in **Figure 3.12** (a), only slight gap variance had been noted in reflectance between both surfaces, which ranged from wavelength 398 nm until 798 nm (**Figure 3.12** (b)).

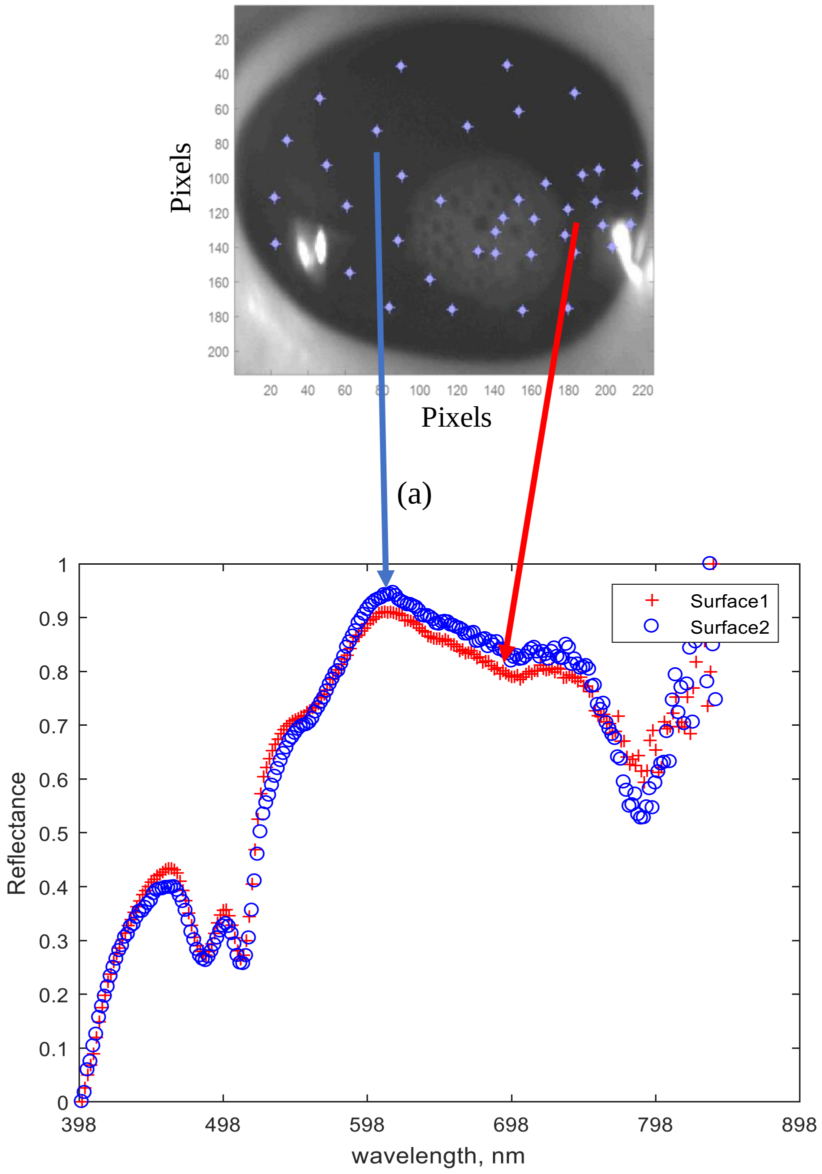

(a)

(b)

Figure 3.12: (a) Left: Sample of healthy eye, image sliced at band-150 (638 nm), (a) Right: Cornea area cropped with selected pixels at two surfaces: 1- surface 1, 2- surface 2. (b) Reflectance vs wavelength of surfaces 1 and 2.

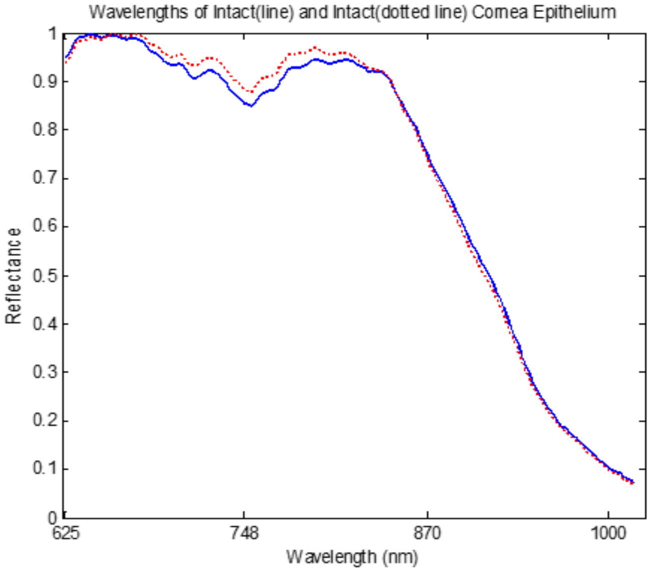

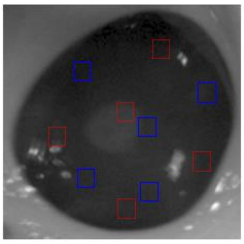

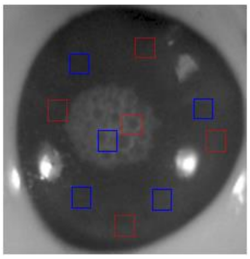

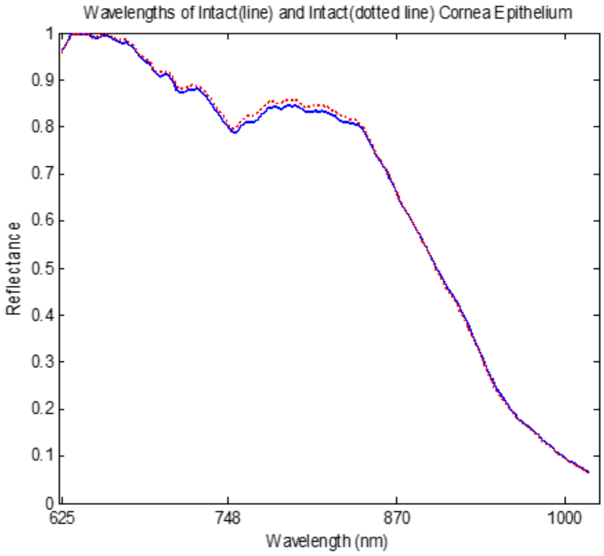

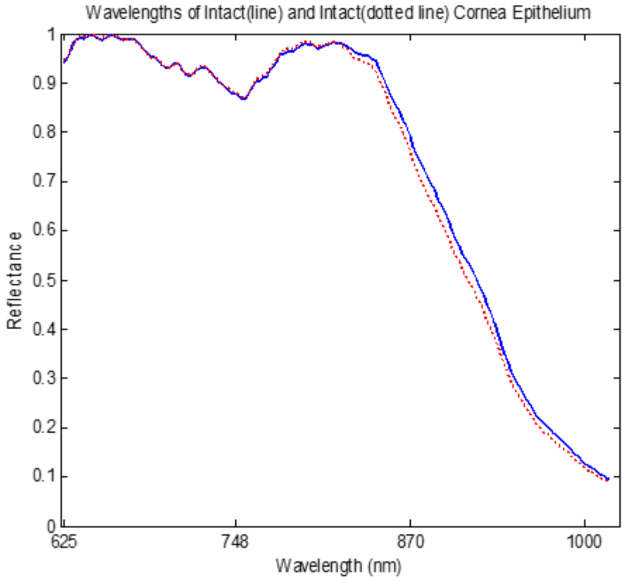

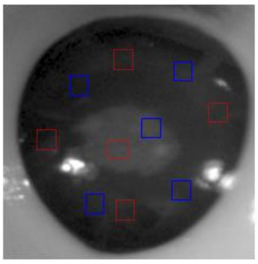

Figure 3.13: Signature reflectance of healthy eyes.

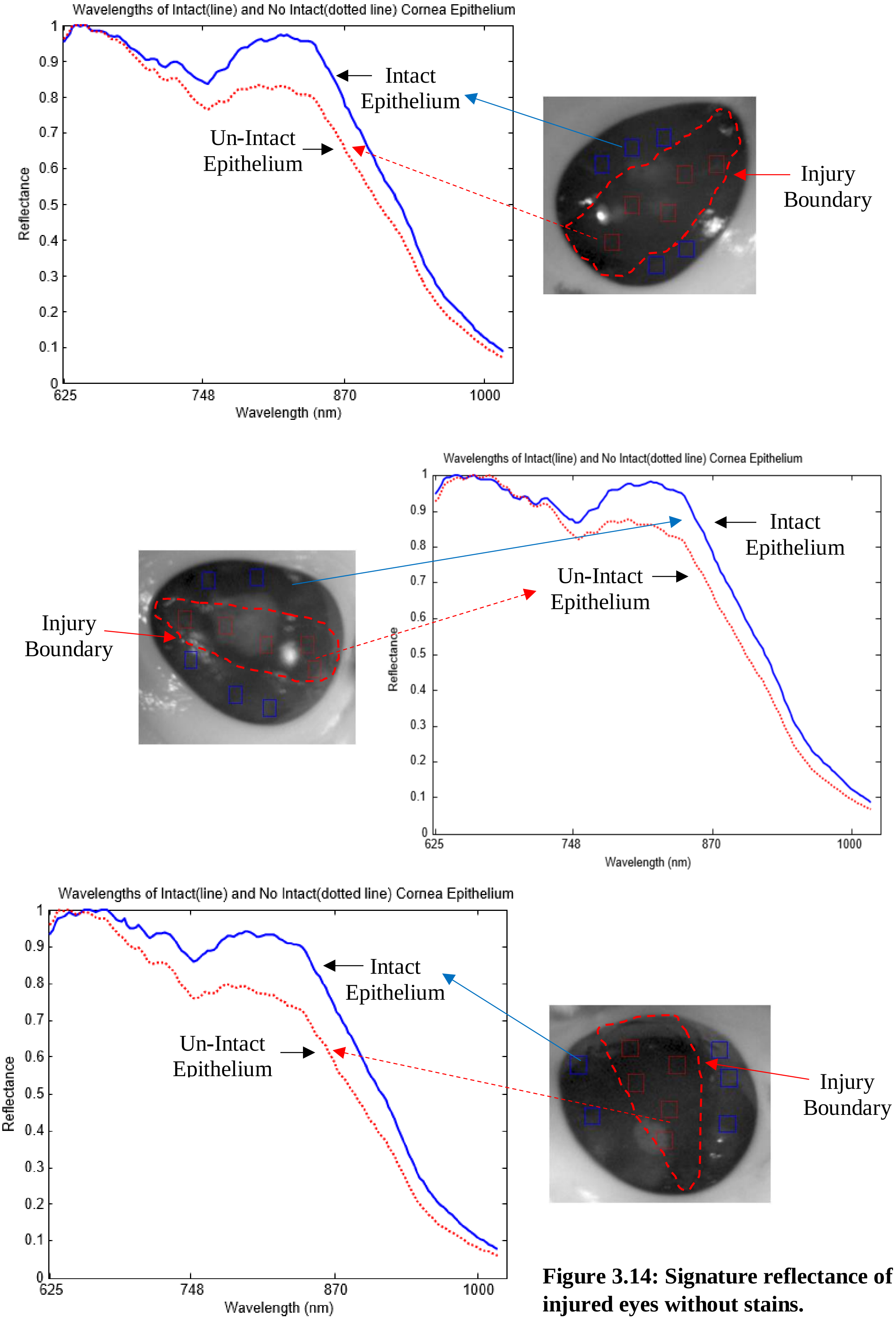

Figure 3.14: Signature reflectance of injured eyes without stains.

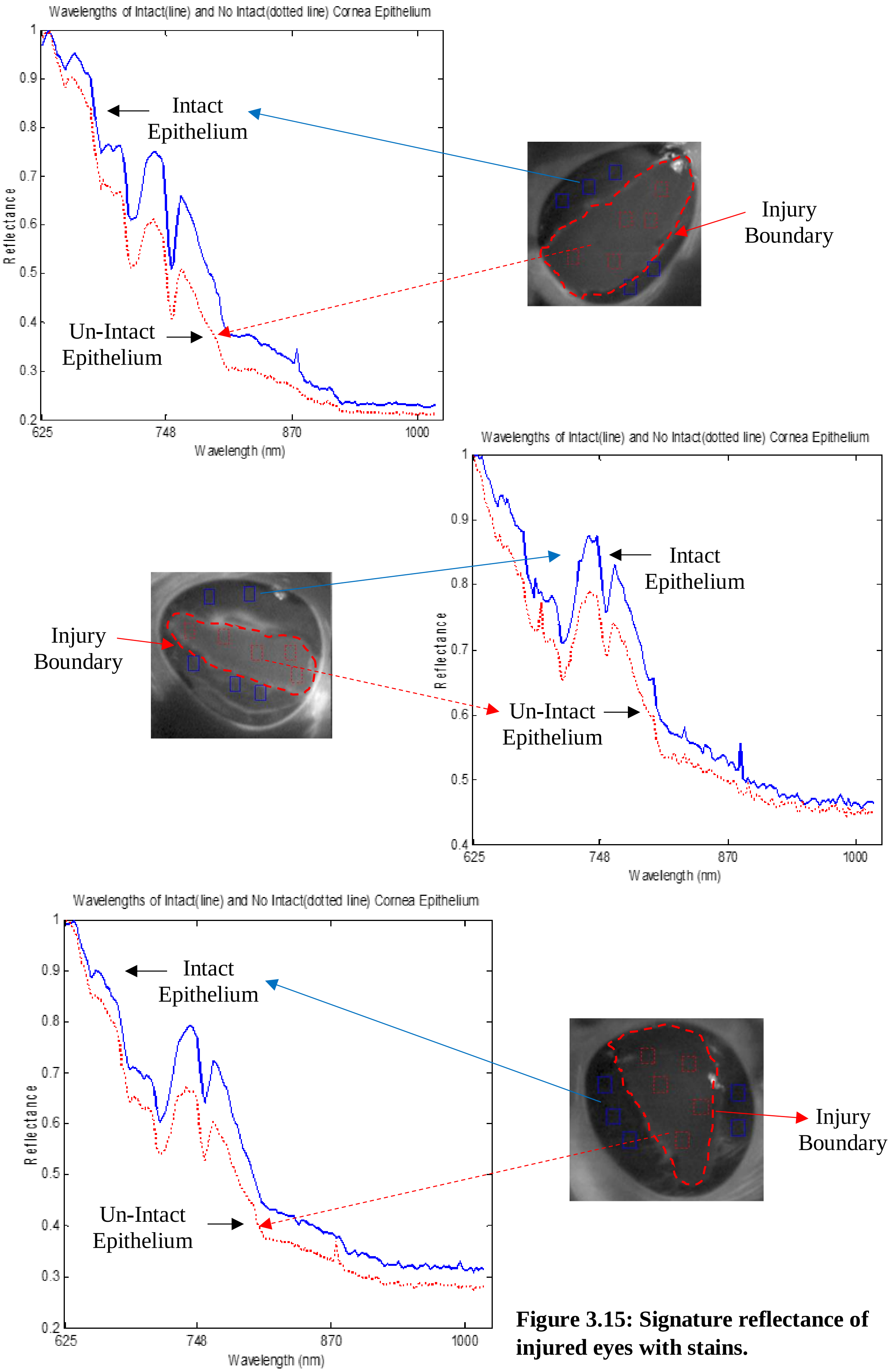

Figure 3.15: Signature reflectance of injured eyes with stains.

Figure 3.11 and Figure 3.12 image eyes obtained from group 1, to confirm that the reflectance signature show significant difference between intact and un-intact epithelium, image scanned from other groups were compared in term of reflectance signature depicted in Figure 3.13, 3.14, and 3.15. The reflectance signature of healthy eyes in Figure 3.12 and 3.13 show that no gap between two groups of random pixels were selected. Whereas, Figure 3.11 and 3.14 show signature gap between intact and un-intact of epithelium. This scenario is validated by eyes with stains, where the plot of reflectance shows signature distinction between injured and healthy area.

The injured surface was determined by slicing the images into several areas of interest. **Figure 3.16** (a), (c), (e), and (g) display the grey image at bands 518 nm, 698 nm, 758 nm, and 818 nm, respectively. The images at longer wavelengths revealed distinct shapes in regular arrangements that are likely to represent individual cells, although further analysis is required for confirmation. On the other hand, **Figure 3.16** (b), (d), (f), and (h) illustrates the structure in hue, saturation, and value (HSV) colour image.

The preliminary analysis revealed a gap in the reflectance spectrum between the non-injured and injured parts of the porcine cornea, thus suggesting further assessment of corneal tissue integrity. In fact, additional image processing as image enhancement with grayscale slices could reveal distinct tissue properties at varying wavelengths. This notion suggests a novel role for the hyperspectral image technology in the diagnostics of corneal tissues, apart from the conventional methods of microscopy.

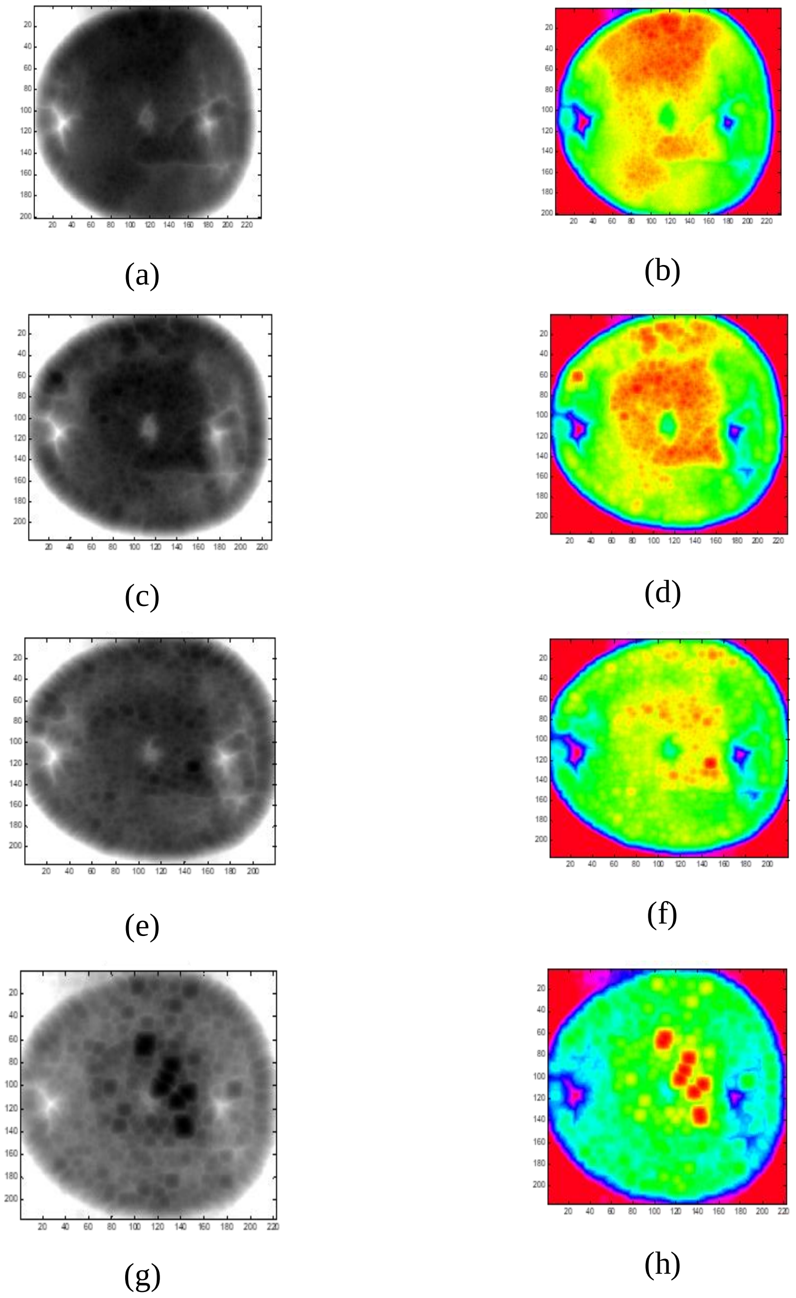
(a) (b)

(c) (d)

(e) (f)

(g) (h)

Figure 3.16: Images sliced at bands 518 nm, 698 nm, 758 nm, and 818 nm at first column of (a), (c), (e), and (g) represent grey scale images. The second column of (b), (d), (f), and (h) represent HSV colour images.

3.2 Digital Image Enhancement for Hyperspectral Image

Image enhancement is a process that transforms an original image when contrast is insufficient, or when a good quality of image with low noise is required for further analysis [65]. The methods used for enhancement vary according to the chosen imaging modality. For example, the methods used to enhance MRI images are unlikely to represent the best approach to enhance hyperspectral images taken in the visible near infrared band of the electromagnetic spectrum [66].

There is no universal enhancement algorithm that is effective for all types of images. The main goal of enhancement algorithms is to reduce noise and increase the contrast between the structures of interest and their surroundings. In addition, image enhancement improves and refines the image segmentation, especially for the images where the distinction between the normal and the abnormal tissues is unclear for the interpretation by human or automatic systems [65], [67]. The following section describes the HSI image pre-processing and the enhancement applied in this research work.

3.2.1 HSI Image Normalisation

The flat-field correction for data normalization before acquiring the image is an essential step of the HSI. During this step, the white balance and dark current measurements [68] are used to acquire the relative reflectance from the sample (**Figure 3.17**). The dark current of the sensor is recorded with the sensor being protected from the incoming light to measure the actual dynamic range of the sensor. In the meantime, the white balance material is calibrated at regular intervals for comparison of its reflectance properties with those of a spectralon probe, which compensate for the ageing or usage degradation of a white balance quality. Simultaneously, both measures can identify any corrupted or defected pixels in the pushbroom sensor of the hyperspectral camera. In addition, the data from the dark current and white balance measurements can be used to correct the measured material image. The main purpose of this correction is to eliminate artefacts and noise effects on the sample [62], computed with the following equation [36]:

$$Rs(\lambda) = \frac{Is(\lambda) - Id(\lambda)}{Ir(\lambda) - Id(\lambda)}\ x\ 100\% \qquad \text{Eq. 1}$$

where $Rs(\lambda)$ is the relative reflectance of the sample object; $Is(\lambda)$ is the sample or measured image; $Id(\lambda)$ is the dark image acquired when the light is absent by closing the lens with a cap; $Ir(\lambda)$ is the image obtained from the spectralon white bar, and; λ is the wavelength.

This image has been removed by the author of this thesis for copyright reasons.

Figure 3.17: Illustration of flat-field correction procedure: (a) original image, (b) flat-field background, and (c) processed image [69].

3.2.2 Brightness and Contrast Adjustment

Most of the captured images appear relatively dark due to their exposure during the image acquisition by the HSI system. These low-contrast dark images require brightness and contrast adjustment for a better visibility of the image details. Gamma correction (**Figure 3.18**) or power-law transformation, $s = r^{\gamma}$ is essential for contrast manipulation when the image is likely to be too dark [66]. The transformation can be obtained simply by varying the value of γ, according to the power-law curves, by setting $\gamma > 1$ to make an image darker, and vice versa.

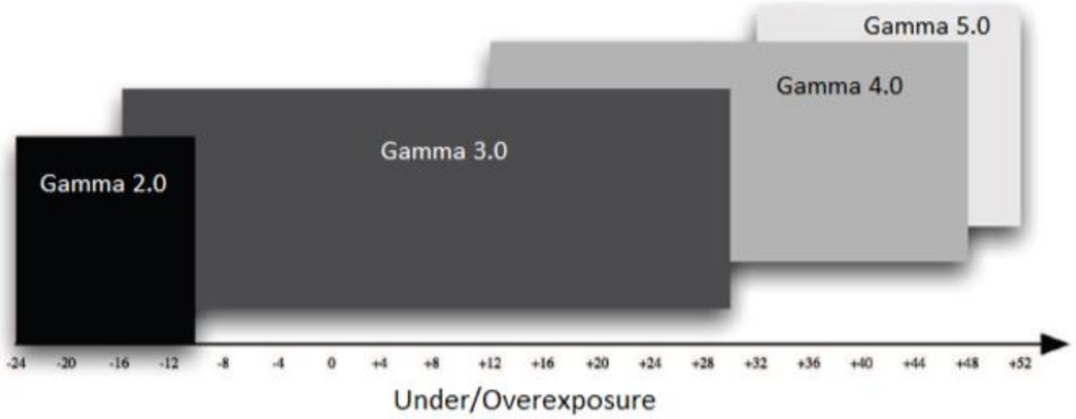

Figure 3.18: Gamma correction [70]**.**

3.2.3 Morphological Transformation

The mathematical morphological (MM) technique is widely used in the shape-based image processing for region segmentation, threshold processing, noise elimination, and hole filling [65]. MM is particularly useful in describing shapes using a set theory by the structuring element (SE). Typically, SE is chosen with the same size and shape as the objects to be processed in the input image. For example, to detect lines in an image, a linear SE is created. There are two categories of SE in gray-scale morphology: flat and non-flat [66]. Flat SE is two-dimensional (2D) while non-flat SE is three-dimensional (3D). SE consists of a matrix of 0s and 1s, which is typically much smaller than the image being processed. The origin, which is a centre of the SE, identifies the pixel of interest and defines the neighbourhood used in the processing of each pixel.

These SEs are also considered in the primitive operations, namely erosion and dilation processing. The following explanation focuses on the erosion operator as it is used in this research. Erosion is applied to two sets of matrices: the gray-level image matrix $A(x,y)$, and the structural element matrix $B(u,v)$. Erosion of A by B is the set of all points z in B, translated by z, is comprised of A, written $A \theta B = \{z | B_{z-} \subseteq A\}$ [66].

Furthermore, a spherical or ball shape non-flat SE is used to probe the image, which is constructed in 3D structure and consists of the radius in the x-y plane. Then, z value is added to define the third dimension. Spherical SE is used with a radial decomposition [71] to accelerate such operations as with the top hat and rolling ball transformations [72]. This non-flat SE also improves the performance of morphological filtering in terms of the smooth opening and closing of electrocardiogram (ECG) signals [73]. Although disk SE is commonly used for medical images [74], it is unlikely to be effective in this study (**Figure 3.19b**). In contrast, the spherical shape (**Figure 3.19c**) removes the glare while preserving the vital image features (boundary of abnormal tissue) because it has been eroded by a spherical SE about the size of the glare. This glare must be removed from the image for further processing.

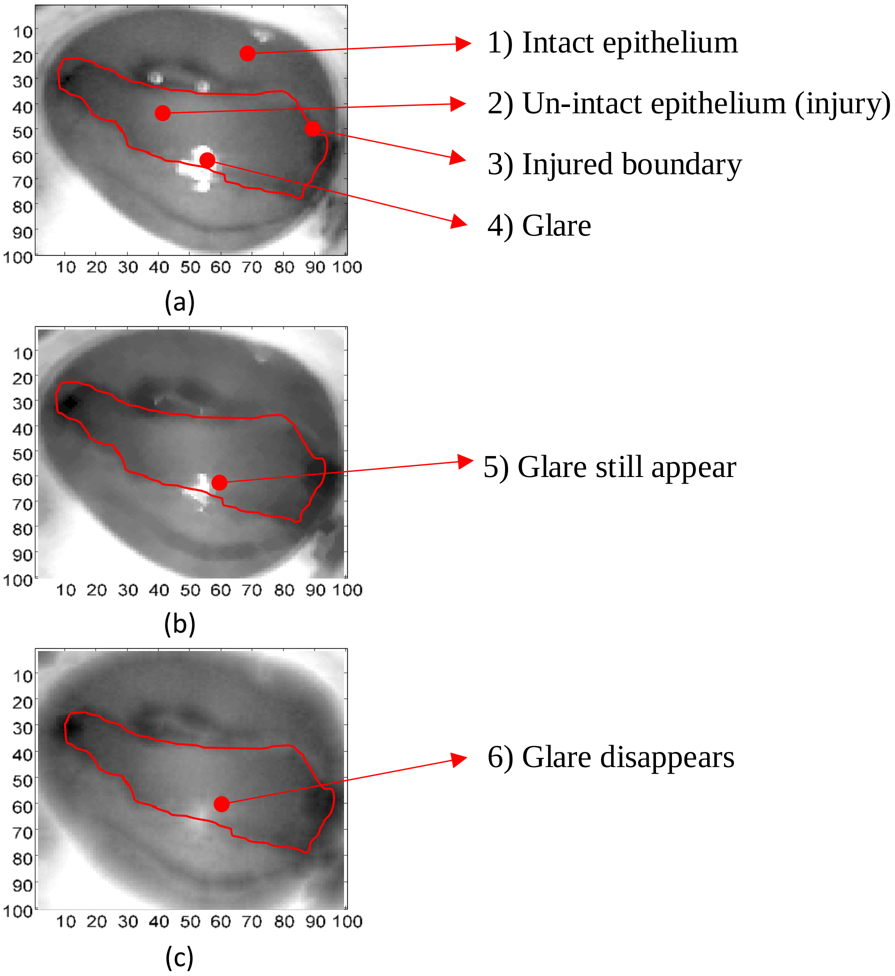

Figure 3.19: Eroded Image. (a) Original image. (b) Eroded with 'disk' SE. (c) Eroded with 'spherical' SE.

3.2.4 Laplacian of Gaussian Filter (LoG)

The Laplacian of Gaussian (LoG) is one of the earliest edge detectors introduced by Marr-Hildreth [75]. The LoG [66] can detect boundaries or edges at different scales while overcoming the intensity changes from the surface disruptions, reflectance, or illumination. The combination of a 2D Gaussian function (image smoothing), Eq.2, and a Laplacian operator (edge detection), Eq.3, gives the expression in Eq.4.

$$G = \exp\left(-\frac{x^2+y^2}{2\sigma^2}\right) \qquad \text{Eq. 2}$$

$$\nabla^2 = \left(\frac{d^2}{dx^2} + \frac{d^2}{dy^2}\right) \qquad \text{Eq. 3}$$

$$\nabla^2 G(x,y) = \left[x^2 + y^2 - \frac{2\sigma^2}{\sigma^4} \exp\left(-\frac{x^2+y^2}{2\sigma^2}\right)\right] \qquad \text{Eq. 4}$$

By applying LoG to hyperspectral images, a variety of images were generated, subject to alterations in its parameters (**Figure 3.20**). Larger values of sigma caused the edges to blur. Meanwhile, the smaller values led to detailed and sharp detectable edges but prone to noise.

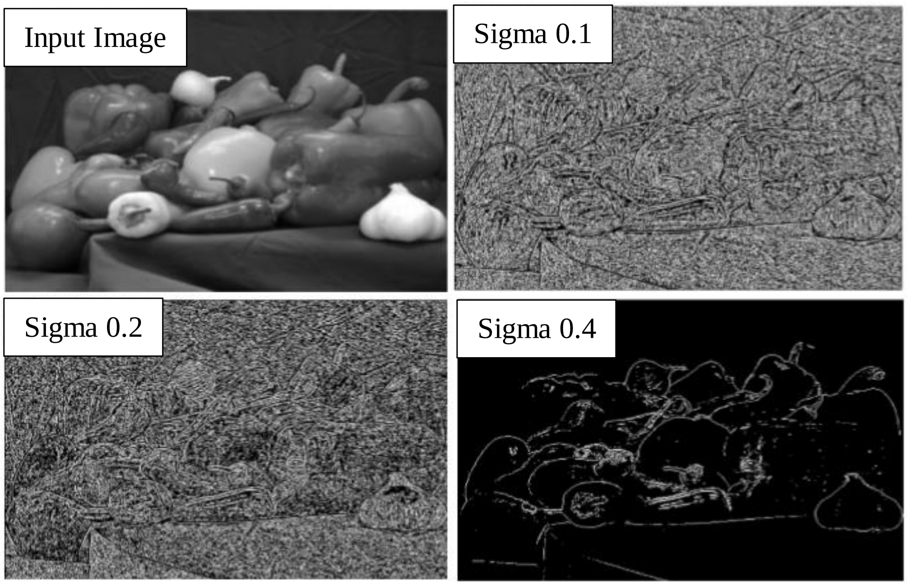

Figure 3.20: LoG operation with different value of sigma [76]**.**

3.2.5 Image Subtraction

Image subtraction in this work is performed to enhance visibility a region of interest as shown in **Figure 3.21**. Let *g*(*x*,*y*) denotes an image difference by the subtraction of PC1

$f(x,y)$ from PC10 $h(x,y)$ or vice versa; forming, $g(x,y) = f(x,y) - h(x,y)$ or $h(x,y) - f(x,y)$.

The image differences are enhanced with details as described previously [66].

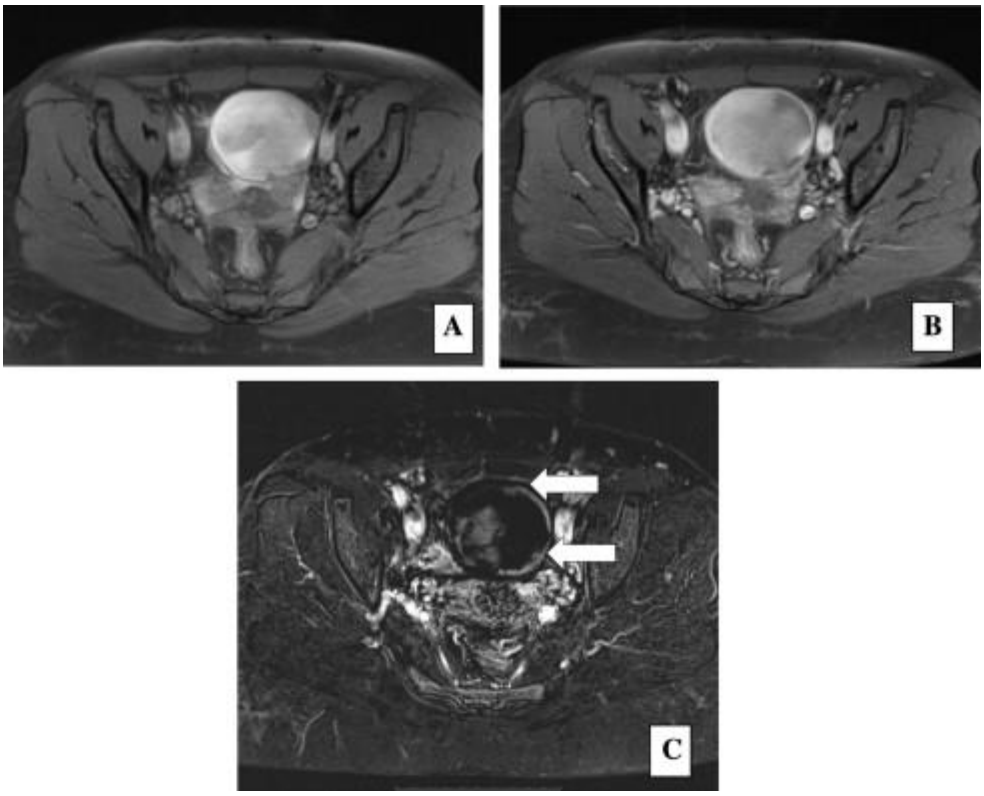

Figure 3.21: Pre and postcontrast enhanced MRI images with fat suppression (A and B) of the pelvis in female patient showing a large ovarian lesion exhibiting a hyperintense signal in both images. Subtraction image (C) shows multiple mural solid enhancing nodules seen along the wall of the lesion (arrows). The possibility of a mucinous ovarian cystic neoplasm probably of malignant nature was suggested and was confirmed histopathologically [77]**.**

3.3 The Dimensional Reduction of Hyperspectral Image

3.3.1 Principal Component Analysis (PCA)

With 3D structures, i.e. 2D in the spatial domain and 1D in the spectral domain, HSI contains a massive volume of data due to a large number of spectral bands used. This causes three challenges during the data collection: (1) high data redundancy due to the high correlation with the adjacent bands; (2) large variability of hyperspectral signatures, and; (3) enormous dimensionality [48].

In overcoming the above issues, PCA [78] which is a popular image transformation method has been employed in this research work. PCA is a form of unsupervised learning method commonly used to transform an image from high into low dimensional space [79]. In this study, several principal components with the maximum variability have been selected for the subsequent processing stages. This algorithm has been previously described in the hyperspectral image classification [79]. The method includes the mean subtraction, computation of covariance matrix, calculation of the eigenvectors and the eigenvalues, selection of components, and formation of feature vectors to derive a new data set. Additionally, dimensional reduction or band selection techniques have been applied to reduce the computational time and minimize the error of parameter estimation, i.e. the feature mean [80].

As an alternative to the conventional PCA, structured covariance PCA has been proposed [81] leading to the introduction of folded-PCA [82]. In this research, PCA has been used to transform correlated data into the uncorrelated features known as the principal components (PCs). This allows a smaller number of bands to be selected, reducing the used subspace to best describe the resulted data for clinical interpretation. In other words, PCA projects the whole data set onto different subspaces to find components containing the maximum variances, as reflected by the corresponding eigenvalues. Considering its benefits, this study has, therefore, employed PCA to perform a concise feature extraction and selection [77].

The background of mathematical expression used in this research work has been previously described [48], [79]. Each image in the spatial dimension $m \times n$ pixels is transformed into an image vector consisting of the spectral wavelength N-dimensional samples and into one image matrix *M*, *[ImgVec1:…: ImgVecN]*. The mean vector (Eq. 5) for every image vector, $xi = [x_1, x_2, \ldots, x_N]^T$ is computed and transformed into a covariance matrix (Eq. 6). The covariance matrix is then used to generate eigenvectors *(e1, ..., en)* and corresponding eigenvalues *(λ1, ..., λn)*. Subsequently, the eigenvectors are arranged in a higher to a lower order of eigenvalues to form the PCs that correspond to the number of hyperspectral bands. The mean vector and covariance matrix are computed as follows:

Mean vector:

$$\bar{m} = \frac{1}{M} \sum_{i=1}^{M} [x_1, x_2, \cdots, x_N]^T \qquad \text{Eq. 5}$$

Covariance matrix:

$$Covx = \frac{1}{M} \sum_{i=1}^{M} (x_i - \bar{m})\,(x_i - \bar{m})^T \qquad \text{Eq. 6}$$

where *M* is an image dimension, *x* is image pixel, and *T* denotes the transpose operation.

In conventional PCA, mean vector and covariance matrix are computed to the hypercube data which requires a large amount of memory. This issue can be resolved by splitting them into four approaches using the structured covariance PCA (SC-PCA) scheme. The SC-PCA includes; pixel-based (Eq. 7), row-based (Eq. 8), column-based (Eq. 9), and band-based approaches (Eq. 10). As a result, SC-PCA provides a rapid processing time with a smaller memory requirement which is applicable for the real-time application.

Pixel-based:

$$C_{pixel} = \sum_{i=1}^{RC} P_i {P_i}^T \qquad \text{Eq. 7}$$

Row-based:

$$C_{Row} = \sum_{r=1}^{R} P_r^R \, [P_r^R]^T \qquad \text{Eq. 8}$$

Column-based:

$$C_{Column} = \sum_{c=1}^{C} P_c^C \, [P_c^C]^T \qquad \text{Eq. 9}$$

Band-based:

$$C_{Band}(i,j) = vec(P_{b=i}^B)[vec(P_{b=j}^B)]^T \qquad \text{Eq. 10}$$

Where C_{pixel}, C_{Row}, C_{Column} , $C_{Band}(i,j)$ are covariance matrix, P_i , P_r^R , P_c^C , $P_{b=i}^B$ are partial covariance matrix of pixel, row, column, and band, respectively, and; T denotes the transpose operation. As with the SC-PCA, the advantage of the folded-PCA is the reduction in memory and computational cost. The algorithm is explained in [82]. **Table 3.2** shows the memory requirement for the three types of PCA. It illustrates how the data matrix and the covariance matrix computation of conventional PCA demand a higher memory space when compare to the others.

Table 3.2: Computational size requirement for the three types of PCA

PCA	Data Matrix Size	Covariance Matrix
Conventional	BxRC	RCxRC
Pixel-based SC-PCA	Bx1	Sum of pixels
Row-based SC-PCA	BxR	Sum of Rows
Column-based SC-PCA	BxC	Sum of Columns
Band-based SC-PCA	RxC	CxC
Folded-PCA	RxC	CxC

Note: B is bands, R is rows/height, and C is columns/width

3.4 Digital Image Classification

3.4.1 Image Feature Extraction

Feature extraction is conducted prior to the image classification, whereby the most relevant information of the input data is transformed into a set of features. Colour, gray level, shape, and histogram are the examples of features that can be used to categorize images into different classes. Image segmentation is commonly used in the feature extraction [79]. Nevertheless, to reduce the computational time, the central moment of the histogram has been used in the present study for image classification without segmentation.

The central moment of the histogram or also known as the first-order statistics provides information related to the gray level distribution. Four features are represented by the first, the second, the third, and the fourth moments, i.e. mean, standard deviation, skewness, and kurtosis. In this study, a combination of 2D features has been used for the feature selection to reduce redundancies. Subsequently, the classification has been performed to discriminate between the injured and the healthy cornea. For comparison, the feature extraction with the pre-trained AlexNet is also presented. These methods are further explained in Chapter 5.

3.4.2 Support Vector Machine – Gaussian Radial Basis Function (SVM-GRBF)

SVM is commonly used for the machine learning applications due to its capability to work with different types of the kernel or covariance function [83] by the dot product rule. Based on the 2D-image feature distribution obtained from the histogram, it is not possible to separate the two classes of image data by a linear transformation in the input space. Therefore, a non-linear SVM classifier has been employed with the Gaussian radial basis function kernel, as its performance in the hyperspectral remote sensing classification is better than the SVM-linear, the K-NN classifier, or the standalone of RBF classifier [84]. The linear and non-linear SVM are represented by Eq. 11 and Eq. 12, respectively:

$$f(x)_{linear} = \sum_{i \in sv} \alpha_i y_i \, (x_i, x') + b \qquad \text{Eq. 11}$$

$$f(x)_{non-linear} = \sum_{i \in sv} \alpha_i y_i \, K(x_i, x') + b \qquad \text{Eq. 12}$$

where $\alpha_i y_i$ is a data point, $K(x_i, x')$ is a kernel, and b is a bias.

Further, the GRBF kernel which is represented as $K(x_i, x')$ in Eq. 12 is denoted as Eq. 13:

$$K_{GRBF}(x_i, x_j) = \exp\left(-\frac{|x - x_i|^2}{2\sigma^2}\right) \qquad \text{Eq. 13}$$

where σ is the width of the radial basis function, and different values of width will affect the boundary of classification between normal and abnormal.

Data normalization has been conducted before training the model to ensure that all attributes have the same importance. In this paper, each column of the feature vector in both the training and the testing sets has been normalised to a length of 1.

3.4.3 Convolutional Neural Networks (AlexNet)

Recent advances in deep learning made tasks such as image and speech recognition possible. Deep learning is a subset of machine learning algorithms that is very good at recognizing patterns but typically requires a large number of data [97]. Deep learning excels in recognizing objects in images because it is implemented using three or more layers of artificial neural networks whereby each layer is responsible for extracting one or more features of the image.

On the other hand, neural network [98] refers to a computational model that works in a similar way to the neurons of the human brain. The function of each neuron is to take an input, perform several operations, and then pass the output to the following neuron. For example, the purpose of this research is to teach the computer to recognise cornea images and classify them into the categories between healthy or injured. Hence, the computer is required to learn (training) how a healthy and an injured cornea look like before it is able to recognize (testing) a new image. In regard to this, the more injuries sample the computer sees, the better is the ability of the computer to recognize injured cornea which is also known as supervised learning. This task starts by labelling the images, followed by the process of recognizing patterns that are present in the images which are absent from the others, and finally building its own cognition. In other words, this process is also known as machine learning [99].

Computers are able to perform computations on numbers but has no ability to interpret images in the similar way human does. In the case of machine learning, the images have to be converted to numbers to help the computer to understand. There are two common ways that can be employed in image processing as follows: (1) Grayscale involves the conversion of the image to grayscale with the range of gray from white to black. Next, each pixel will be assigned a value based on the darkness of the grayscale. In addition, all the numbers will be put into an array for the computation to be performed, and (2) RGB allows colours to be represented as RGB values which involves the combination of red, green, and blue ranging from 0 to 255. Next, the RGB value of each pixel can then be extracted and the result can be put in an array for interpretation.

A new image that is interpreted by the computer will be converted to an array using the same technique, followed by the comparison of the patterns of numbers against the existing known objects. The computer then allots confidence scores for each class. In this case, the class with the highest confidence score is usually considered as the predicted one.

One of the most popular techniques in improving the accuracy of image classification is convolutional neural networks (CNNs) [100]. This technique involves a special type neural networks that functions similarly as the regular neural network, except that it has a convolutional layer. The image is broken up into a number of tiles instead of feeding the whole images as an array of numbers, whereby each tile will be predicted by the algorithm. Finally, the computer will try to predict what is in the picture based on the prediction of all the tiles. More importantly, this allows the computer to parallelise the operations and detect the object regardless of its location in the image.

A standard neural network known as AlexNet [85] consists of 1.2 million high-resolution images and can be used to classify 1000 different classes. It comprises millions of parameters, hundreds thousand neurons, five convolutional layers (some of which consist of max-pooling layers), and three fully-connected layers with a 1000-way SoftMax

(**Figure 3.22**). The AlexNet has been used on small data for fingerprint detection [86] on a pretrained model with good results. Furthermore, AlexNet has been trained on rich feature representations for a wide range of images.

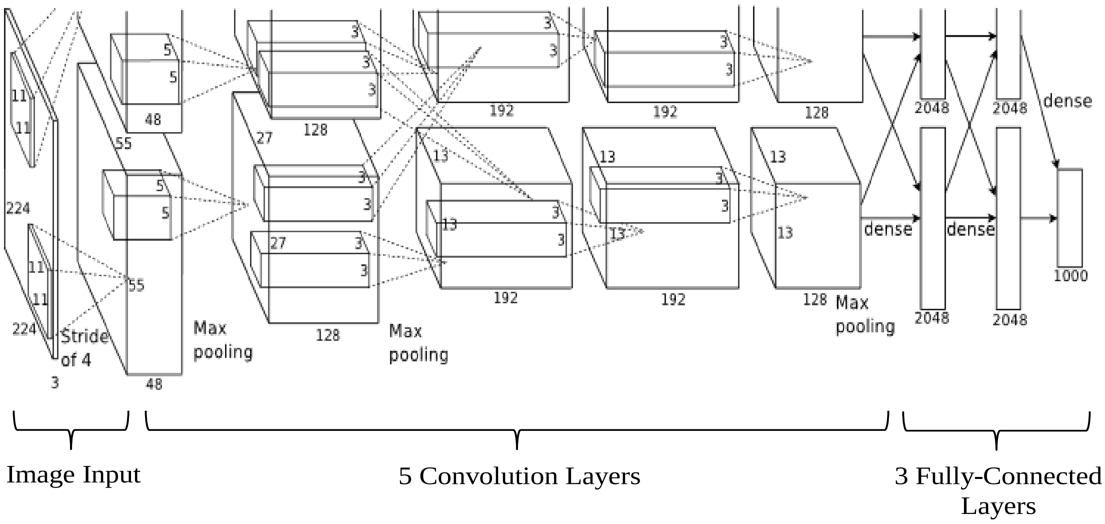

Figure 3.22: AlexNet architecture.

As AlexNet is designed to classify 1000 images, it is not suitable (overfitting concerns) for this research work to train the network from scratch which has a small data set and a limited number of classes (healthy and injured). Therefore, the pre-trained (**Figure 3.23**) AlexNet with two approaches have been used to classify the data, namely transfer learning [87] and deep feature extraction [88], [89] with some modification parameters from the old AlexNet model (see detailed explanation in Chapter 5).

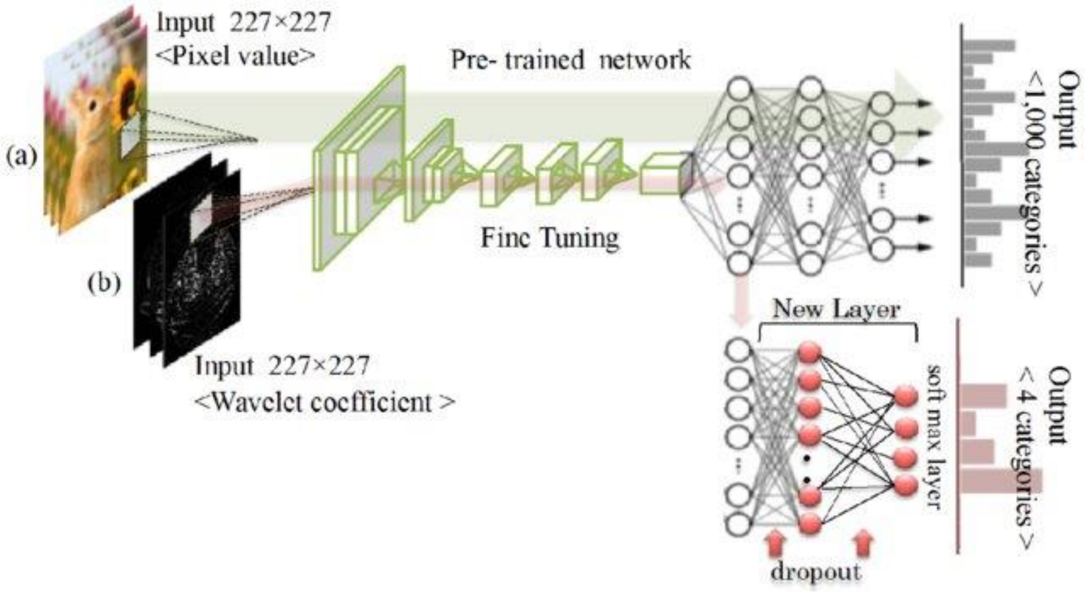

Figure 3.23: Example of pre-trained with transfer learning approach [90].

To understand well the AlexNet structure, key terms used describe as follows:

Convolution layer – A layer designates a filter by which examine a subset of the image, and subsequently scans the whole image through image filter (**Figure 3.24**). Convolution layer defines the filter size and stride.

Filter – The filter looking for specific features e.g. edges on the image.

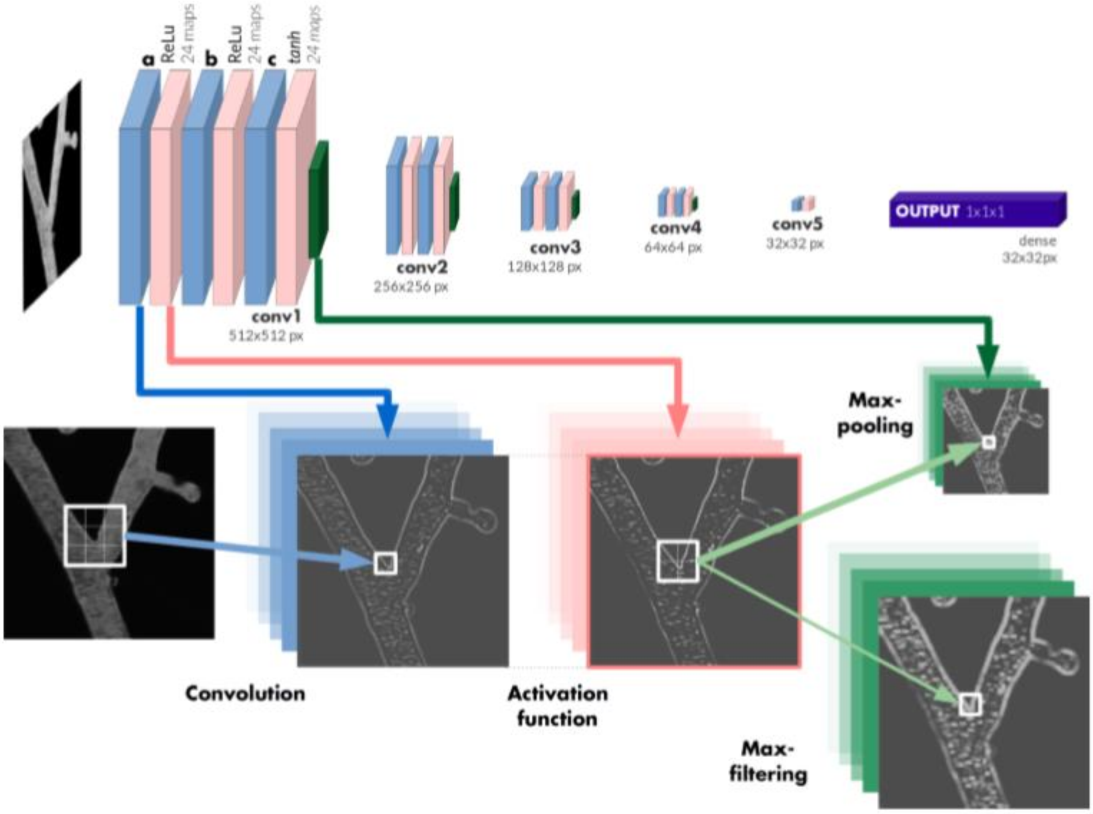

Figure 3.24: Convolution layer image output [91]**.**

Stride – An alternative method for down sampling the spatial resolution of the feature mappings. The stride length defines how many steps take when sliding filter across an image. For example, a stride length of one, moving the filter one unit as is scanned an entire image.

Max pooling – Pooling layer used to compress information rather than extract image features. Similar to convolution layer, it defines filter and stride size. Maximum pooling refers to the selection of maximum value inside the filter in every scan (**Figure 3.25**).

Figure 3.25: Max pooling process [92]**.**

Rectified linear units (ReLU) – Activation function where output is 0 when image pixel smaller than 0, otherwise, no changes (**Figure 3.26**). It is applied after convolution layer to solve vanishing gradient and to induce sparsity in the features.

Figure 3.26: Rectified linear units (ReLU) function [92]**.**

Fully connected (FC) – In FC, image matrix flattened into vector and feed it into a FC layer as neural network. Feature map matrix will be converted into vector, the features were combined together to create a model (**Figure 3.27**). From here, an activation function such as softmax to classify the outputs as injury or healthy.

This image has been
removed by the author
of this thesis for
copyright reasons.

Figure 3.27: CNN with fully connected (FC) and softmax layer. Model 1 has a FC layer of 1024 neurons, while Model 2 presents 32 neurons [93]**.**

Dropout – To deal with overfitting where the neuron weight has been reduced as shown in **Figure 3.28**.

This image has been
removed by the author
of this thesis for
copyright reasons.

Figure 3.28: Neural network without and with dropout
(Source: N. Srivastava et.al., Dropout: A Simple Way to Prevent Neural Networks from Overfitting, 2014)

Softmax – Often used in the final layer after fully connected layer. Softmax is output for the probabilities range of 0 to 1. It calculates a probability for every possible class and sum of all probabilities is one.

3.5 Summary

The new data collection of cornea epithelium using the pushbroom HSI system is presented in this chapter. To the best knowledge of the author, hyperspectral image collection presented in this chapter is a novelty of this study. This is first work to use HSI for corneal epithelium injury detection. Four series of experiments for images with and without eye staining have been captured via a scanning process. The analysis has mainly focused on the eyes without staining while the stained eyes have been used as the ground truth images to identify the injured area. Two types of camera, VIS-NIR (400 nm to 1000 nm) and NIR (950 nm to 1700 nm) have been used.

The resulting images from the VIS-NIR have been utilised for the subsequent process, while the images captured from the NIR have been rejected due to the low image quality, where the intact and un-intact corneal epithelium layer were difficult to distinguish. However, this study has not investigated the valid reason for the poor outcome from NIR. Overall, the literature on the background knowledge of image analysis will be used has been categorised into image enhancement, dimensional reduction, and image classification with each being discussed appropriately.

CHAPTER 4

A NEW HYPERSPECTRAL IMAGE ENHANCEMENT (8-SHIE)

A corneal injury may be visible, but the severity of damage cannot be easily determined by the naked eye. Quantifying the defect or assessing each layer on the cornea is a challenging task even to an expert, because the appearance is transparent and it is comprised of a tiny structure. Therefore, the preliminary experiment, which is referred as group 1, tested five samples. This experiment determined if hyperspectral imaging is possible in providing and revealing significant information from the cornea in general and especially in the epithelium layer.

This chapter also presents information on how hyperspectral images were processed from raw images that contained a large amount of information into formatted data file to minimise storage space for post-processing. The analyses on spatial and spectral signatures are presented towards image enhancement so as to provide objective interpretation.

4.1 Spectral Bands Post-Processing

4.1.1 Spectral Binning

The Environment for Visualizing Images (ENVI) software program was applied to read the raw image, a sample illustration of which is given in **Figure 4.1**..

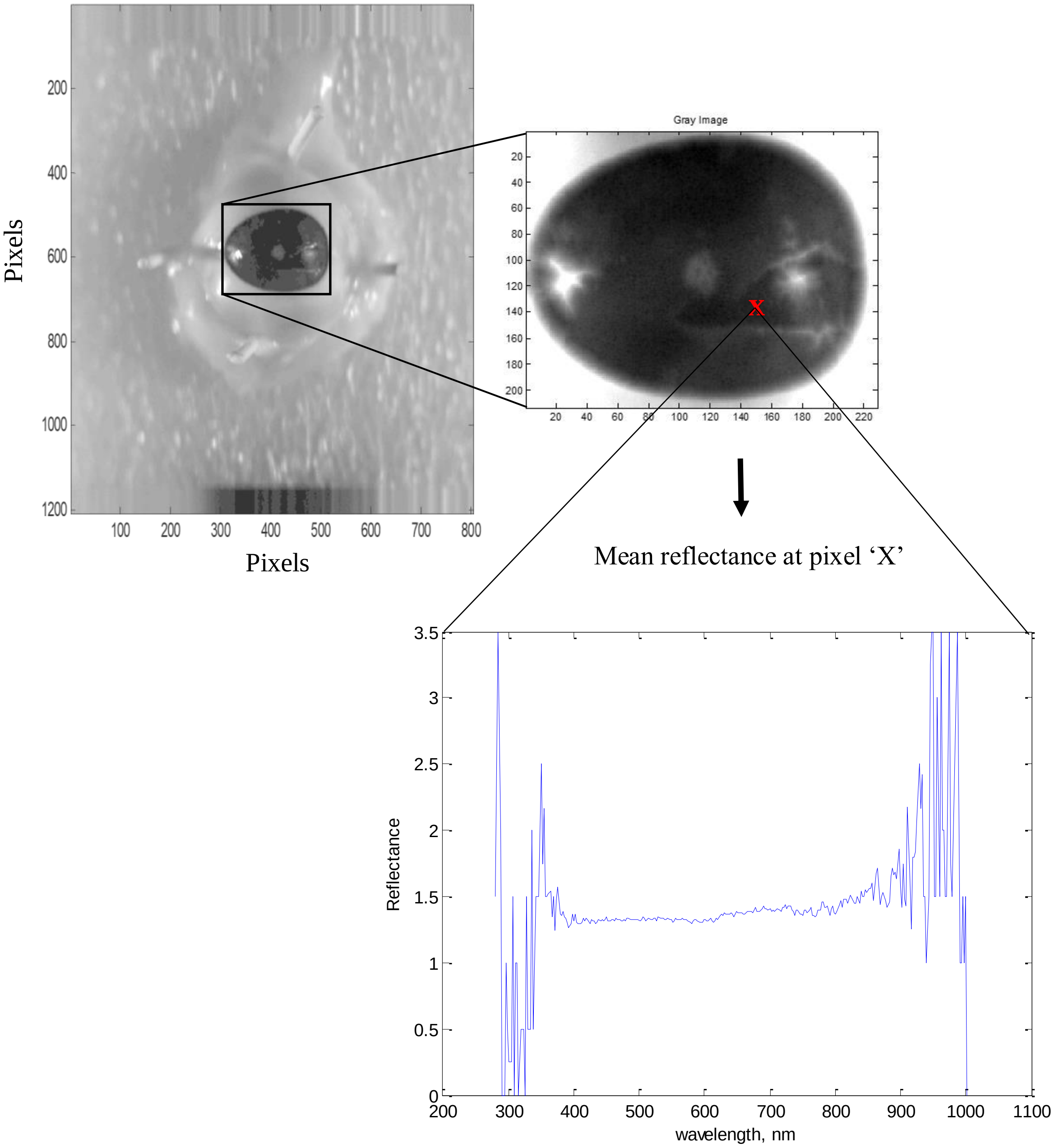

Figure 4.1: Image sliced at band-150 (638 nm). Mean reflectance of original image at pixel 'X' as labelled.

First, the dimension was minimised via spectral binning [94] to save storage space and reduce processing time. Spectral binning where two or more spectral bands are summed up to form a unique row channel that shows in Figure 4.2. It is called on-chip binning if the summation is performed during image acquisition by the hardware, otherwise if this done offline during post-processing, is then called off-chip binning. By all means, the higher the number of binned bands (rows), the higher is the spectral signal-to-noise ratio (SNR).

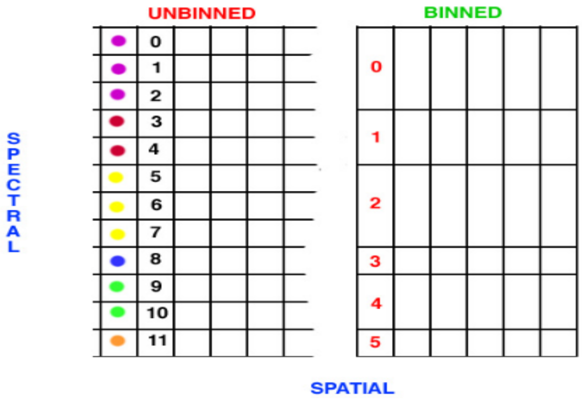

Figure 4.2:Spectral Binning. The number of across-track spatial pixels is preserved whereas the bands (0,1,2) are binned to form band (0), bands (3,4) will form band 1 and so on [94]**.**

After that, the image data were saved for the post-processing. The cubical image dimension 1200 to 1300 x 804 (spatial) x 604 (spectral) was binned on the spectral dimension. It is worthy to note that although spectral binning may affect the spectral resolution, it can also reduce spatial redundancies.

4.1.2 Image and Reflectance Normalisation

The original image contained 604 bands. Spectral binning was applied twice, from 604 bands to 302 bands, and to 151 bands shows in **Figure 4.3**.

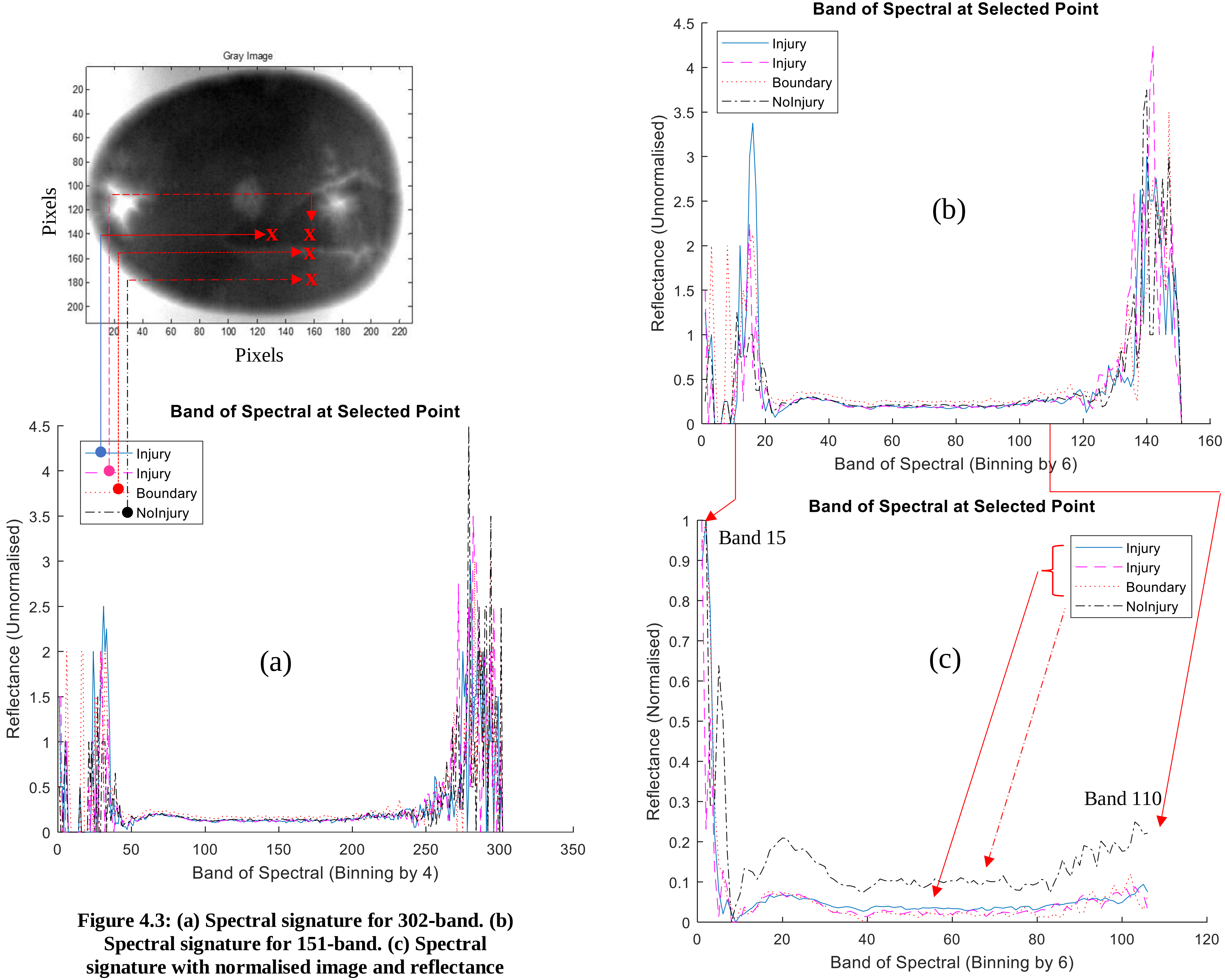

Figure 4.3: (a) Spectral signature for 302-band. (b) Spectral signature for 151-band. (c) Spectral signature with normalised image and reflectance between band-15 and band-110.

4-pixel had been selected to plot the spectral signature. 2-pixel denoted injured area, 1-pixel represented injured boundary, and the other 1-pixel referred to intact epithelium (**Figure 4.3**). **Figure 4.3 (a)** and **(b)** represent spectral signature binned by 4 and 6 respectively. Both plots do not show any significant spectral difference between injured and healthy pixels.

In contrast, **Figure 4.3 (c)** portrays the band 15 to band 110 with normalised spectral signature. The reflectance showed distinct spectral signature within the selected band, whereby non-injured area refers to healthy cornea being separated from the injuries and its boundaries. Therefore, normalisation of spectral signature and band selection are required to distinguish intact and un-intact epithelium layer.

4.1.3 Bad Band Removal

Initially, the band selection was performed via visual interpretation. For example, band 1 and 10, as shown in **Figure 4.4**, had no useful information to differentiate the target pixels, while band 140 was comprised of noisy image.

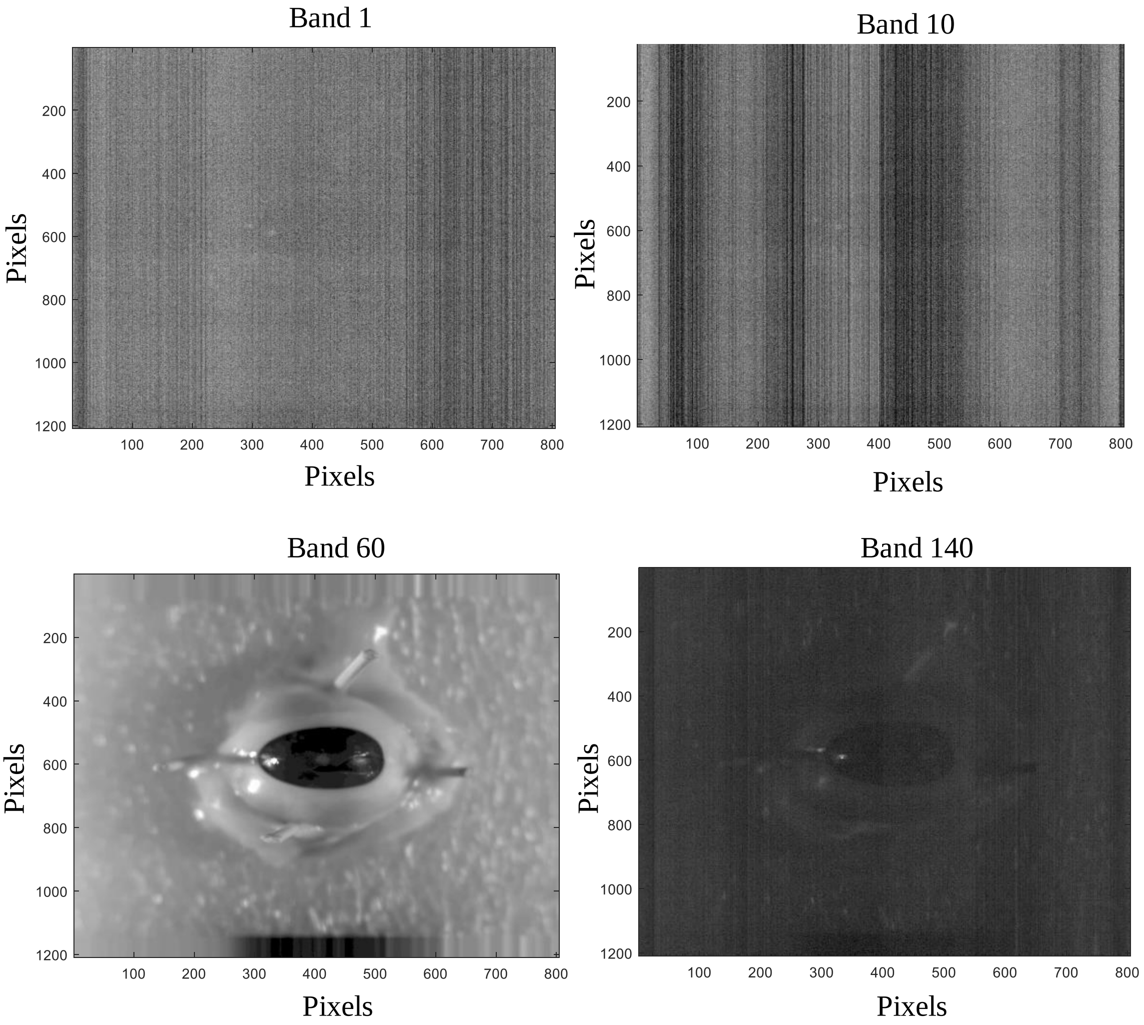

Figure 4.4: Visual interpretation on single band.

Refer to Figure 4.3 (C) based on the spectral signature, band less than 15 and more than 120 not contained useful information (bad band) and had been discarded. In comparison to band 60, the pixels of interest were successfully identified. The procedure of automatic band selection is depicted in section 4.2.

4.2 The 8-Step Image Enhancement for Corneal Epithelium Injuries

As aforementioned, eye staining step was omitted in group 1, but this procedure was carried out in group 2 and group 3 to provide ground truth images. Based on the grading staining in the Oxford schema [95] , various types of dyes are available, for instance, fluorescein sodium (corneal staining), rose Bengal, and lissamine green (conjunctival staining). These dyes can be applied to estimate surface damage on the cornea. However, the application of eye staining has several shortcomings [95], [96], for example, fluorescein sodium diffuses rapidly into the tissues that affects the quality of image. On the other hand, the drop size of rose Bengal and lissamine green is an essential factor for successful grading.

Hyperspectral image enhancement had been explored [97] in this study for the purpose of providing high accuracy in image classification. The steps involved in image pre-processing and image enhancement, as described in Chapter 3, had been performed to improvise distinction and visualisation of both normal and abnormal corneal epithelium (Figure 4.5). **Figure 4.6** illustrates eleven eyes that had been transformed by using PCA before image enhancement was carried out.

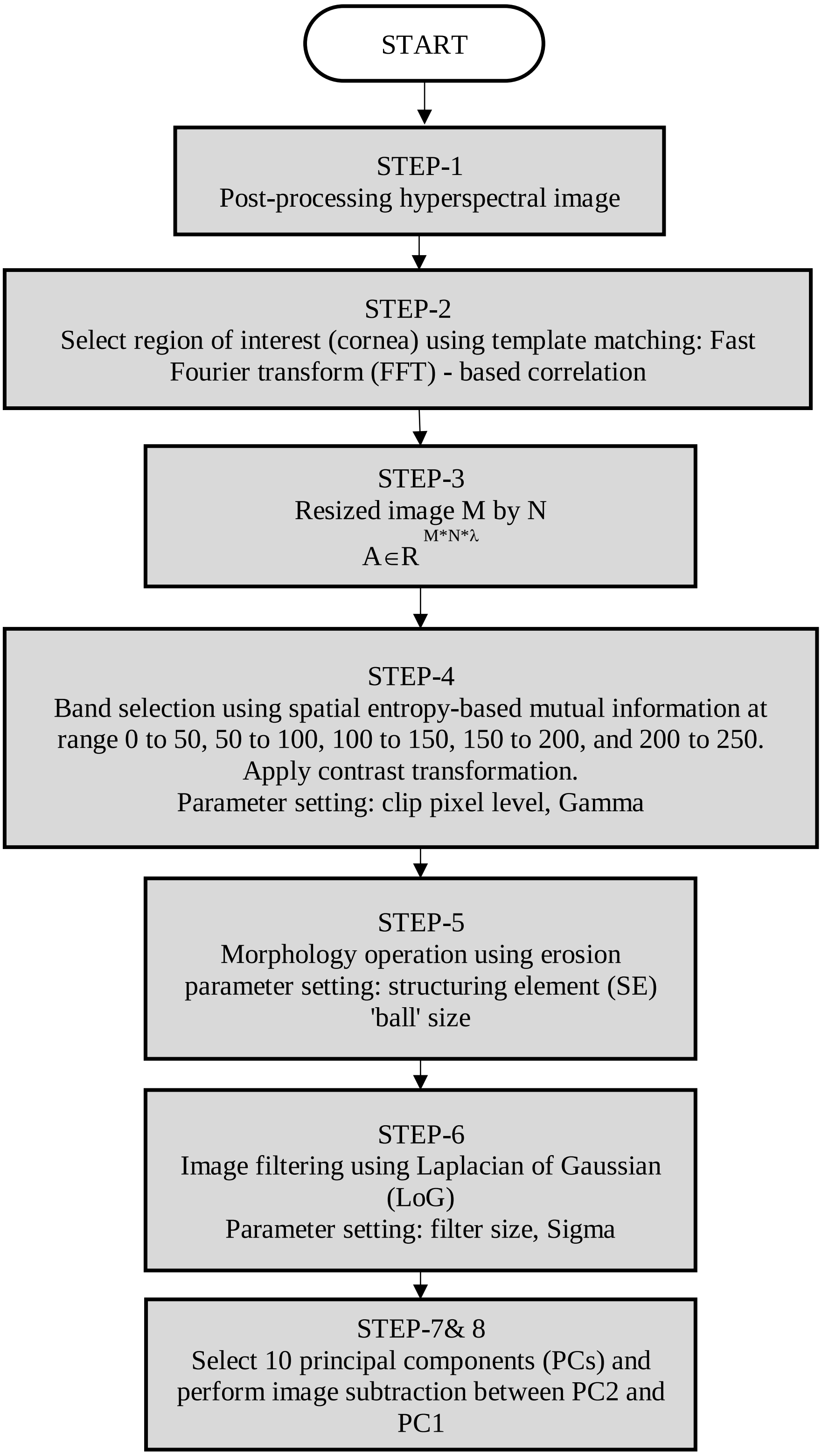

Figure 4.5: Block diagram of HSI image enhancement

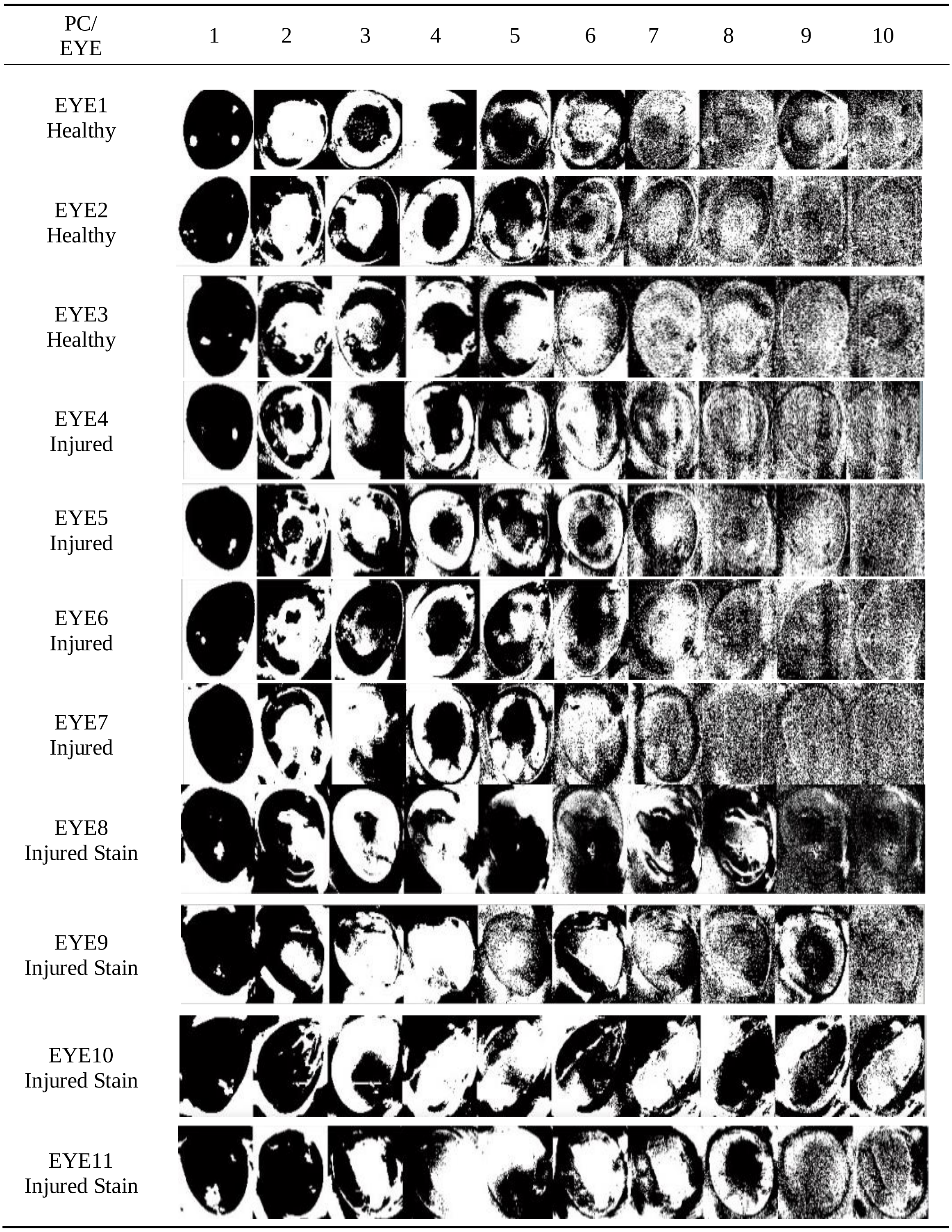

Figure 4.6: Ten principal components (PC) of eleven eyes transformed with PCA. Clinical information was noted in several PCs, particularly for EYE8 until EYE11, as these images were stained. In contrast, EYE1 to EYE7, which were not stained, appeared similar although EYE4 to EYE7 displayed abnormal corneal epithelium.

The samples showed that all the unstained eyes displayed similarity between normal and abnormal corneas. In contrast, all the stained eyes indicated vivid clinical information from the injury area.

The **8-Step** image enhancement algorithms for the hyperspectral image of porcine cornea are summarised as follows:

Step-1. Post-processing, a full band of a hyperspectral image was loaded,

$Input = M*N*\lambda$.

$$D_{M*N*\lambda} = \{d_i | i = 1, 2, \dots \dots, \lambda\} \qquad \text{Eq. 14}$$

where D represented as full band, λ denoted as band images acquired from a hyperspectral remote sensor. Each image $d_i \in D$ can be indicated as a spatial dataset where each pixel of the image has spatial attributes, i.e., the row (M) and column (N), and a non-spatial attribute, i.e., the intensity value.

Step-2. A region of interest (cornea) was selected by using the template matching method (2D FFT-based correlation [98]) (see **Figure 4.7**).

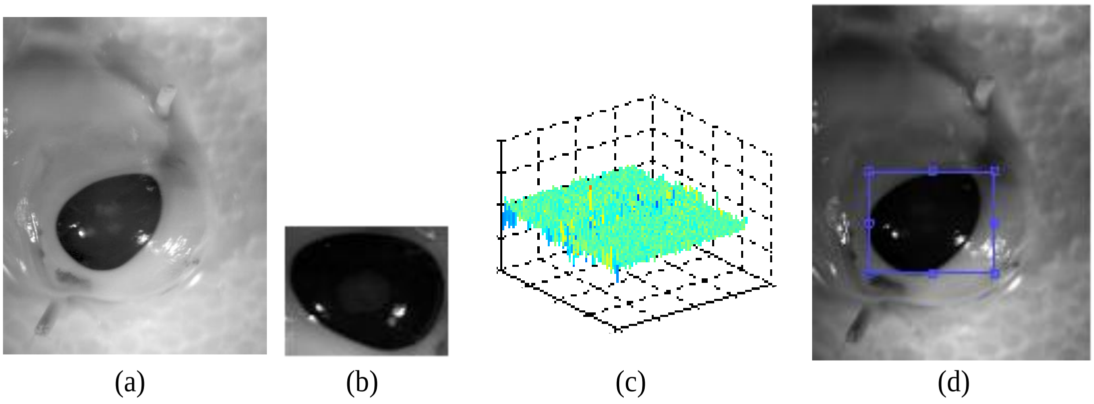
(a) (b) (c) (d)

Figure 4.7: Template matching-FFT based correlation. (a) Input image. (b) Template image. (c) Correlation plot. (d) Template matched.

$$F(u,v) = \frac{1}{MN}\sum_{m=0}^{M-1}\sum_{n=0}^{N-1} f(m,n)\exp\left[-2\pi j\left(\frac{mu}{M}+\frac{nv}{N}\right)\right] \qquad \text{Eq. 15}$$

where $F(u,v)$ denoted as image in frequency domain while, $f(m,n)$ represented as image in time domain. *M, N* designated as row and column of image pixels. The complex number is represented by exp which consists sine and cosine function. Then, the inverse image transformation (IFFT) denoted as Eq. 16.

$$f(m,n) = \sum_{u=0}^{M-1}\sum_{v=0}^{N-1} F(u,v)\exp\left[2\pi j\left(\frac{mu}{M}+\frac{nv}{N}\right)\right] \qquad \text{Eq. 16}$$

Step-3. The image was resized to 100 x 100, $A \in D^{M* N* \lambda}$.

Step-4. Contrast transformation was applied to all the selected bands (i.e., from band 50 until band 100). Parameter setting: clip pixel level, and gamma.

The bands were selected by using spatial entropy based on mutual information (SEMI) [99] derived from the spectral image that ranged as follows: 0-50, 50-100, 100-150, 150-200, and 200-250. The SEMI equation generated as follows:

$$H_s(X) = -\sum_{i=1}^{t}\frac{d_i^{int}}{d_i^{ext}}P_i\ \log_2(p_i) \qquad \text{Eq. 17}$$

where $\frac{d_i^{int}}{d_i^{ext}}$ added as a weight factor in the Shannon entropy. P_i is the fraction of the number of pixels computed from the image histogram.

$$I_s(X,Y) = H_s(X) + H_s(Y) - H_s(X,Y) \qquad \text{Eq. 18}$$

Eq. 18 is a statistical information measurement of image X, where $H_s(X)$ and $H_s(Y)$ are the entropies to the band image X and the ground truth Y, respectively, and $H_s(X,Y)$ is the joint entropy between X and Y.

$$I_s(X,Y) = -\sum_{i=1}^{t} \frac{d_i^{int}}{d_i^{ext}} P_i \log_2(p_i) - \sum_{j=1}^{0} \frac{d_j^{int}}{d_j^{ext}} P_j \log_2(p_j) + \sum_{i=1}^{t} \sum_{j=1}^{0} \frac{d_{ij}^{int}}{d_{ij}^{ext}} P_{ij} \log_2(p_{ij}) \qquad \text{Eq. 19}$$

Finally, Eq. 19 SEMI equation was generated by substitutes Eq. 17 in the Eq. 18. Which enables the spatial entropy H_s to measure the image information by evaluating the pixels non-spatial attribute in a spatial space.

As a result, the image that was within the range of wavelength 503 nm until 625 nm had been selected for further processing (see **Figure 4.8**). These images displayed significant outcomes as the injured boundary gradually disappeared from the lower to the higher band. Hence, this method can be applied to examine the healing process.

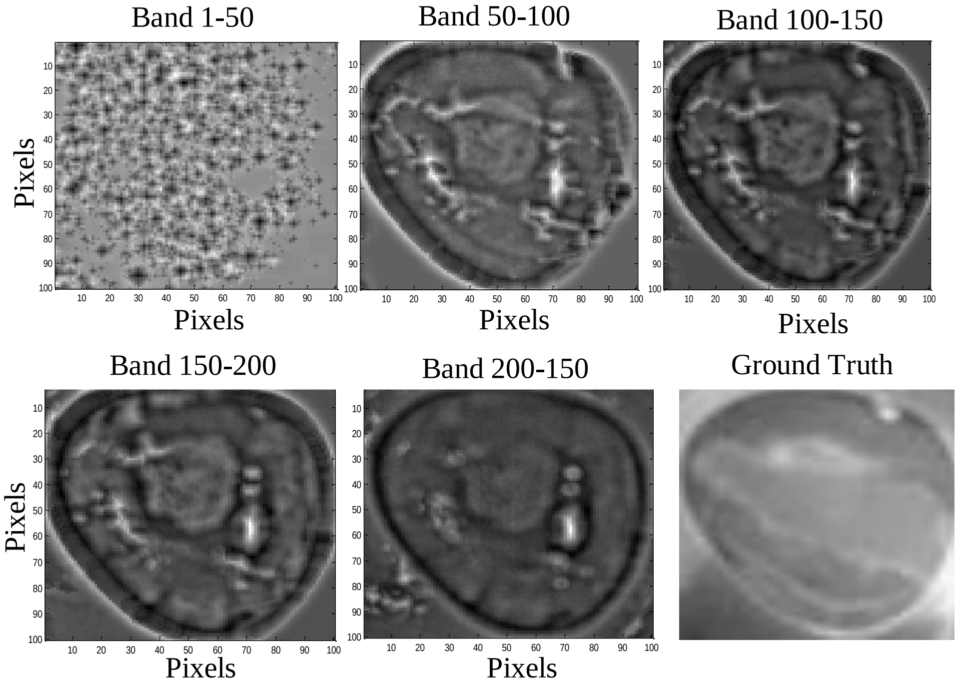

Figure 4.8: Output image at bands 1-50, 50-100, 100-150, 150-200, and 200-250. Image at row 2 column 3 is the ground truth image.

Step-5. Morphology operation using the erosion technique was applied to all the selected bands. Parameter setting: structure element (SE) ‘ball’ size.

$$A\theta B = \{z|B_z \subseteq A\} \qquad \text{Eq. 20}$$

where $A\theta B$ as erosion of A by B is the set of all points z in B, translated by z, is comprised of A. A is the gray-level image matrix, and B is the structural element matrix.

Step-6. Image filtering using Laplacian of Gaussian (LoG) had been performed on all the selected bands. Parameter setting: filter size, and sigma. The equations as follows:

$$G = \exp\left(-\frac{x^2 + y^2}{2\sigma^2}\right) \qquad \text{Eq. 21}$$

$$\nabla^2 = \left(\frac{d^2}{dx^2} + \frac{d^2}{dy^2}\right) \qquad \text{Eq. 22}$$

$$\nabla^2 G(x,y) = \left[x^2 + y^2 - \frac{2\sigma^2}{\sigma^4}\exp\left(-\frac{x^2 + y^2}{2\sigma^2}\right)\right] \qquad \text{Eq. 23}$$

The combination of a 2D Gaussian function as Eq. 21, and a Laplacian operator as Eq. 22, gives the LoG expression as Eq.23.

The three-parameter setting (SE size, filter size, and sigma) was selected based on the visualisation of the spectral image with four varying parameter sets ([5,5], [3 3], 0.1), ([15,15], [5 5], 0.1), ([25,25], [7 7], 0.1), and ([50,50], [9 9], 0.1). As a result, the image with parameters ([50,50], [9 9], 0.1) displayed the injured boundary (see **Figure 4.9**).

Step-7. Principal component analysis (as Eq. 5 to Eq. 10) of all the selected bands had been computed. As a result, 10 PCs displayed almost 100% variance, while PCs that signified zero variance were neglected.

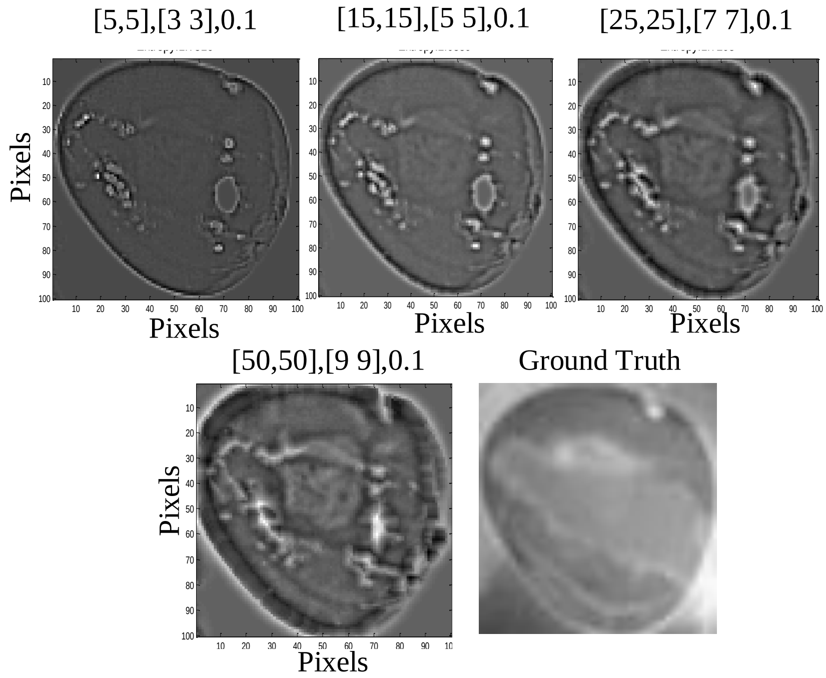

Figure 4.9: Four output image with different parameter setting ([5,5], [3 3], 0.1), ([15,15], [5 5], 0.1), ([25,25], [7 7], 0.1), and ([50,50], [9 9], 0.1). Image at row 2 column 2 is the ground truth image.

Step-8. Image subtraction was performed between PC2 (2nd largest variance) and PC1 (1st largest variance). The outcome after the enhancement was carried out is illustrated in **Figure 4.10**.

$$g(x,y) = f(x,y) - h(x,y) \qquad \text{Eq. 24}$$

where $g(x,y)$ denotes an image difference by the subtraction of two images, $f(x,y)$ from $h(x,y)$ or vice versa.

The comparison between the image before and after enhancement is portrayed in **Figure 4.11**. After enhancement, the injury boundary in the images seemed to be visible and corresponded to the ground truth image. The enhanced image appeared slightly larger due to the morphological process.

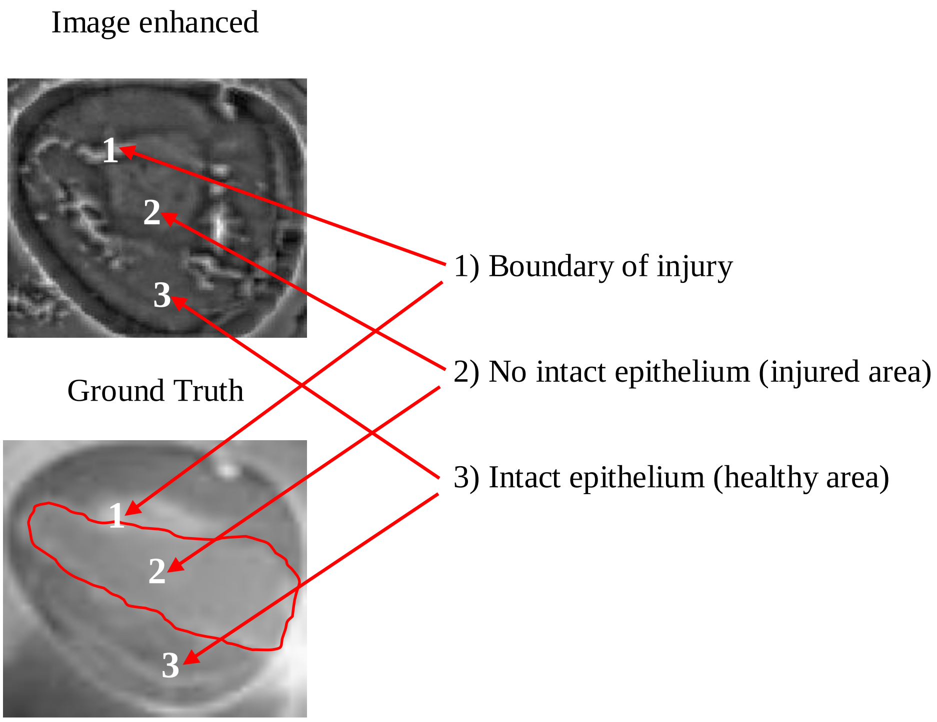

Figure 4.10: (a) Image enhanced. (b) Ground truth image.

(a)

(b)

(c)

Figure 4.11: Image comparison before and after enhancement. (a) Original image without stain. (b) After image enhancement (without stain). (c) Ground truth image with stain.

4.2.1 The 8-SHIE Applied on Indian Pines

The remote sensing Indian Pines [100] data were employed to ascertain that this newly developed algorithm worked well in the presence of hyperspectral image, although this is not reckoned as medical image. The Indian Pines data happen to be popular for hyperspectral image classification [101] as they are comprised of 16 classes of samples. The set of scenes was gathered by using an AVIRIS sensor in June 12, 1992 at the Indian Pines test site located at North-western Indiana. The set consisted of 145 x 145 pixels and 220 contiguous spectral reflectance bands in wavelengths that ranged between 0.4 µm and 2.5 µm. The set contained two-third agriculture, and one-third forest or other natural vegetation scenes. It also had two major dual-lane highways, a rail line, as well as some low-density housing, built structures, and smaller roads.

The AVIRIS refers to a proven instrument in the realm of earth remote-sensing. The primary objective of the AVIRIS project is to identify, measure, and monitor the constituents of the Earth's surface and the atmosphere based on molecular absorption, as well as particle scattering signatures. Studies that employed the AVIRIS data had predominantly focused on understanding processes associated to the global environment and climate change.

For any given material, the amount of solar radiation that is reflected (absorbed, transmitted) would appear to vary in different wavelengths. The varying features of samples allow the segregation of distinct signatures based on their response values for a given wavelength. **Figure 4.12** illustrates the spectral signatures for five classes derived from the Indian Pines dataset.

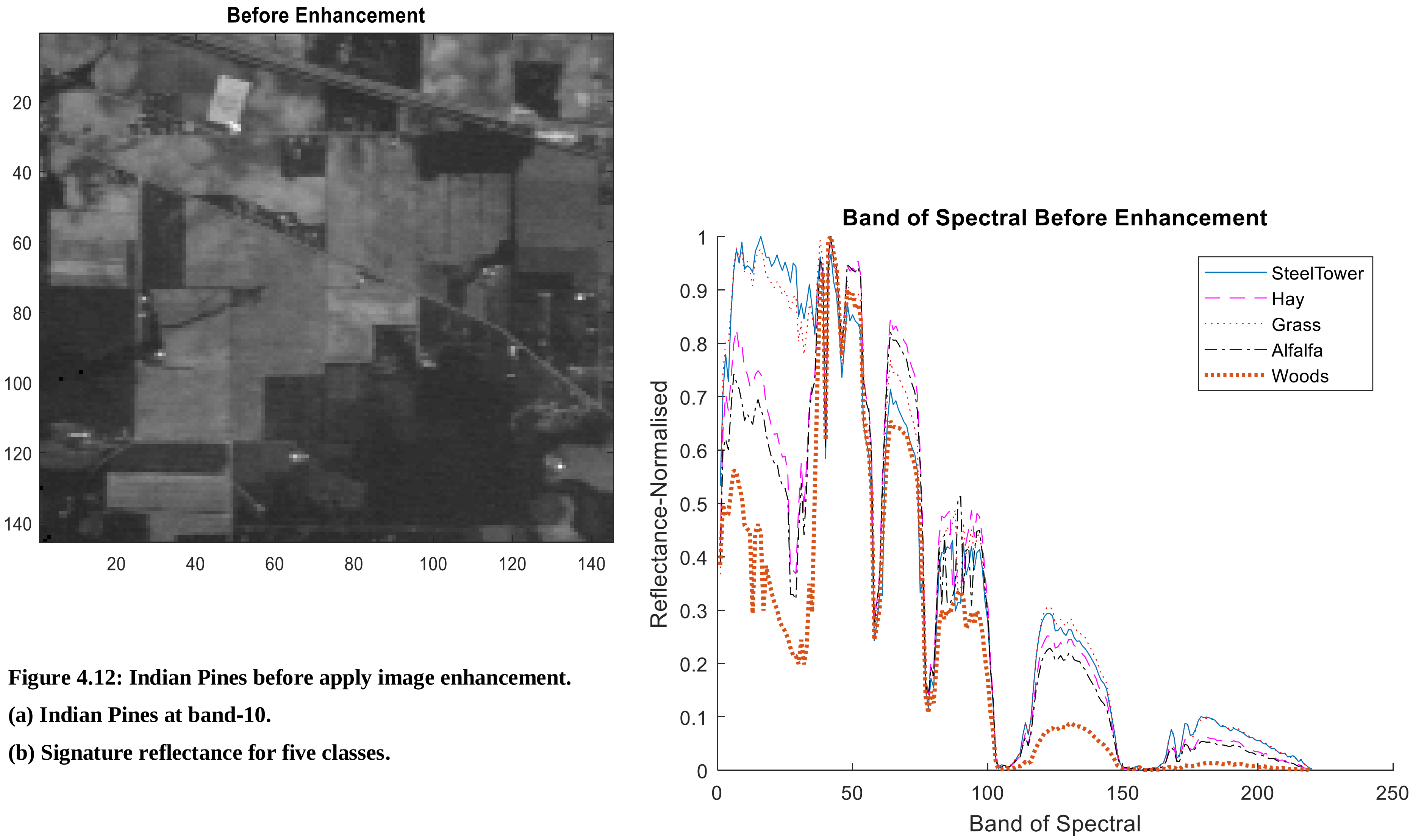

Figure 4.12: Indian Pines before apply image enhancement.

(a) Indian Pines at band-10.

(b) Signature reflectance for five classes.

The Indian Pines ground truth scene was comprised of 16 classes, which are: alfalfa, corn-notill, corn-mintill, corn, grass-pasture, grass-tress, grass-pasture-mowed, hay-windrowed, oats, soybean-notill, soybean-mintill, soybean-clean, wheat, woods, buildings-grass-trees-drives, and stone-steel-towers. However, only ten classes had been applied in order to test the algorithm. This is mainly due to the purpose of testing the algorithm in its ability to separate the spectral signatures individually towards image classification.

By comparing **Figure 4.12** (image before enhancement) with **Figure 4.13** (image after enhancement), the latter exhibited its spectral signature being distinctly separated for the five classes in the following order: woods, hay, alfalfa, grass, and steel tower.

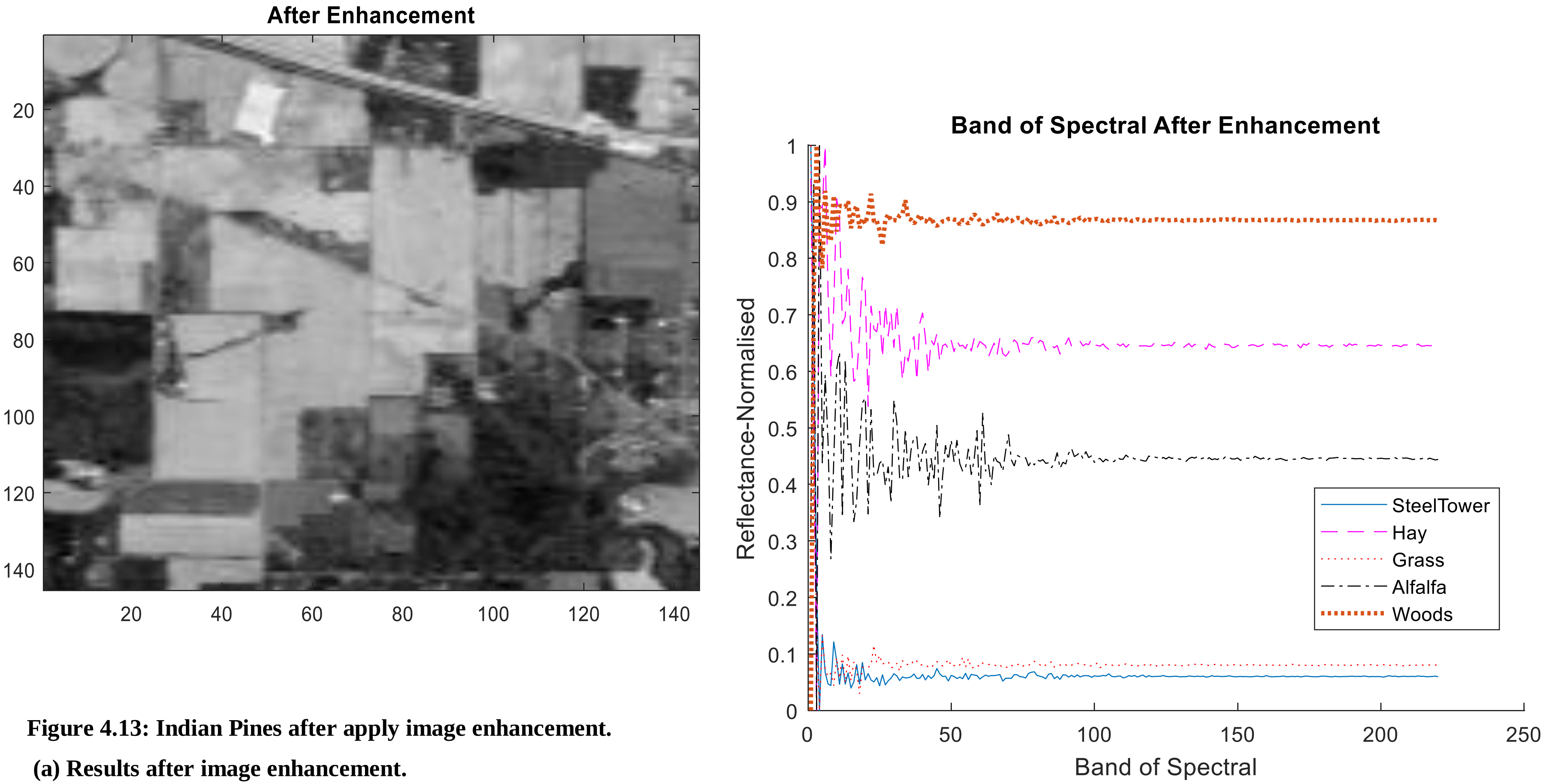

Figure 4.13: Indian Pines after apply image enhancement.

(a) Results after image enhancement.

(b) Spectral signature for five classes being separated individually. From top is woods followed by hay, alfalfa, grass, and steel tower.

With additional classes, as illustrated in **Figure 4.14**, clear separation was still noted with segregated signatures and in some cases, several classes were formed into a group. From top ranking, the four reflectance signatures are as follows: woods, buildings, wheat, and corn, which had been likely to form a group of varied wavelengths.

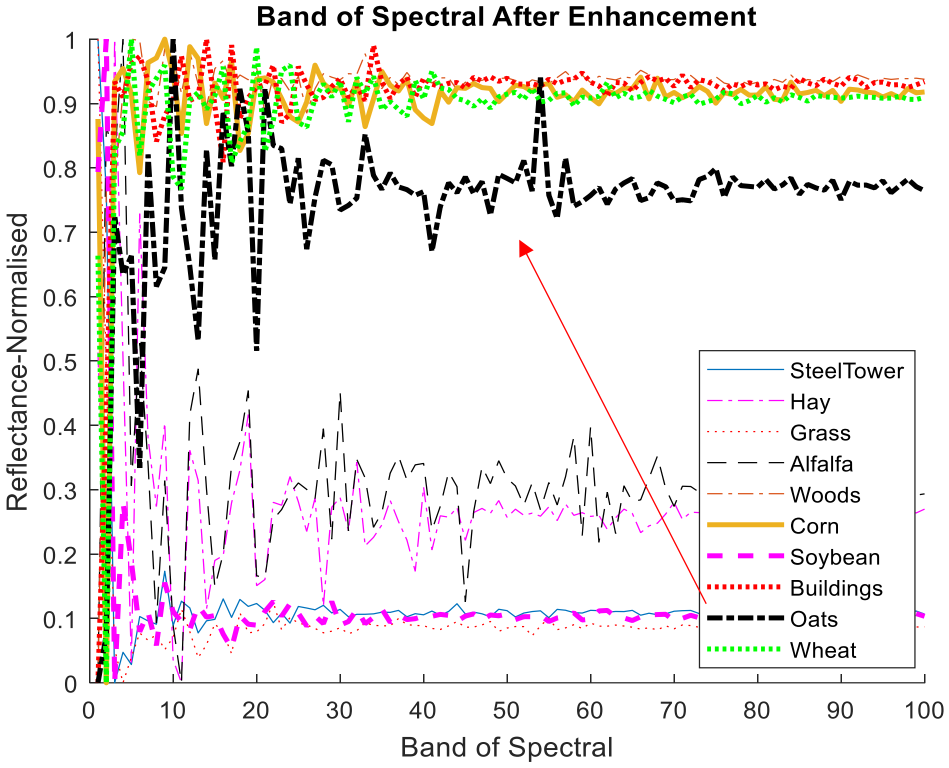

Figure 4.14: Spectral signature of Indian Pines data for ten classes after image enhancement. From top are woods, buildings, wheat, and corn in a group. Next is oats followed by alfalfa and hay in a group. Final signatures in a group are steel tower, soybean, and grass.

Followed by oats as standalone reflectance signature and being parallel with the outcomes of classification accuracies, as presented in **Table 4.1**, oats recorded 100% accuracy for eight types of classifiers. Hence, it had been envisaged that oats contained unique wavelength, in comparison to other classes. Next, two classes that formed a group were alfalfa and hay. Last but not least, steel tower, soybean, and grass were classified in the last group.

Table 4.1: Classification accuracies (%) of the Indian Pines image obtained by eight classifiers. Table source [97].

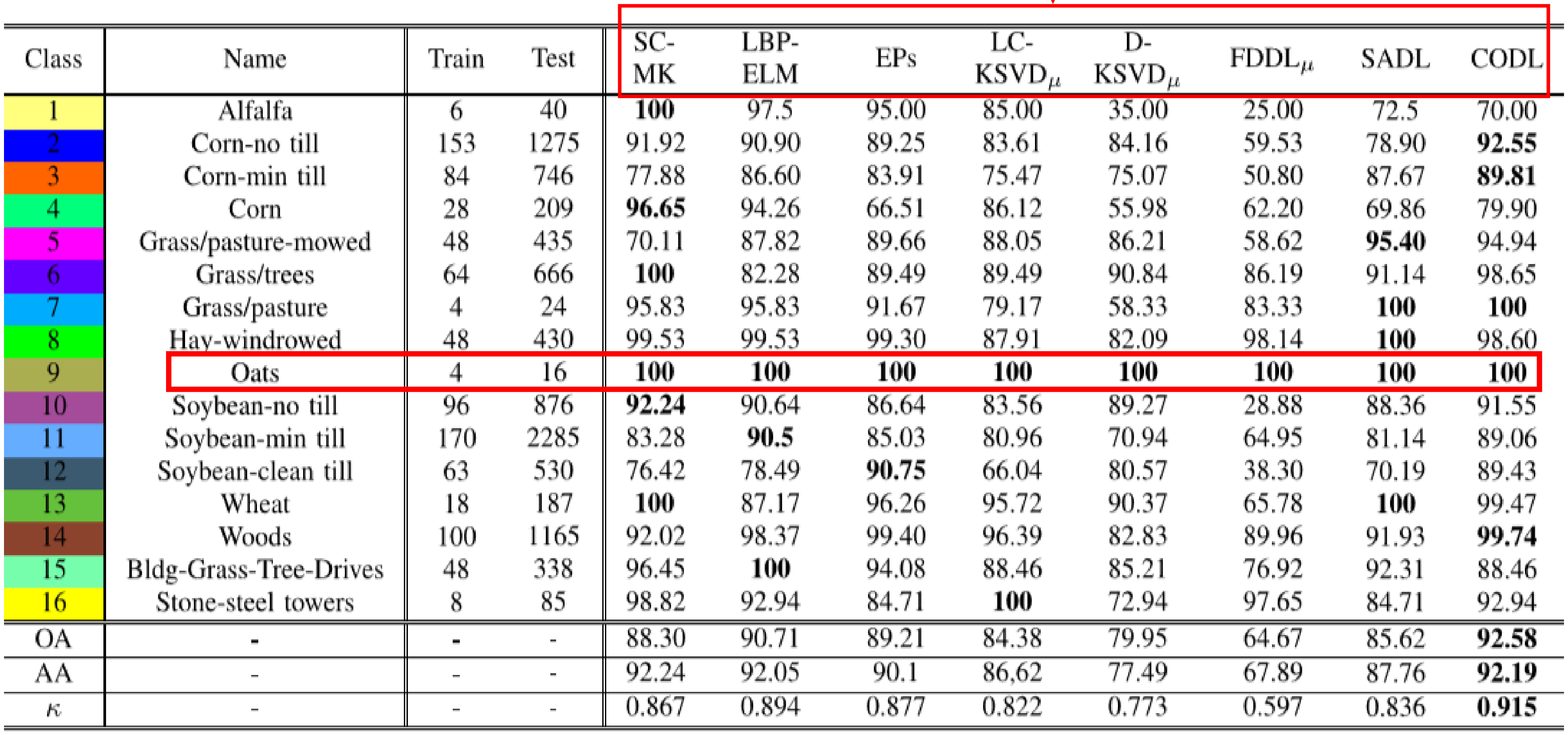

Class	Name	Train	Test	SC-MK	LBP-ELM	EPs	LC-KSVD$_\mu$	D-KSVD$_\mu$	FDDL$_\mu$	SADL	CODL
1	Alfalfa	6	40	**100**	97.5	95.00	85.00	35.00	25.00	72.5	70.00
2	Corn-no till	153	1275	91.92	90.90	89.25	83.61	84.16	59.53	78.90	**92.55**
3	Corn-min till	84	746	77.88	86.60	83.91	75.47	75.07	50.80	87.67	**89.81**
4	Corn	28	209	**96.65**	94.26	66.51	86.12	55.98	62.20	69.86	79.90
5	Grass/pasture-mowed	48	435	70.11	87.82	89.66	88.05	86.21	58.62	**95.40**	94.94
6	Grass/trees	64	666	**100**	82.28	89.49	89.49	90.84	86.19	91.14	98.65
7	Grass/pasture	4	24	95.83	95.83	91.67	79.17	58.33	83.33	**100**	**100**
8	Hay-windrowed	48	430	99.53	99.53	99.30	87.91	82.09	98.14	**100**	98.60
9	Oats	4	16	**100**	**100**	**100**	**100**	**100**	**100**	**100**	**100**
10	Soybean-no till	96	876	**92.24**	90.64	86.64	83.56	89.27	28.88	88.36	91.55
11	Soybean-min till	170	2285	83.28	**90.5**	85.03	80.96	70.94	64.95	81.14	89.06
12	Soybean-clean till	63	530	76.42	78.49	**90.75**	66.04	80.57	38.30	70.19	89.43
13	Wheat	18	187	**100**	87.17	96.26	95.72	90.37	65.78	**100**	99.47
14	Woods	100	1165	92.02	98.37	99.40	96.39	82.83	89.96	91.93	**99.74**
15	Bldg-Grass-Tree-Drives	48	338	96.45	**100**	94.08	88.46	85.21	76.92	92.31	88.46
16	Stone-steel towers	8	85	98.82	92.94	84.71	**100**	72.94	97.65	84.71	92.94
OA	-	-	-	88.30	90.71	89.21	84.38	79.95	64.67	85.62	**92.58**
AA	-	-	-	92.24	92.05	90.1	86,62	77.49	67.89	87.76	**92.19**
κ	-	-	-	0.867	0.894	0.877	0.822	0.773	0.597	0.836	**0.915**

4.3 Performance Measure using Contrast to Noise Ratio (CNR)

Figure 4.15 and **Figure 4.16** illustrate the outcomes of images with contrast to noise ratio (CNR) [74], as well as the histogram between healthy and injured corneas. CNR measure (**Eq.25**) used to determine image quality. The CNR value for the enhanced image appeared to be higher, when compared to the original image, hence making the injury easily detectable (Figure 4.16 (C)) with human vision. Whereas, lower CNR indicated difficulty in detecting the injury.

$$CNR = \frac{Contrast}{Noise} = \left[\frac{|\mu_1 - \mu_2|}{\sqrt{\sigma_1^2 + \sigma_2^2}}\right] \qquad \text{Eq. 25}$$

Where μ and σ are expectation values and standard deviations of two different images or it can be two areas of different brightness in a same image.

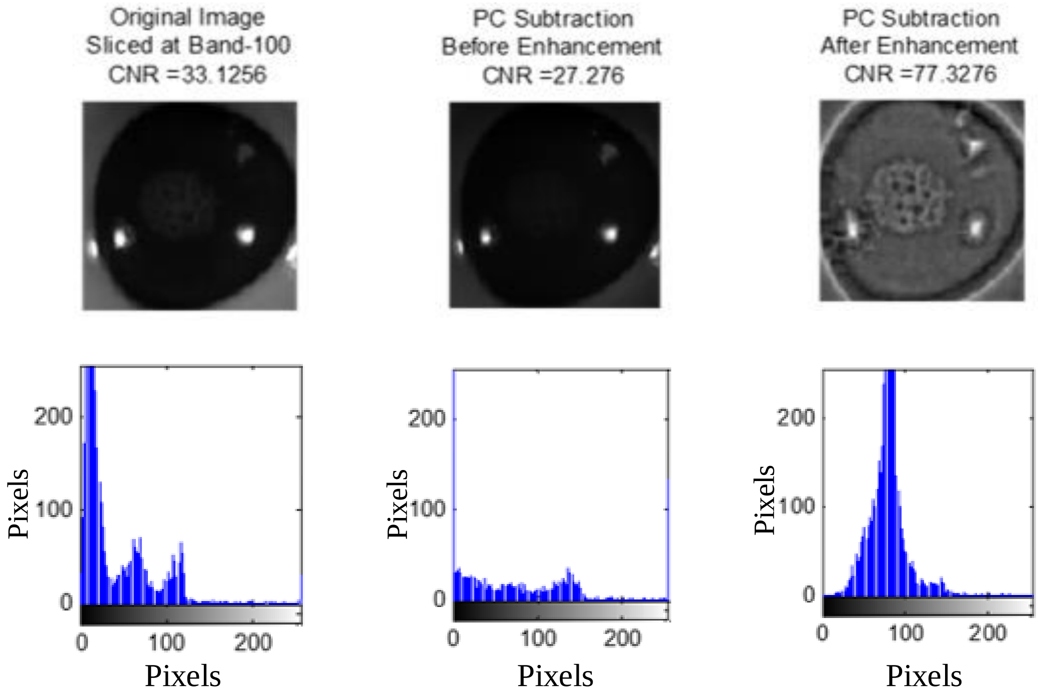

(a)

(b)

(c)

Figure 4.15: Images of healthy cornea with the histogram underneath respectively. Images were normalised and resized to 100 x 100. (a) Original image sliced at band-100 (CNR: 33.1256), (b) Image after PC subtraction before enhancement (CNR: 27.276), and (c) Image after PC subtraction and enhancement (CNR: 77.3276).

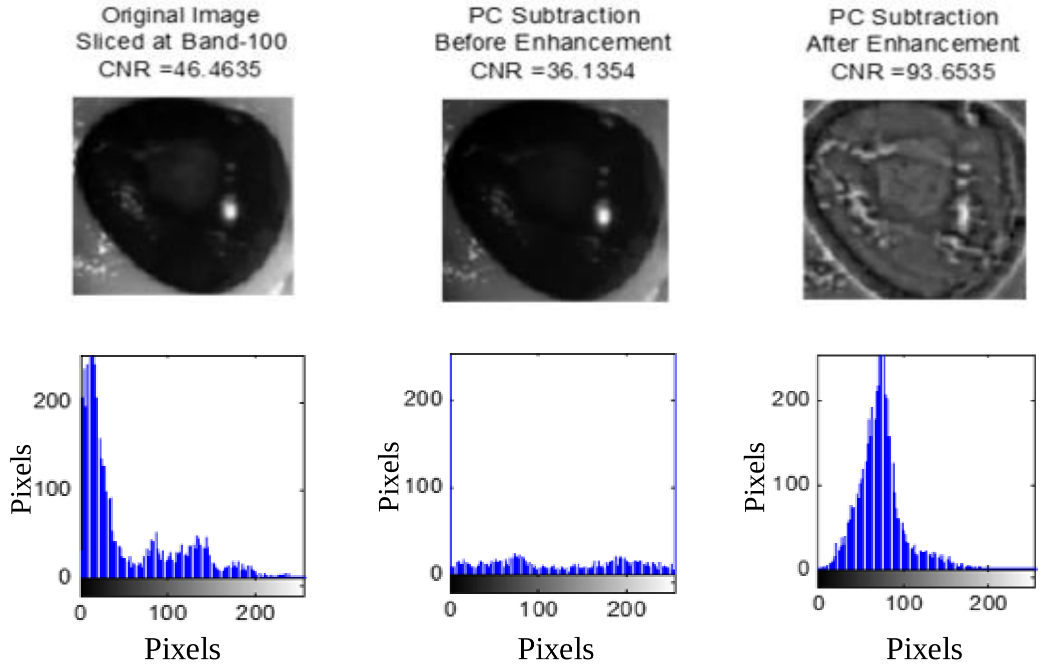

(a) (b) (c)

Figure 4.16: Images of injured cornea with the histogram underneath respectively. Images were normalised and resized to 100 x 100. (a) Original image sliced at band-100 (CNR: 46.4635), (b) Image after PC subtraction before enhancement (CNR: 36.1354), and (c) Image after PC subtraction and enhancement (CNR: 93.6535).

Finally, image enhancement was performed upon all twenty-five eyes, as portrayed in **Figure 4.17**. All these images were further used in the next process for image classification.

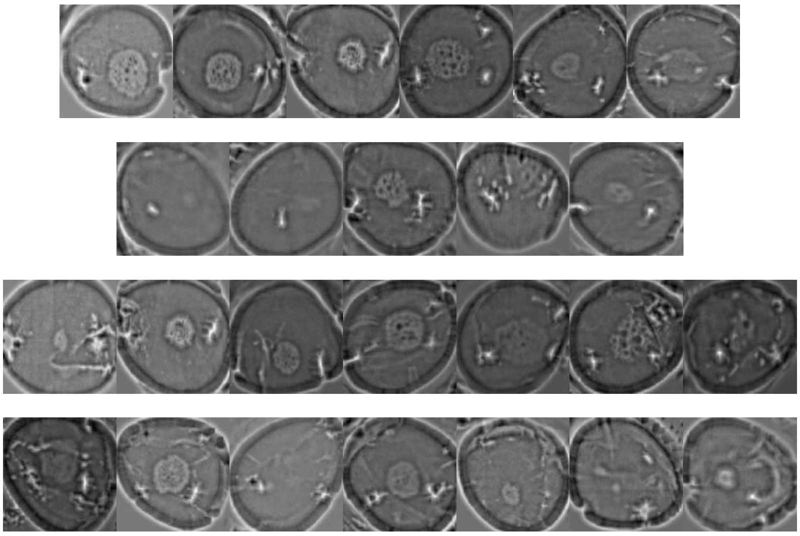

Figure 4.17: All the images were normalised and resized to 100 x 100. Rows 1 and 2 represent healthy eyes, while rows 3 and 4 denote injured eyes.

4.4 Summary

The preliminary study from experiment group 1 had shown that the reflectance signatures retrieved from hyperspectral imaging of both normal and abnormal corneal epithelium tissues of porcine had similar morphology with subtle variances. This gives confidence to pursue further experimental in groups 2, 3, and 4 on the data collected for further image analyses.

Twenty-five hyperspectral data were employed to develop a new image enhancement algorithm. Initially, the spatial and the spectral dimensions were interpreted visually from band-to-band. The spatial and spectral normalisation had been applied in advance during the pre-processing step to attain optimum outcomes. Furthermore, any unnecessary band that contained meaningless information had been discarded to save space storage and to hinder data redundancy. After that, the 8-Step image enhancement was carried out to discriminate injured and healthy corneas.

Overall, the results showed that the proposed algorithm had been able to illustrate clearly the injured boundary. The algorithm could also be used to monitor the cornea healing process as the injured boundary can be viewed from band-to-band. Primarily, this algorithm had been designed for the cornea images gathered for the purpose of this thesis. Besides, in order to ascertain that this algorithm worked well for other hyperspectral images, it was further tested on the existing remote-sensing Indian Pines dataset. As such, some parameters were altered to suit the image properties. For example, the SE size in the morphology operation was changed to 1 instead of 50. From the reflectance signature results, this algorithm successfully segregated the ten varying classes, although its main purpose is to distinguish between two classes. All the enhanced images were then applied for image classification in the next chapter.

CHAPTER 5

MIXTURE DEEP-LEARNING CLASSIFICATION OF CORNEAL EPITHELIUM INJURIES

The purpose of this chapter is to describe and compare the three classification approaches (**Figure 5.1**) with the purpose of figuring out the best accuracy and low time consumption for the cornea assessment. The three classification approaches are as follows:

1. Histogram feature extraction with SVM-GRBF classifier.
2. Transfer learning using pretrained AlexNet with a fine-tuned model.
3. Feature extraction with pretrained AlexNet (Mixture AlexNet and SVM-Linear).

In regard to this matter, it is important to note that the classification input features can be extracted from the histogram (features crafting) as well as the deep learning neural network (features learning). Image classification is described as the process of labelling predetermined pixels into different classes. Commonly, the purpose of classification in medical application is to classify healthy and unhealthy tissues for the purpose of analysing and diagnosing specific diseases such as cancer [102].

In relation to this, an automatic classification has been developed using various techniques with the purpose of helping human to classify them in an objective manner. Moreover, several procedures have been adopted in the achievement of image classification, namely image pre-processing, features selection, features extraction, type of classifiers, and performing accuracy assessment [103].

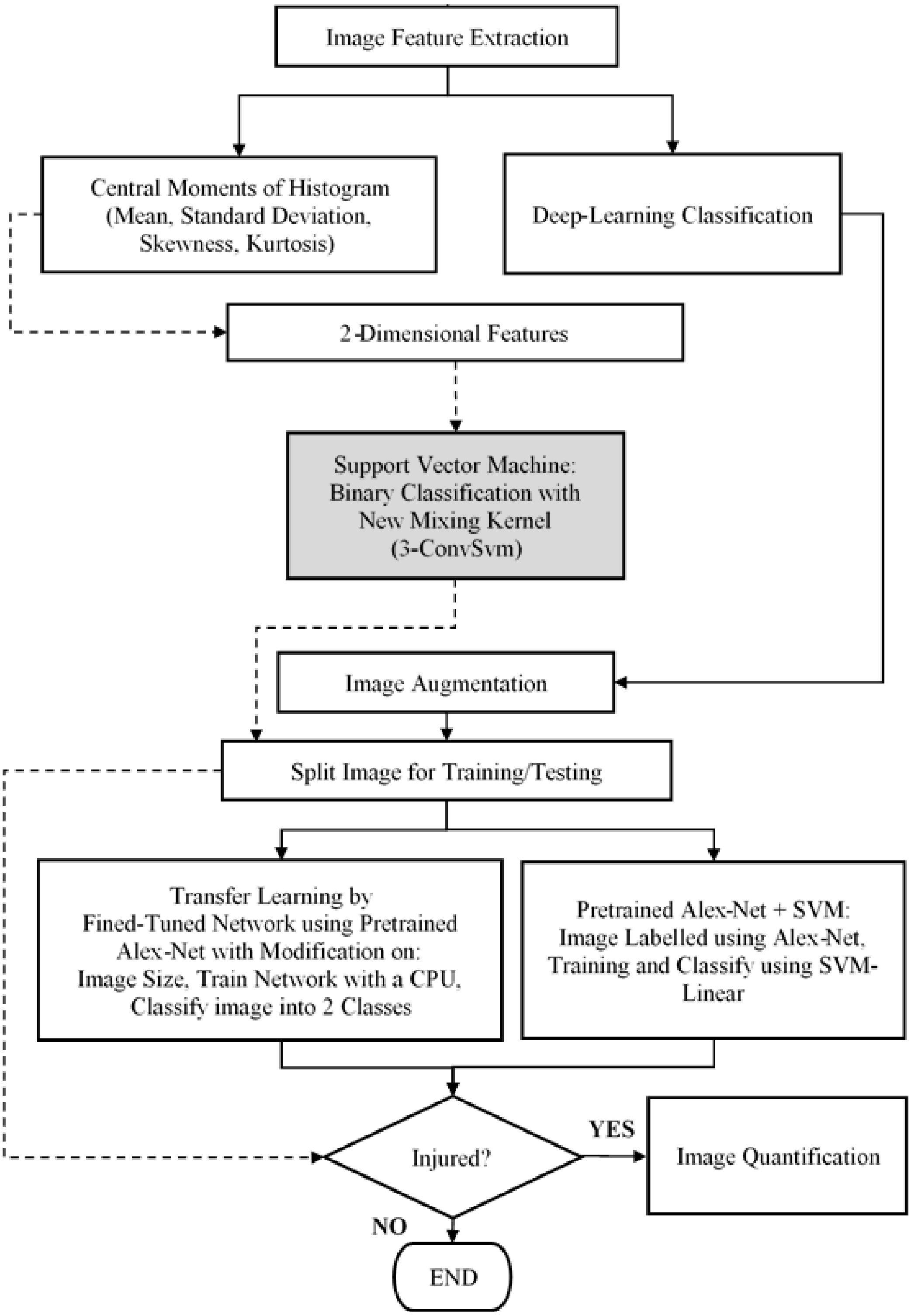

Figure 5.1: Framework of three classification approaches.

The purpose of image pre-processing is to process the original image and prevent any ineffective information. On another note, the objective of both feature selection and extraction is to avoid the overfitting of the data to ensure that further analysis can be performed. The function of feature extraction is to transform high-dimensional datasets into a lower dimensional space. Contrastingly, feature selection is not responsible in transforming or altering the original representation of the data. The next procedure refers to the type of classifiers which can be further categorised as follows: (1) supervised learning allows the input variables and output variables to be utilized for the purpose of learning the mapping function, and (2) unsupervised learning only provides input data and no corresponding output variables.

Hence, it is crucial to understand that the goal of unsupervised learning is to model the underlying structure in order to learn more about the data. The final procedure involves the performance assessment which is carried out based on the six criteria proposed by Cihlar et al. (1998) for the purpose of evaluating the classification method [104]. The six criteria are accuracy, reproducibility, robustness, ability to fully use the information content of the data, uniform applicability, and objectiveness. Nevertheless, in reality, no classification algorithm can satisfy all these requirements nor be applied to all studies due to different environmental settings and data used.

5.1 Building a Deep Learning Convolutional Neural Networks

25 images have been obtained from the PC subtraction consisting of the normal and the abnormal cornea. image flipping and rotation were employed for data augmentation to increase the classification accuracy and to enrich the training data [83]. In total, 94 images have been used following the image augmentation for classification. All images have been transformed into image vectors and randomly split into two sets for training and testing. The ratio of training to testing was varied across the following values: 0.1(10% for training, 90% for testing), 0.2, 0.3, 0.4, 0.5, 0.6, 0.7, 0.8, 0.9, and 1.0 in order to determine the optimal accuracy. The time consumed using a single CPU for every distribution has also been recorded.

The parameters identification is considered as a challenging task because there are many parameters that need to be adjusted. In this research we adopted a structure made by Alex Krizhevsky (AlexNet), the champion of ImageNet Large Scale Visual Recognition Challenge (ILSVRC2010) as a reference [85]. In this case, five convolutional layers and three max pooling were used to achieve the optimum result. Max pooling is described as technique that down sampling the array size for the purpose of reducing the dimensions of an image by taking the maximum pixel value of a grid. Moreover, this also helps to reduce overfitting and allow the model to be more generic. The idea here is that the most interesting bit will be kept if something interesting is found in any of the four input tiles that makes up each 2 by 2 grid square. Hence, this allows the size of array to be reduced and at the same time, keeping the most important bits.

The next step involves the addition of three fully connected layers with the inclusion of a softmax layer at the very end of the fully connected layers. This process reduces a giant image into a fairly small array. It is crucial to note that an array is just a bunch of numbers that can be used as input into another neural network. Hence, the final neural network will decide if the image is a match or not a match. Apart from that, a fully connected network is applied to differentiate it from the convolution step.

On a more important note, these steps can be combined and stacked as many times as needed, be it two, three, or even ten convolution layers when solving problems in the real world. The max pooling can be thrown wherever appropriate in order to reduce the size of data. The basic idea is to start with a large image which is boiled down step by step until a single result is achieved. In this case, more convolution steps allow the network to learn to recognise more complicated features. For example, the first convolution step might involve the process of recognising injury edges, while the second might be responsible of identifying the shape of injury using the knowledge of injury edges. Next, the third step may include the technique of situating the location of injury using the knowledge on injury shape.

The experiment in this study started with a 227 x 227-pixel image, with the application of convolution and max pooling twice. The process was followed by the application of convolution three more times and the max pooling in order to produce three fully-connected layers. The end result shows that the image managed to be classified into healthy and injured classes. Nevertheless, it is crucial to note that a large amount of data makes it harder for neural network to solve the problem, but it can be compensated by making the network bigger for the purpose of allowing more complicated patterns to be learned. Therefore, it can be understood that the deep neural network needs to build up more layers compared to the traditional neural network.

5.2 Histogram Feature Extraction with SVM-GRBF Classifier

In this case, the first classification approach was performed based on the histogram of the gray-scale image. Specifically, a total of four features were extracted, namely mean, standard deviation (square root of the variance), skewness, and kurtosis which were calculated using the probability distribution of the intensity levels in the histogram bins [105]. The histogram of intensity levels is described as a simple summary of the statistical information of the image, which involves the use of individual pixels to calculate the gray-level histogram. Therefore, it can be clearly understood that the histogram contains the first-order statistical (central moments) information about the image values [106]. The statistics are defined based on the following equations_[107].

Let random variable I represents the gray-levels of image values. The first-order histogram P(I) is defined as:

$$P(I) = \frac{No. of pixels\ with\ gray\ level\ I}{Total\ No. of\ pixels\ in\ the\ histogram} \qquad \text{Eq. 26}$$

Based on the definition of P(I), the mean and central moments μ_k of I given by:

Mean:

$$Pm1 = \sum_{I=0}^{N-1} I^1 P(I) \qquad \text{Eq. 27}$$

Central moments:

$$\mu_k = \sum_{I=0}^{N-1} (I - m1)^k P(I) \qquad \text{Eq. 28}$$

where k = 2, 3, 4, and N is the number of possible gray levels.

The most frequently used central moments are variance, skewness, and kurtosis given by μ_2, μ_3, and μ_4 respectively [107]. The function of variance is to measure the deviation of gray-levels from the mean. Meanwhile, skewness is described as an indicator of asymmetry around the mean, whereas kurtosis is defined as a function of the histogram sharpness. Apart from that, the combinations of 2D-features were computed for both healthy and injured eyes, which will then be used as inputs to the binary classifiers.

The results of 1st-order histogram are shown in **Table 5.1**. All of these features will then be combined as 2D-features for the classification purposes using SVM with various parameters setting. In addition, the results of six pairs 2D-features (Mean-Std, Mean-Skew, Mean-Kurt, Std-Skew, Std-Kurt, Skew-Kurt) are depicted in (Section 5.5).

Table 5.1: 4-features computed from image histogram for 25 eyes.

EYE Healthy	Mean Healthy	Standard Deviation Healthy	Skewness Healthy	Kurtosis Healthy	EYE Injured	Mean Injured	Standard Deviation Injured	Skewness Injured	Kurtosis Injured
1	135.31	28.10	0.69	4.79	12	125.85	26.46	0.51	5.36
2	97.23	28.67	0.92	5.86	13	110.69	26.74	0.83	6.45
3	101.50	27.87	0.84	6.09	14	81.23	22.58	1.43	8.40
4	80.91	22.34	1.22	8.73	15	82.07	23.08	0.83	5.81
5	88.11	25.90	0.95	7.26	16	76.56	19.28	1.16	8.80
6	102.41	26.99	1.04	6.47	17	79.44	28.30	1.02	5.54
7	100.73	19.88	1.10	7.74	18	67.84	20.04	1.11	8.01
8	108.48	21.03	1.25	9.66	19	73.76	27.27	1.11	6.24
9	89.85	24.00	1.26	8.21	20	116.46	27.40	0.61	4.64
10	99.75	27.72	0.89	6.08	21	120.36	21.74	0.76	6.61
11	98.96	22.73	1.18	8.66	22	96.72	27.15	0.94	6.51
					23	108.97	28.55	0.67	5.71
					24	101.93	29.25	0.27	4.67
					25	105.74	24.04	0.37	4.67

5.3 Transfer Learning Using Pretrained AlexNet with a Fine-Tuned Model

The second approach classification adopted by the present study refers to transfer learning with a fine-tuned model, whereby the last three layers were configured for a total of 1000 classes of the original trained network. In this work, these layers including several other layers were fine-tuned (see **Table 5.2**, underlined-bold items) for the new classification cornea problem that was restricted to only two classes.

In this research, image augmentation with flipping and rotation were applied in order to obtain more images. However, the image augmentation is only applied to the injured image as shown in **Figure 5.2**. More importantly, image augmentation allows a variety of injured locations and positions to be obtained, which is not applicable on healthy cornea (**Figure 5.3**). As a result, a total of 94 images managed to be achieved instead of the initial target of 25 images.

Table 5.2: AlexNet parameters with fine-tuned network for transfer learning on cornea images.

No	Layer	Type	Parameters
1	Data	Image Input	Layer1: Convolution layer **Input image size: 227×227×3** with zero centre normalisation No. of filters: 96 Filter size: 11×11×3 Stride: [4 4] Output: 224/4×224/4×96 (because of stride 4) **Train Network with a CPU**
2	Conv1	Convolution	
3	Relu1	Relu	Rectified linear units
4	Norm1	Cross channel normalisation	Cross channel normalisation with 5 channels per element
5	Pool1	Max pooling	Layer2: Max pooling followed by convolution Input: 55×55×96 Max pooling: 55/2×55/2×96 = 27×27×96 No. of filters: 256 Filter size: 5×5×48 Stride: [2 2] Output: 27×27×256 **Train Network with a CPU**
6	Conv2	Convolution	
7	Relu2	Relu	Rectified linear units
8	Norm2	Cross channel normalisation	Cross channel normalisation with 5 channels per element
9	Pool2	Max pooling	Layer3: Max pooling followed by convolution Input: 27×27×256 Max pooling: 27/2×27/2×256 = 13×13×256 No. of filters: 384 Filter size: 3×3×256 Stride: [2 2] Output: 13×13×384 **Train Network with a CPU**
10	Conv3	Convolution	
11	Relu3	Relu	Rectified linear units
12	Conv4	Convolution	Layer4: Convolution layer Input: 13×13×192 No. of filters: 384 Filter size: 3×3×192 Stride: [1 1] Output: 13×13×384 **Train Network with a CPU**
13	Relu4	Relu	Rectified linear units
14	Conv5	Convolution	Layer5: Convolution layer Input: 13×13×192 No. of filters: 256 Filter size: 3×3×192 Stride: [1 1] Output: 13×13×256 **Train Network with a CPU**
15	Relu5	Relu	Rectified linear units
16	Pool3	Max pooling	3×3 max pooling with stride [2 2]
17	Fc6	Fully connected	Layer6: Fully connected layer Input: 13×13×128 is transformed into a vector Output: 4096-dimensional feature with 2048 in each vector
18	Relu6	Relu	Rectified linear units
19	Drop6	Dropout	Reducing overfitting with probability 0.5
20	Fc7	Fully connected	Layer7: Fully connected layer 4096-dimensional feature with 2048 in each vector
21	Relu7	Relu	Rectified linear units
22	Drop7	Dropout	Reducing overfitting with probability 0.5
23	Fc8	Fully connected	Layer8: Fully connected layer **2 number of classes**
24	Prob	SoftMax	Reducing overfitting
25	Output	Classification output	**Classify 2 image: Healthy and Injured**

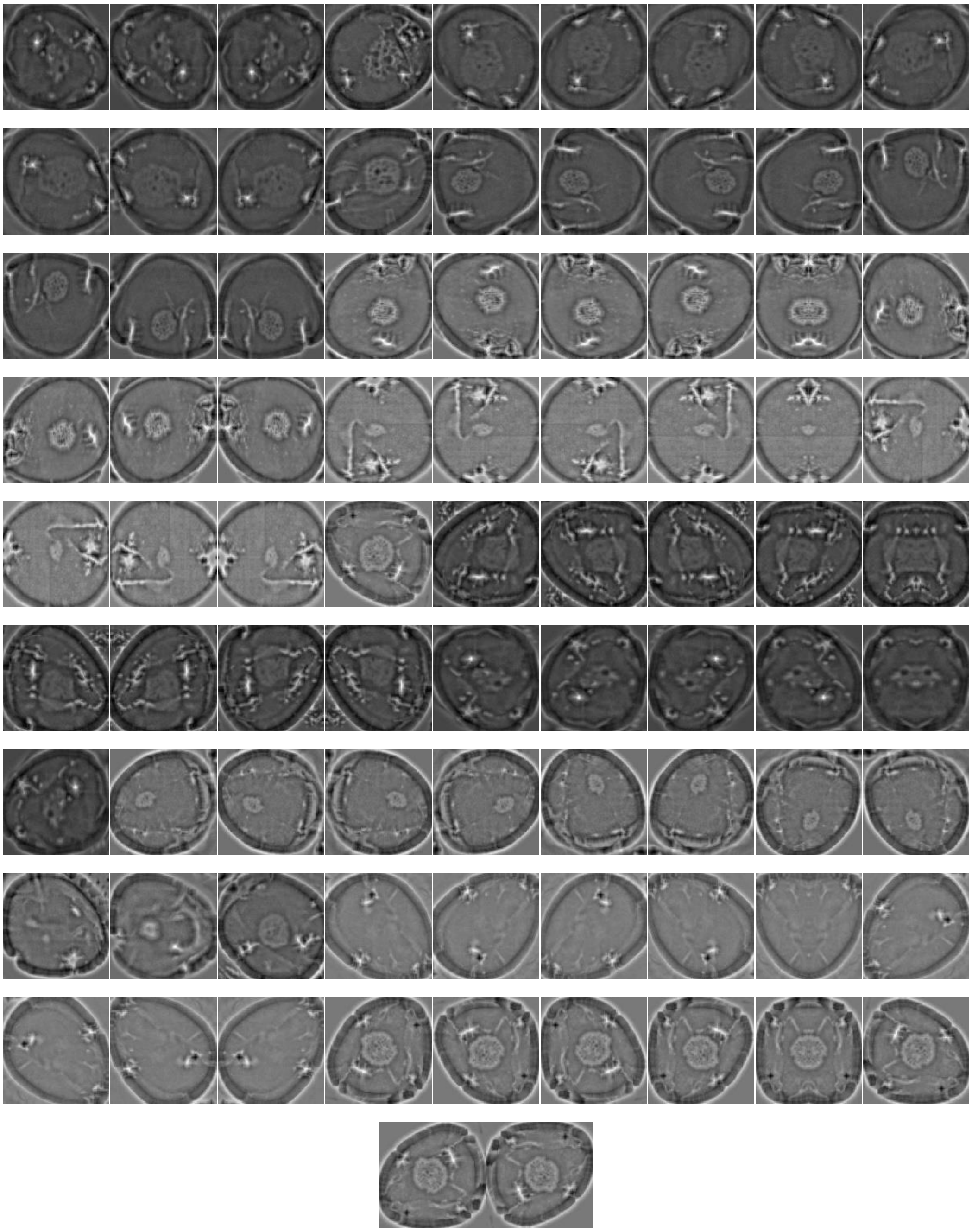

Figure 5.2: Injured cornea with image augmentation.

:

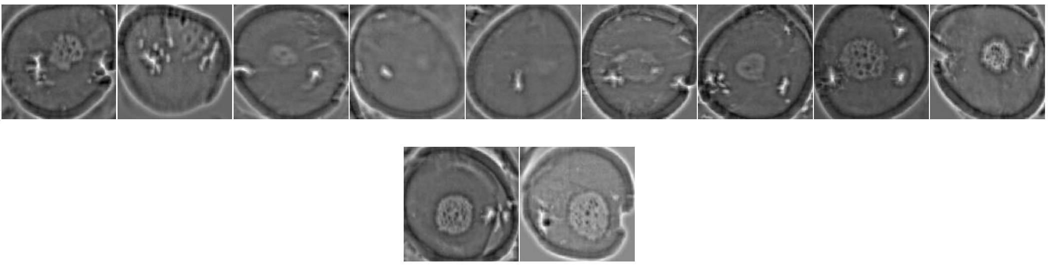

Figure 5.3: Healthy cornea without image augmentation.

The input image was resized to 227×227×3, while the network was trained with a single CPU. The layers other than the last three were transferred directly (the layer weights of the pretrained network remains) to the new classification task, whilst the final three layers were replaced with other layers, namely a fully connected layer, a softmax layer, and a classification output layer. The new fully connected layer was trained to classify the cornea images limited to only two classes. In the case of increasing the learning rate in the new layers, the values for both the weight learn rate factor and the bias learn rate factor were set to 20 with a small initial learning rate of 0.001, including the number of epochs to five. Finally, the cornea images were trained in a network that consists of the transferred and the new layers. As a result, the validation images managed to be classified using the fine-tuned network, while the accuracy was computed from the fraction of labels correctly predicted by the network.

5.4 Mixture AlexNet and SVM-Linear

The third approach employed in this study refers to the image feature extraction with pretrained AlexNet, which is considered as the easiest and fastest way to exploit the representational power of pretrained deep networks. In particular, the network is responsible of producing a hierarchical representation of input images. Meanwhile, activations on the fully connected layer 'fc6' are used for feature extraction of the training and test images as can be seen in **Figure 5.4**.

The class labels from the training and test data were extracted. Next, the features extracted from the training images were utilised as the predictor variables, which was then trained using linear support vector machine (SVM). Overall, the test images were classified using the trained SVM model based on the features extracted from the test images.

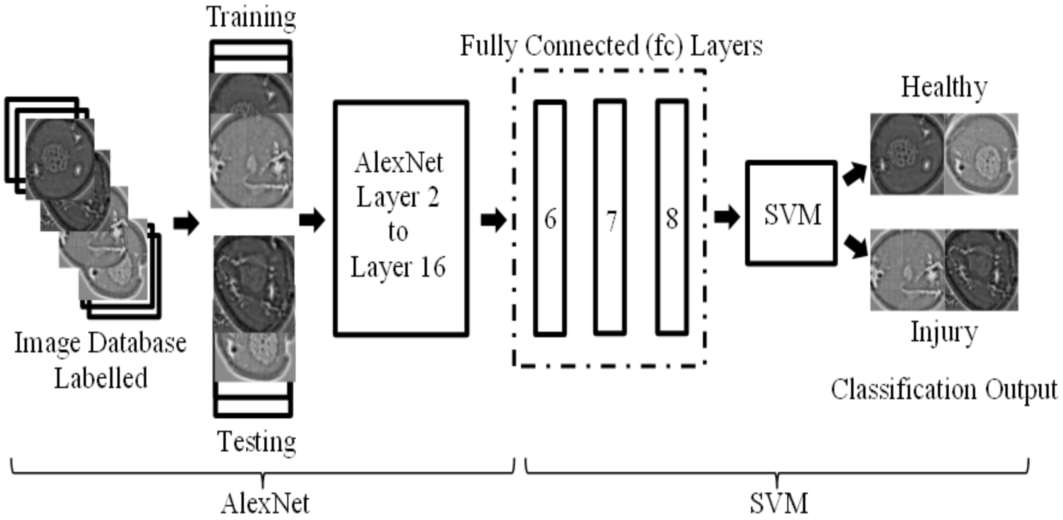

Figure 5.4: Feature extraction with pretrained AlexNet on cornea images classification using SVM.

The fusion of AlexNet and SVM-linear classifier was used for comparison to the standalone AlexNet. Due to the complex architecture involved in AlexNet, the learning process can be very time-consuming. This disadvantage could potentially be resolved by the use of a graphics processing unit (GPU). However, GPU is less readily used or available, thereby limiting future applicability. Therefore, for central processing unit (CPU) users, the combination of AlexNet and SVM-linear is more than sufficient, where AlexNet performs the high-level feature extraction while SVM-linear carried out the classification (**Figure 5.4**).

Figure 5.5 depicts the samples of features extracted from convolution 1, convolution 5, and fully-connected 8 (FC8). In the present study, there are three possible layers of feature extraction output in AlexNet, namely FC6 (layer 17), FC7 (layer 20), and FC8 (layer 23) that consist of 4096, 4096, and 1000 feature dimensions, respectively. More importantly, any of these three layers can be used as feature representation entries to the SVM classifier. In this combination, convolutional layers were employed for the purpose of learning a better representation of the input image. Meanwhile, SVM classification was performed on the fc output during the training and testing with such automatically extracted features. Therefore, this is a clear explanation as to why AlexNet-SVM tends to run much faster than a standalone AlexNet.

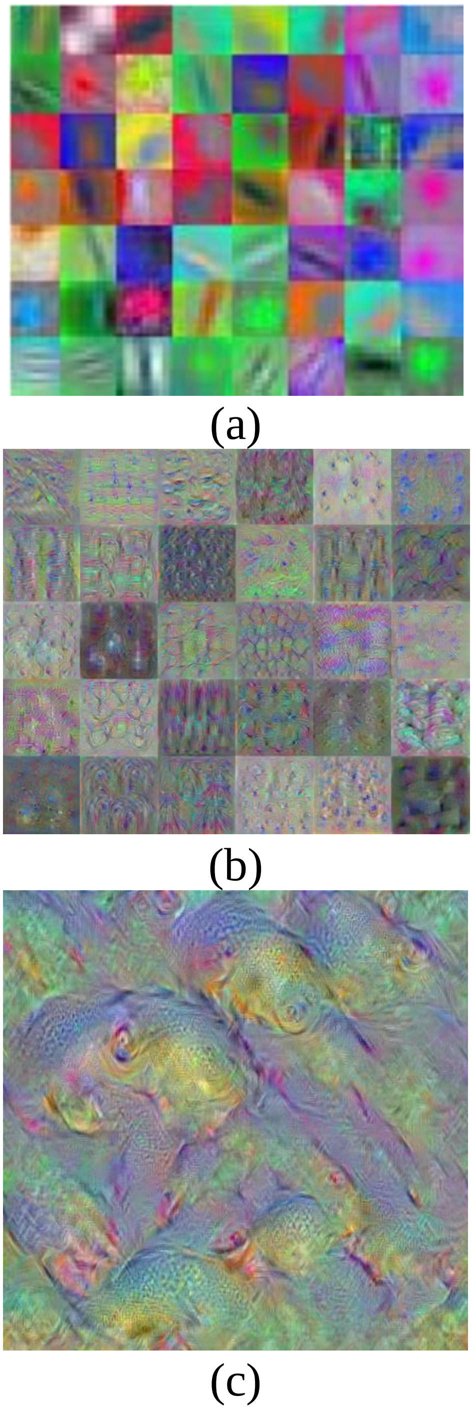

Figure 5.5: Sample of features extraction. (a); Conv1 (56 channels); (b); Conv5 (30 channels); and (c) FC8 layer (channel 1).

5.5 Results and Performance

Table 5.3 shows the results of classification performed by SVM-GRBF using the four features extracted from the histogram for testing data (data were unseen during training). In particular, it represents the number of iterations required for convergence, accuracy, and error during the testing of different sets of hyperparameters.

Table 5.3: Four features classification using SVM-GRBF.

Features	**C = 1**			**C = 500**			**C = 500**		
	Sigma = 1			**Sigma = 1.658**			**Sigma = 2.658**		
	10-Fold Cross Validation			**10-Fold Cross Validation**			**10-Fold Cross Validation**		
	Iterations	**Accuracy**	**Error**	**Iterations**	**Accuracy**	**Error**	**Iterations**	**Accuracy**	**Error**
Mean-Std.	13	0.2708	0.4545	81	0.5625	0.3636	578	0.4792	0.4545
Mean-Skew	13	0.8333	0.3636	148	0.9583	0.4545	412	**1**	0.4545
Mean-Kurt	6	0.7500	0.3636	169	0.8125	0.3636	189	0.5208	0.2727
Std.-Skew	10	0.6042	0.4545	161	0.2083	0.5455	207	0.1875	0.6364
Std.-Kurt	6	0.3750	0.1818	419	0.6875	0.6364	172	0.7083	0.4545
Skew-Kurt	12	0.6875	0	200	0.5833	0.1818	243	0.7292	0.0909
4-Features	11	0.4375	0.3636	38	0.7292	0.4545	86	0.4583	0.4545

The results showed that a combination of 2D features of mean and skewness is able to yield 100% accuracy, particularly when C and Sigma are increased sufficiently. **Figure 5.6** illustrates the decision boundaries and support vectors.

The performance of the classifiers is measured based on confusion matrix as presented in **Table 5.4**. First, the cornea injury that is correctly identified as injured by the network is called as True Positives (TP). Second, the healthy cornea correctly identified by the network as healthy is described as True Negatives (TN). Third, False Positives (FP) is used to label the cornea predicted as injured but is actually healthy. Finally, False Negatives (FN) describes the injured cornea that is incorrectly recognised as injured. In this case, false positives are more preferred than false negatives when detecting injured cornea because false negatives is regarded as the worst possible case, particularly when the injured cornea is measured as healthy.

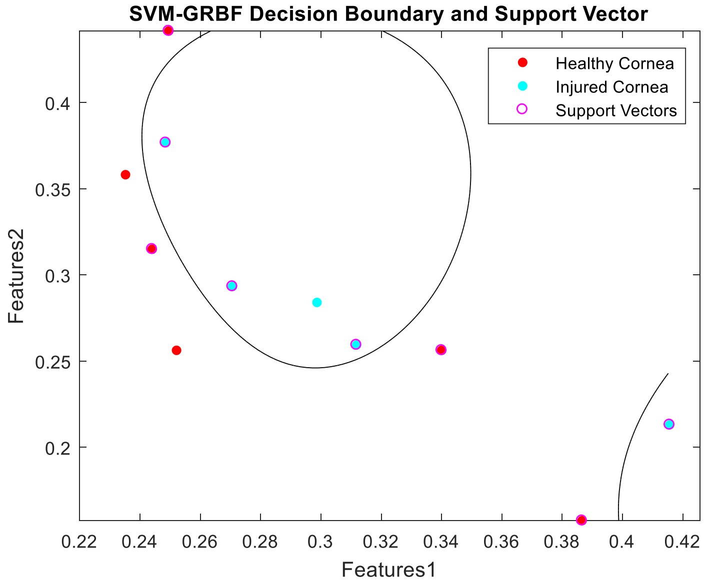

Figure 5.6: Decision boundary and support vector for mean vs skewness (testing data).

Table 5.4: Confusion Matrix.

Confusion Matrix	**Predict Injured**	**Predict Healthy**
Actual Injured	True Positives (TP)	False Negatives (FN)
Actual Healthy	False Positives (FP)	True Negatives (TN)

The accuracy was calculated as the area under the receiver operating characteristic (ROC) curve, which was then computed using LibSVM-MATLAB. The error refers to the generalisation error which is described as the out-of-sample mean squared error with the purpose of measuring how accurately a model is able to predict outcome values for previously unseen data. The ROC curve for 2D feature classification is shown in **Figure 5.7**.

The ROC is a metric used to check the accuracy of classifiers. By definition [108], [109] a ROC curve shows True Positive Rate (TPR) versus False Positive Rate (FPR) for different thresholds of the classifier output. The maximum area under the curve (AUC) is

1, which corresponds to a perfect classifier. Larger AUC values indicate better classifier performance. From the ROC curve, 2D features of mean vs skewness yielded an optimal accuracy compared to other combinations of features. This ROC curve can be used for feature selection to classify cornea images.

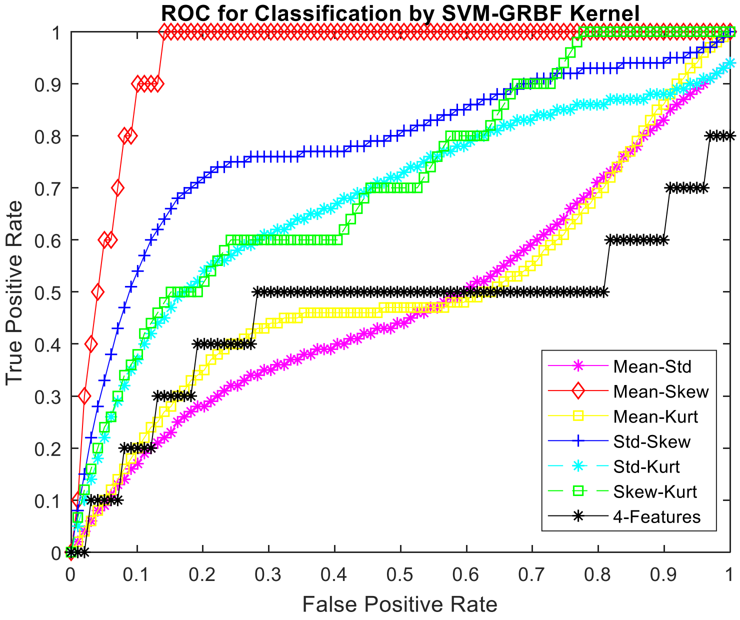

Figure 5.7: ROC curve for 2D-features classification by SVM-GRBF with C = 500, and Sigma = 1.658.

The results of the second and third approaches to classify physical images features according to AlexNet and AlexNet-SVM linear, with respect to accuracy as in **Figure 5.8** and the time consumed in **Figure 5.9**.

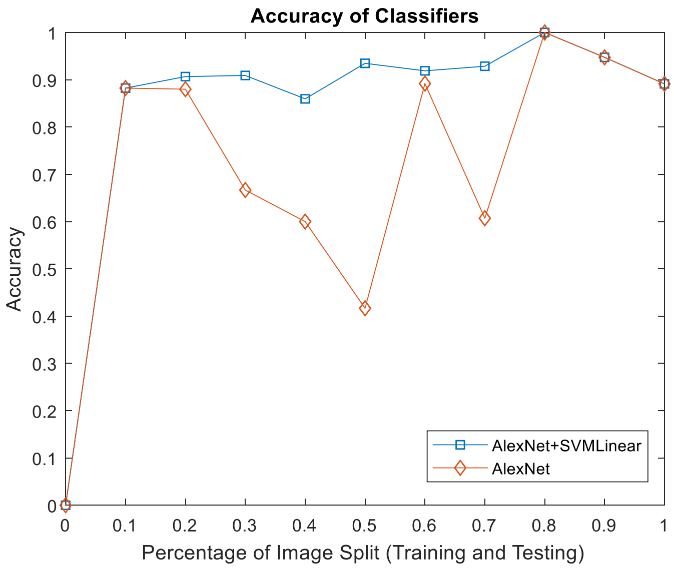

Figure 5.8: The accuracy of AlexNet and AlexNet-SVM classifier.

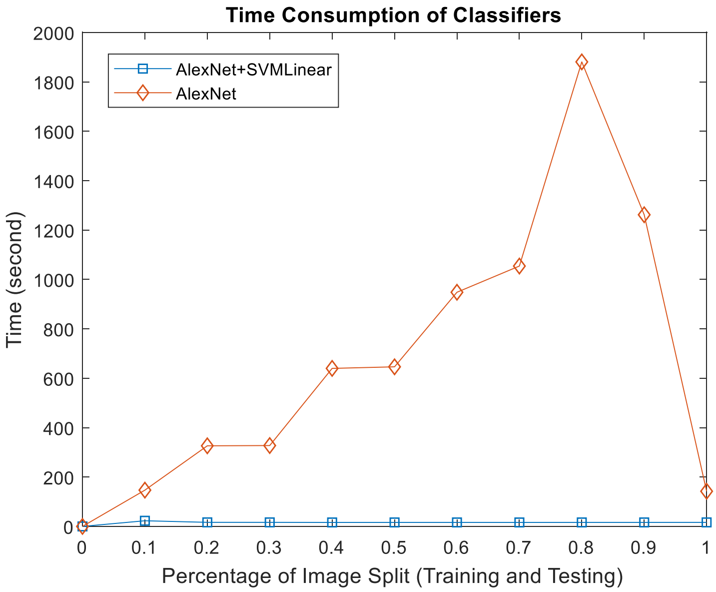

Figure 5.9: The time consumption of AlexNet and AlexNet-SVM linear classifiers.

Both AlexNet with and without SVM yielded 100% accuracy at 0.8 (80% training, 20% testing) based on image training and testing distribution, although AlexNet without SVM performed poorly in-terms of computation time. This result proved that mixed SVM in the AlexNet as a classifier will improve the processing time.

5.6 Parameter of Injured Boundary

Image quantification was performed following image classification. In regard to this matter, quantification of these images is essential in providing objectivity considering that medical imaging plays a role in medical assessments [65]. Ideally, an imaging assessment algorithm must be precise and capable of generating numerical quantification in a rapid fashion. Hence, the technique must utilize statistical approach for robustness in order to produce the expected outcome [110]. Here we looked statistical approach at five measurements for computation of the image: 1. Entropy (E) is measured randomness of the image pixels denoted in (Eq. 29). 2. No. of pixels also called as area (A) is determined by counting pixels contained within a boundary. 3. Perimeter (l) is the total length of the segmentation area. 4. The centroid (xc,yc) is computed two points of elements in the row and column to specify the center mass of the object denoted in (Eq. 30). 5. Finally, eccentricity (Ec) is the ratio of the longest (lc) and maximum length (lp) within the boundary pixels denoted in (Eq. 31).

These listed measurements of the image are available built-in MATLAB code known as ‘regionprops' (measure properties of image region), and the mathematical definitions of entropy, centroid, and eccentricity are given as follows. Entropy (E):

$$E = -\sum_{ij} P_{ij}\, logP_{ij} \qquad \text{Eq. 29}$$

Where P_{ij} is the histogram count from the imhist operation.

Centroid (*xc*,*yx*):

$$xc = \frac{1}{N}\sum_{i=1}^{N} x_i \qquad \text{Eq. 30}$$

$$yc = \frac{1}{N}\sum_{i=1}^{N} y_i$$

Where *N* is a number of pixels in the boundary, xi and yi are the row and column points of pixel *N*, respectively.

Eccentricity (*Ec*):

$$lc\ (lp) = \sqrt{(x2 - x1)^2 + (y2 - y1)^2} \qquad \text{Eq. 31}$$

$$Ec = lc/lp$$

Where *lc* is the longest length, *lp* is maximum (perpendicular with *lc*) length of foci boundary, and the two points of pixels in the respective length denotes as *(x1, y1), (x2, y2).*

In the **Figure 5.10**, row 1 at columns 2 and 3 show a binary mask and a perimeter of the injured region respectively, whereas in the row 2 at column 2 shows an injured area in a blue color and the binary mask image with mathematical morphology was applied in the column 3.

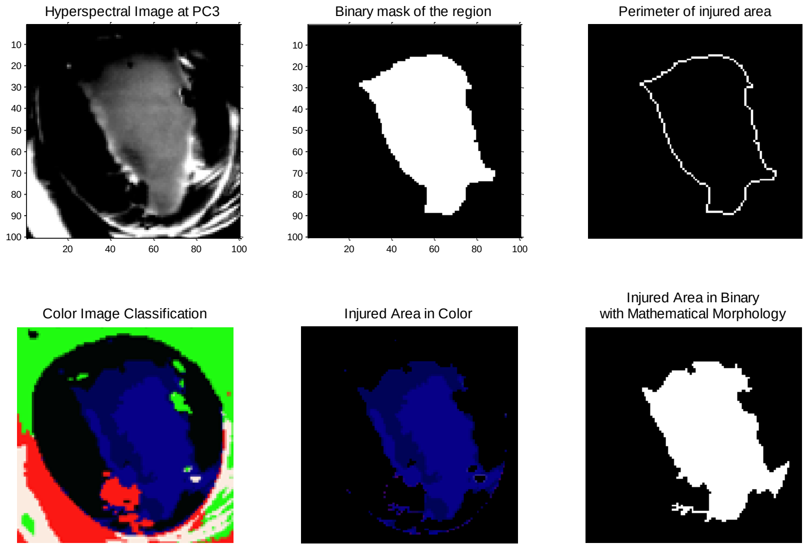

Figure 5.10: Image in size 100 x 100. Row 1: Human segmentation using selected image from one PCs. Row 2: Machine/colour image segmentation using RGB image selected from three PCs.

The entropy, no. of pixels, centroid, perimeter, and eccentricity were tabulated in **Table 5.5**.

Table 5.5: Quantification of eye injury (comparison of human and machine segmentation).

Items	Entropy	No. of Pixels	Centroid	Perimeter (Pixels)	Eccentricity
EYE8 Human	4.2519	1949	57.7, 49.4	210.8	0.99
EYE8 Machine	3.5247	2993	60.9, 56.1	618.3	0.68
EYE9 Human	5.6581	3992	58.2, 47.7	286.2	0.89
EYE9 Machine	4.8547	4280	57.7, 47.1	424.4	0.75
EYE10 Human	5.5148	4164	55.9, 54.5	277.3	0.95
EYE10 Machine	5.5566	4153	57.0, 56.6	452.3	0.82
EYE11 Human	4.7504	2684	58.1, 48.6	240.7	0.88
EYE11 Machine	5.1956	2714	59.5, 51.4	343.9	0.79

These parameters were quantified and obtained from the injured areas using five types of shape measurement. The no. of pixels and perimeter imply the size of the injured area. The centroid allows the location of the injury to be best estimated. Finally, eccentricity indicates the shape of the injured area close to line segment (closer to 1) or circle (closer to 0).

5.7 Summary

In summary, the image acquired from hyperspectral imaging managed to produce better result in assessing corneal epithelium injury. The combination of spatial and spectral features was revealed to be particularly useful for gathering clinical information. In the case of this study, different approaches were employed to identify injury on the images due to the transparent nature of the cornea, with and without fluorescein staining.

On another note, features crafting (histogram) and features learning (deep learning) for features extraction method were used for comparison purposes. In regard to this matter, features crafting involves a human designing features that are fed into a classifier, whereas features learning refers to having an algorithm create feature itself [111], [112], [113]. Features learning is motivated by the fact that machine learning tasks such as classification often require input that is mathematically and computationally convenient to process.

However, it is important to realize that real-world data such as images and video are usually complex, redundant, and highly variable. Hence, it is deemed necessary to discover useful features from raw data. On the other hand, traditional hand-crafted features/features crafting is known to involve expensive human labor and highly dependent on expert knowledge. Moreover, one of the drawbacks is that they normally cannot be generalized well. Therefore, this has motivated the design of efficient feature learning techniques for automation and generalization purposes.

Overall, it can be concluded that the mixture AlexNet-SVM (features learning) is the most suitable technique that can be used for cornea assessment among the three classification approaches based on the accuracy and time consumption. The algorithm proposed which involves the use of optimal classifier can be used for objective measurement (image quantification) in order to help the clinician to identify normal and abnormal tissues automatically.

CHAPTER 6

A NEW MIXING KERNEL FOR SUPPORT VECTOR MACHINE CLASSIFIER (3-CONVSVM)

This chapter describes the third knowledge contributions in this study. A new 3-convex combination kernels function is introduced for the binary SVM classifier. In fact, it is important to note that kernel development for SVM has received considerable attention in the last few years for hyperspectral image classification [114], as well as its recent utilisation in medical study [115]. The purpose of choosing binary classification in the current observation is due to the fact that most medical data are commonly classified into two-class problems, namely benign or malignant which is helpful in detecting breast cancer, healthy or disorder in liver diagnosis, injured or no injury in eyes disease, and present or absent of diabetes and heart assessments.

The proposed method (**Figure 6.1**) was applied with numerical experiments on several number of selected datasets. The datasets were iris dataset, breast dataset, diabetes dataset, heart dataset, liver dataset, satellite dataset, and pig's eyes dataset. In particular, different type of datasets which include medical, general, and hyperspectral as well as the level of samples complexity were employed in this study for the purpose of producing the generalisation ability for the proposed mixing kernels. Meanwhile, several aspects were computed and recorded which include the number of iterations, support vectors, classification training time, training and testing accuracy, and generalisation loss during the testing. In addition, it is worth to note that all datasets were added with outliers and Gaussian noise with the aim of observing the kernel sensitivity. Finally, a comparison analysis was carried out between the accuracy of 3-convex kernel after tuned loss and the single-kernel and 2-convex kernel combination.

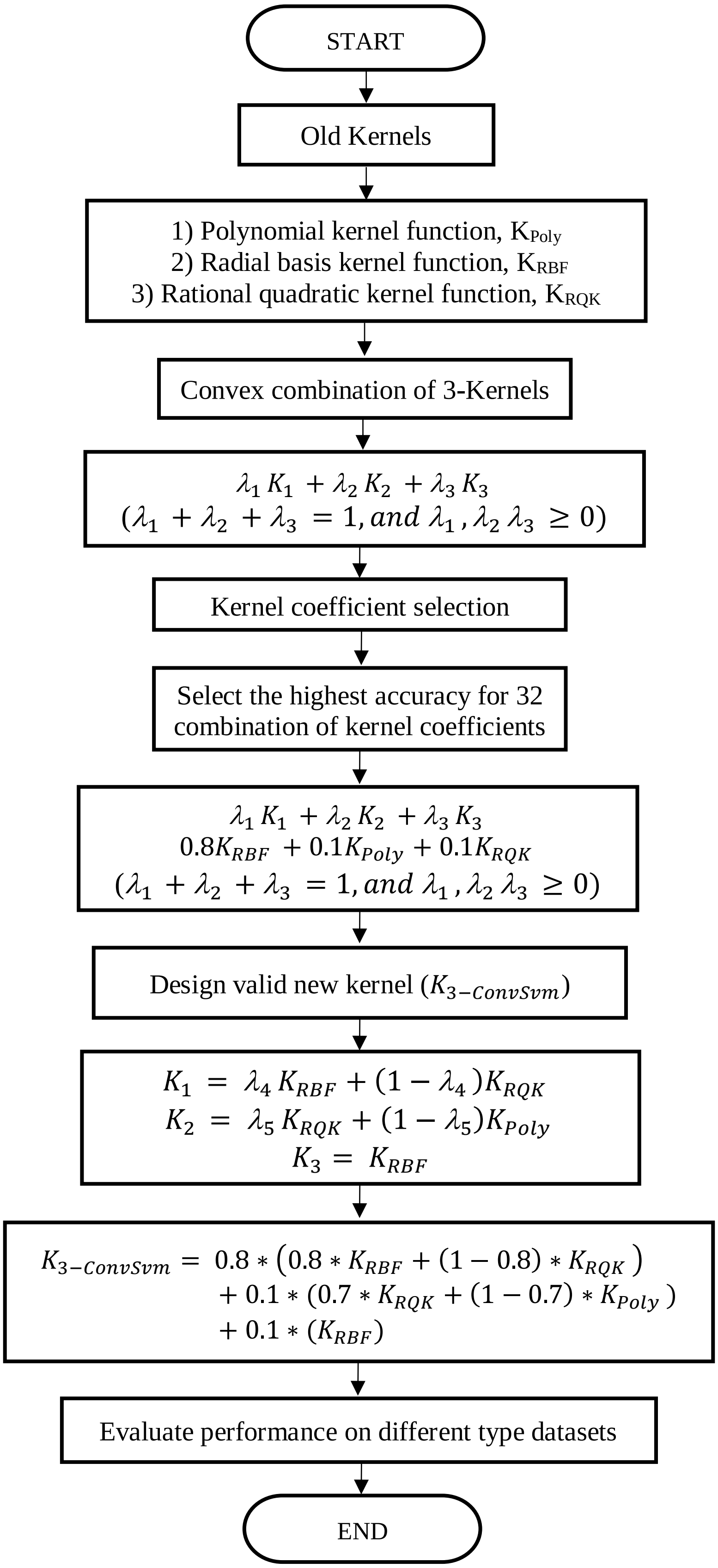

Figure 6.1: Framework of new mixing kernel for SVM.

6.1 Developing New Kernel from Old Function

The essential step in SVM classification include the need to determine the appropriate kernel function. Specifically, kernel function is commonly applied in a nonlinear problem that transforms data space into a high-dimensional feature space with the aim of forming a linear model. Hence, it is possible for the nonlinear data to be separable into two labels of classes. More importantly, the modify existing functions with the aim of making new ones are deemed possible provided that the kernel is valid and the combination is admissible [114], [83].

A considerable amount of research indicated that combined kernels are able to produce improved classification accuracy compared to the use of a single kernel [116], [117], [118], [119], [120]. In this case, the most critical step is to provide suitable hyperparameters in order to combine the coefficients from different kernels. Meanwhile, past studies also managed to explore different techniques that can be employed in obtaining optimal classification results which include grid search [121], particle swarm optimization (PSO) [122], and genetic algorithms (GA) [123]. Nevertheless, the hyperparameters used in the present study were fixed in all analyses considering that the aim was to provide a comparison across single and combined kernels instead of maximising the accuracy. Moreover, it is worth to note that the parameters might be tuned to reduce generalisation loss.

6.1.1 Standard Kernel Functions and Covariance Function Characteristics

The standard kernel functions in SVM used in this study are listed below except the RQK which is known as the covariance function used in Gaussian processes:

1) Linear kernel function:

$$K_{Linear}(x, x') = (x * x') \qquad \text{Eq. 32}$$

Linear kernel is a basic kernel function to resolve a linear problem by providing the hyperplane in sample space.

2) Polynomial kernel function (Poly):

$$K_{Poly}(x, x') = |(x - x') + r|^{d} \qquad \text{Eq. 33}$$

where r is the is the offset coefficient that is normally 1, while d denotes the degree of polynomial kernel, d > 0.

3) Radial basis kernel function (RBF):

$$K_{RBF}(x, x') = \exp\left(-\frac{|x - x'|^{2}}{2\sigma^{2}}\right) \qquad \text{Eq. 34}$$

where σ is RBF kernel parameter. Moreover, the radius of influence of the support vectors changes according to different values of σ.

4) Rational quadratic kernel function (RQK):

$$K_{RQK}(x, x') = \left(1 + \frac{|x - x'|^{2}}{2\alpha\sigma^{2}}\right)^{-\alpha} \qquad \text{Eq. 35}$$

similar like RBF when α is infinity. Where α denotes the relative weighting of maximum and minimum scale variations.

Figure 6.2 shows the characteristic of polynomial kernel as described in Eq. 33. In this case, it should be understood that the increase in the deviation between input data x and test input (0.1) value xi is always greater than zero apart from causing the K value to increase on the right and decrease on the left side of xi. Hence, this clearly shows that the overall properties of the data points far away from the test points in the dataset may also cause an impact on the value of the kernel function.

On another note, larger d (1, 2, 3, 4, 5) value leads to larger curvature of the curve, which causes the distribution of the K value to be increasingly uneven. On a more important note, it is argued that the overall properties of kernel will be weakened, while its generalisation ability which is also known as extrapolation ability will become weaker with the increase of the d value [118].

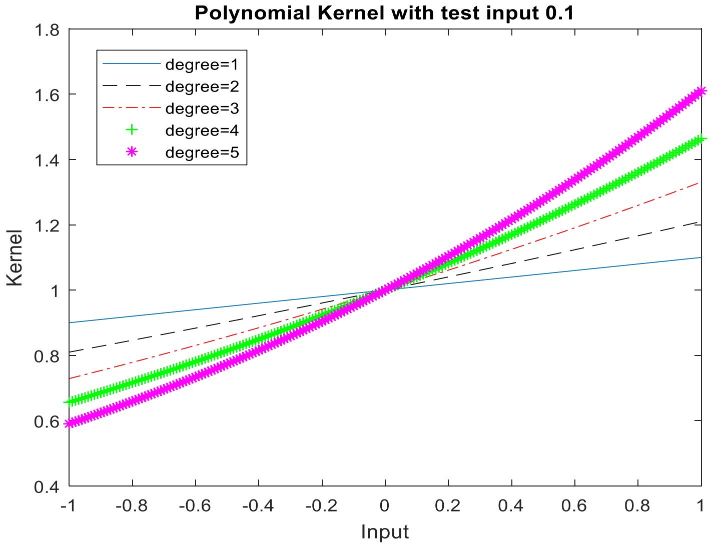

Figure 6.2: The characteristics curve of polynomial kernel with increased polynomial degree, *d*.

Figure 6.3 shows the characteristic of RBF kernel as illustrated in Eq. 34. As can be observed in the figure, the K value is larger in the vicinity of the test input value xi. In this case, the increase in the deviation between x and xi tends to decrease the K value. Hence, this shows that only data points close to the test points in the dataset have an impact on the value of the kernel function.

The larger the σ (0.1, 0.2, 0.3, 0.4, 0.5) value, the larger the curve control interval. On a similar note, larger value of σ leads to larger K value corresponding to the same x, which causes the distribution to be more even. Moreover, it was also suggested that the RBF will be weakened and its learning ability will become weaker with the increased value of σ [123].

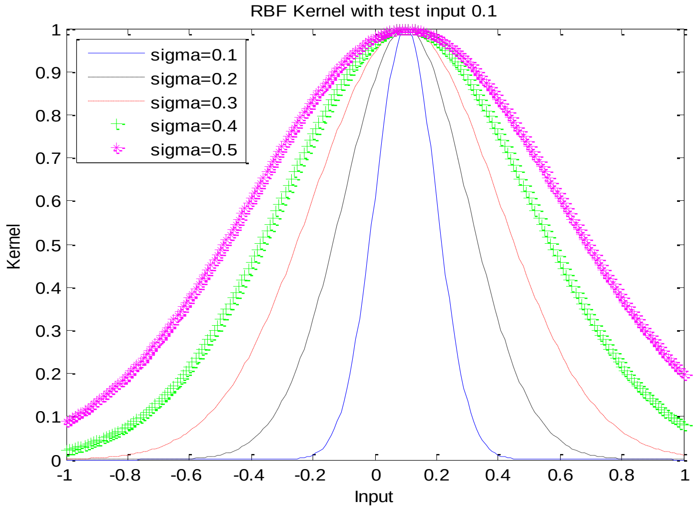

Figure 6.3: The characteristics curve of RBF kernel with increased sigma, σ.

The characteristics of RQK kernel as described in Eq. 35 are shown in

Figure 6.4. As can be seen, the RQK kernel is equivalent to adding together many RBF kernels with various kernel parameters. The parameter α determines the relative weighting of small and large-scale variations. Hence, the RQK is identical to the RBF if α is infinity.

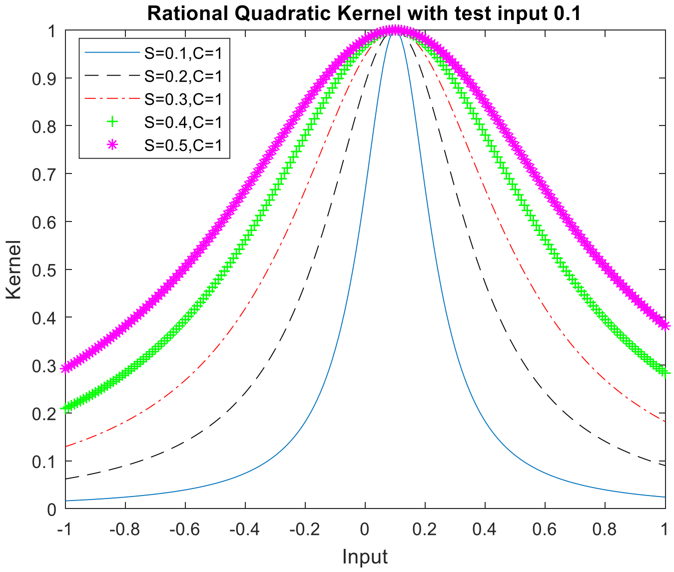

Figure 6.4: The characteristics curve of RQK kernel with increased sigma, σ with same value of C=1.

6.2 Proposed 3-Convex Kernels Combinations (3-ConvSvm)

It is worth to note that there are several ways of mixing kernels. The most important concern is that the resulting kernel must be an admissible kernel. In this case, the sum of two kernels is considered as a valid kernel. Consideration to the random process $f(x)=f_1(x)+f_2(x)$, where $f_1(x)$ and $f_2(x)$ are independent which lead to $k(x, x^{'})= k_1(x, x^{'})+ k_2(x, x^{'})$ [83]. This construction can be used to add together kernels with different characteristics length-scales.

On another note, a convex combination has been recommended to be used on the valid kernel [124] as one of the methods to guarantee that the mixed kernel is admissible. This study used the following method to construct a new mixed-kernel function. One of the examples of convex combination of two kernels is as follows:

$$K_{Mix} = \lambda_1 K_1 + (1 - \lambda_1) K_2 \qquad \text{Eq. 36}$$

As shown in the Eq. 36, it is necessary to determine the optimal mixing weight coefficient (λ) whereby the value of λ is a constant scalar. Convex combinations involve the coefficients to sum to 1 and are non-negative [125].

One of the examples of mixing kernel known as PRBF is shown in Eq. 36. It is worth to note that the combination of polynomial and RBF kernel has been presented in previous study [124]. **Figure 6.5** illustrates the characteristic graph of PRBF where the total weight coefficient, $\lambda = 1$. In this case, the kernel parameters were set as C = 1, 2, 3, 4, and 5, while d and σ were 2 and 0.25, respectively.

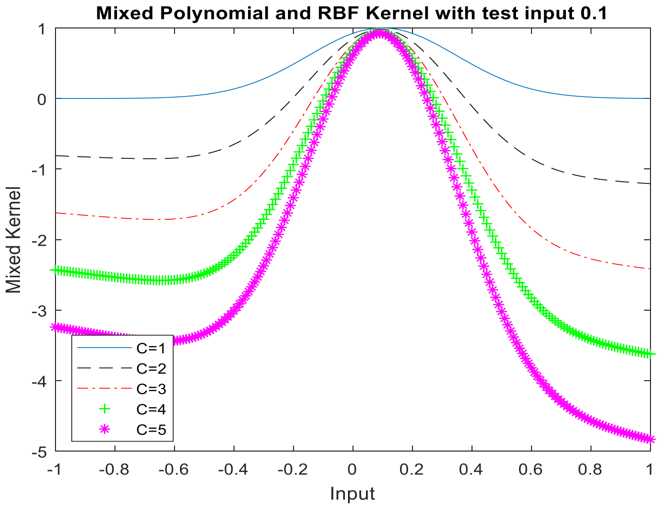

Figure 6.5: The characteristics curve of mixed RBF and polynomial kernel with different kernel parameters, C with test input 0.1. Where, d = 2, σ = 0.25.

The PRBF which is known as an integrated global kernel (polynomial) and local kernel (RBF) function tends to have a great impact on the data samples closer to the test points as well as a certain impact on the data samples far from the test points. Moreover, PRBF was suggested as a strong kernel function model in both learning ability and generalisation ability. More importantly, its learning ability is said to be stronger than the global kernel function, while its generalisation ability is stronger than the local kernel function. The PRBF kernel is able to improve the SVM classification accuracy by determining the suitable parameters compared to the single kernel [120].

Therefore, the sum of three kernels is also considered as a valid kernel. Here, the 3-convex combination kernel is proposed as shown below:

$$K_{3-ConvSvm} = \lambda_1 K_1 + \lambda_2 K_2 + \lambda_3 K_3$$

$$(\lambda_1 + \lambda_2 + \lambda_3 = 1, and\ \lambda_1, \lambda_2\, \lambda_3 \geq 0)$$

Eq. 37

Where,

$K_1 = \lambda_4 K_{RBF} + (1-\lambda_4)K_{RQK}$, $K_2 = \lambda_5 K_{RQK} + (1-\lambda_5)K_{Poly}$, and, $K_3 = K_{RBF}$

The $\lambda_1, \lambda_2, \lambda_3$ and λ_4, λ_5 are kernel coefficients to sum to 1 and non-negative in order to form convex combinations. K_{RBF} denotes the RBF kernel, K_{RQK} refers to RQK kernel, and K_{Poly} is known as polynomial kernel.

Figure 6.6 shows the characteristics of the new kernel construction as shown in Eq. 37.

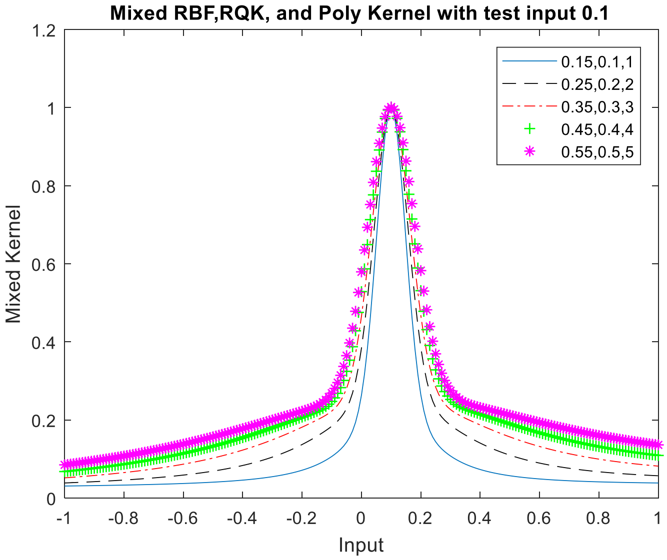

Figure 6.6: The characteristics curve of 3-ConvSvm kernel with different kernel parameters with $C = 1$. The kernel coefficient is set as: $(K_{3-ConvSvm} = 0.8 * (0.8 * K_{RBF} + (1-0.8) * K_{RQK}) + 0.1 * (0.7 * K_{RQK} + (1-0.7) * K_{Poly}) + 0.1 * (K_{RBF}))$.

6.2.1 Kernel Coefficient Selection for 3-Convex Combination

In this case, it is necessary to first determine the admissible range for the weight coefficient of each kernel. **Table 6.1** illustrates the 32 possible combination for the convex kernel coefficient that was tested on the pig's eyes dataset. Moreover, the accuracy for all these combinations were computed as depicted in **Figure 6.7**.

Table 6.1: Possible combination for the convex kernel coefficient.

No.	λ1 (RBF)	λ2 (Poly)	λ3 (RQK)	No.	λ1 (RBF)	λ2 (Poly)	λ3 (RQK)
1.	***0.8***	***0.1***	***0.1***	**17.**	0.1	0.6	0.3
2.	0.5	0.4	0.1	**18.**	0.5	0.1	0.4
3.	0.4	0.5	0.1	**19.**	0.4	0.2	0.4
4.	***0.1***	***0.8***	***0.1***	**20.**	0.3	0.3	0.4
5.	0.7	0.1	0.2	**21.**	0.2	0.4	0.4
6.	0.6	0.2	0.2	**22.**	0.1	0.5	0.4
7.	0.5	0.3	0.2	**23.**	0.4	0.1	0.5
8.	0.4	0.4	0.2	**24.**	0.3	0.2	0.5
9.	0.3	0.5	0.2	**25.**	0.2	0.3	0.5
10.	0.2	0.6	0.2	**26.**	0.1	0.4	0.5
11.	0.1	0.7	0.2	**27.**	0.3	0.1	0.6
12.	0.6	0.1	0.3	**28.**	0.2	0.2	0.6
13.	0.5	0.2	0.3	**29.**	0.1	0.3	0.6
14.	0.4	0.3	0.3	**30.**	0.2	0.1	0.7
15.	0.3	0.4	0.3	**31.**	0.1	0.2	0.7
16.	0.2	0.5	0.3	**32.**	0.1	0.1	0.8

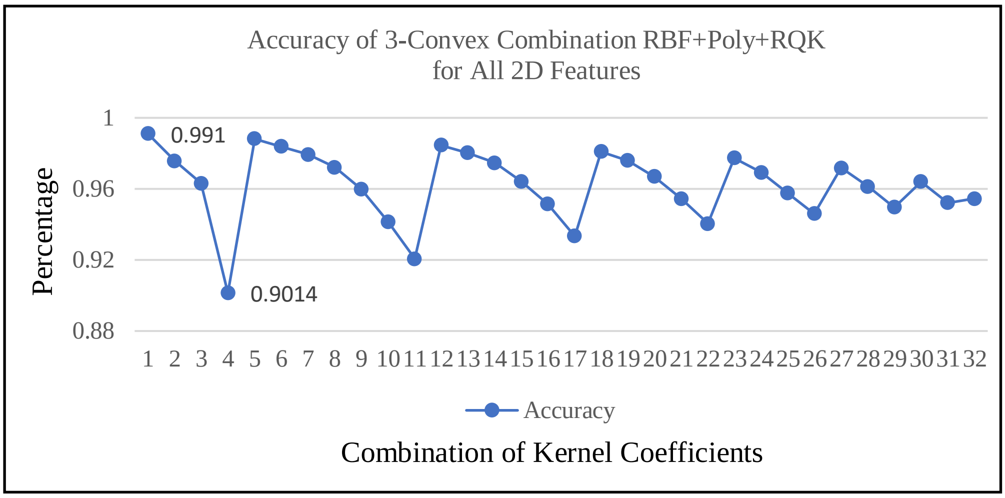

Figure 6.7: The accuracy of 32 convex kernel combination.

The result of 1st combination yields a higher accuracy at 99%, while the combination in no.4 is recorded only as 90%. Therefore, higher weight coefficient belongs to RBF kernel, whereas the smallest is for polynomial and RQK kernel with the purpose of achieving the optimal classification. Apart from that, it is worth to note that the 1st combination is used for the all analyses.

6.3 Performance of the New Mixing Kernel

In this study, the performance of new mixing kernel was measured using various datasets. Specifically, the seven datasets that were used include one owned dataset (**Figure 6.8**), whereas the remaining six datasets were obtained from UCI repository [126] as follows: Iris (**Figure 6.9**), breast (**Figure 6.10**), diabetes (**Figure 6.11**) , heart (**Figure 6.12**), liver (**Figure 6.13**), and satellite (**Figure 6.14**). The sample size that was employed in this study are as follows: 25 samples (pig's eyes), 100 samples (iris), 683 samples (breast), 768 samples (diabetes), 297 samples (heart), 345 samples (liver), and 1333 samples (satellite).

Furthermore, the five types of datasets were categorised as medical dataset, while iris and satellite were respectively categorised into the general and hyperspectral category. As presented in **Figure 6.8** to **Figure 6.14**, it can be observed that each dataset has different complexity in terms of the data distribution for the purpose of envisaging that the mixing kernel will work well on any dataset.

Meanwhile, it should also be noted that all datasets were non-linear problem for the binary classification. According to the best classification result presented in Chapter 5 (**Figure 5.8**), each dataset was randomly divided into 80% training and 20% testing in corresponds to data partitioning.

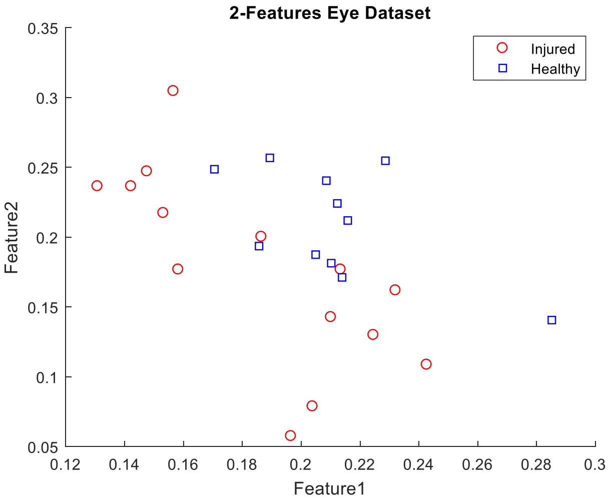

Figure 6.8: Pig’s Eyes dataset (total:25, training: 19, testing: 6).

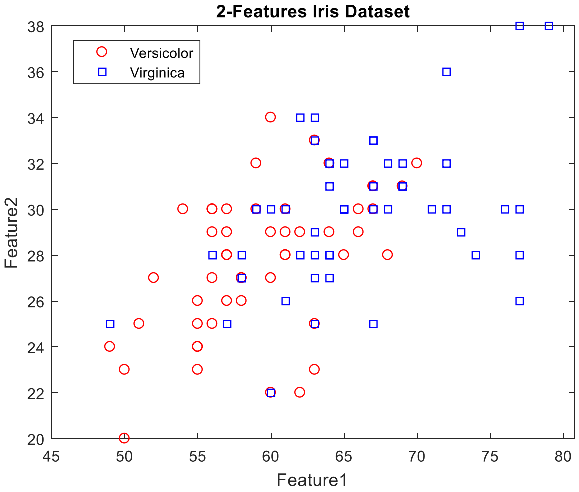

Figure 6.9: Iris dataset (total: 100, training: 80, testing: 20).

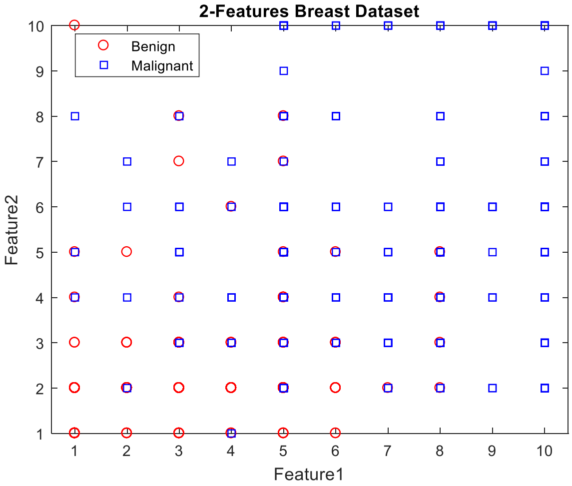

Figure 6.10: Breast dataset (total: 683, training: 543, testing: 140).

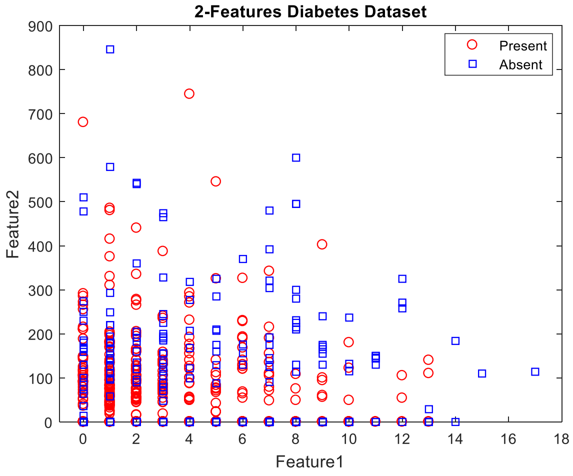

Figure 6.11: Diabetes dataset (total: 768, training: 614, testing: 154).

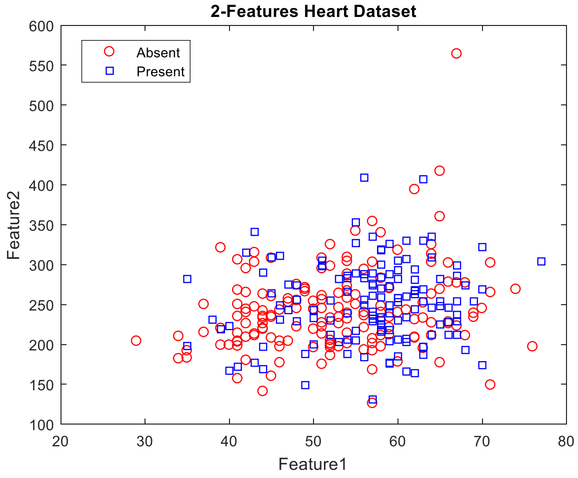

Figure 6.12: Heart dataset (total:297, training:238, testing:59).

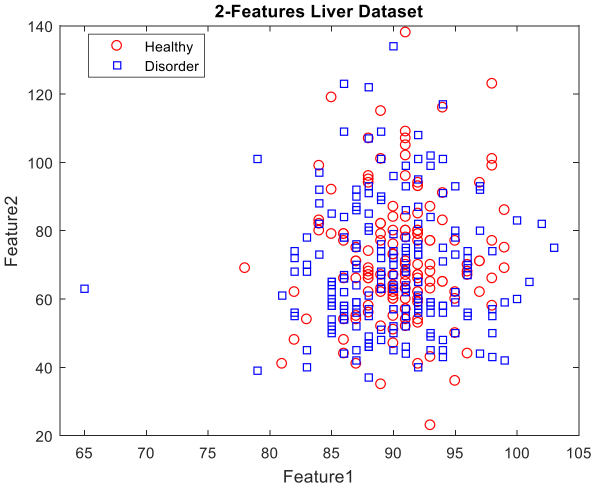

Figure 6.13: Liver dataset (total:345, training:276, testing:69).

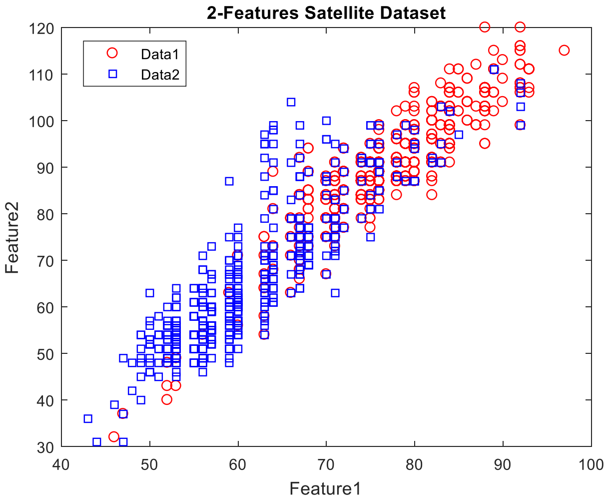

Figure 6.14: Satellite dataset (total:1333, training:858, testing:475).

In regard to this matter, noisy data was added on the testing dataset instead of the training samples. Two types of noise [127], [128] known as the class noise (**Figure 6.15**) and attribute noise (**Figure 6.16**) were added in the test dataset for the purpose of observing the kernel sensitivity. In particular, outliers are described as points in the region of some class but with a wrong label that are known as class noise, while attribute noise is considered as points in each class in which its attributes are randomly chosen.

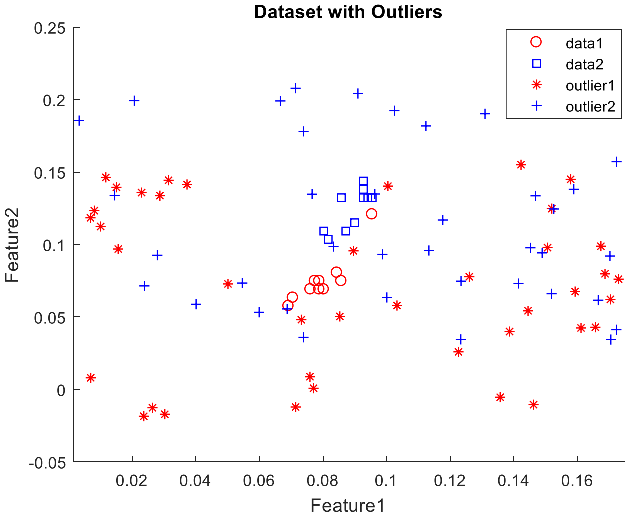

Figure 6.15: Adding class noise in the dataset.

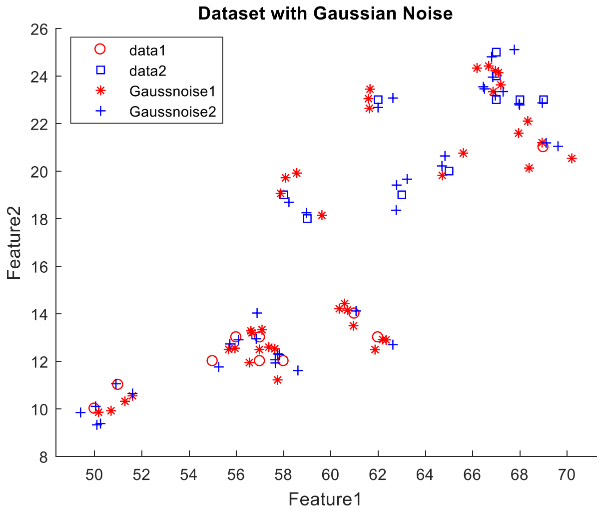

Figure 6.16: Adding attribute noise in the dataset.

The accuracy rates obtained in each test dataset as well as for each kernel are presented in **Table 6.2** to **Table 6.8**. The weight coefficient settings were set as follows: λ_1 = 0.8, λ_2 = 0.1, λ_3 = 0.1, λ_4 = 0.8, λ_5 = 0.7, kernel parameters, σ_{RBF} = 0.25, σ_{RQK} = 0.5, d_{Poly} = 2, C_{RBF} = 1, and C_{RQK} = -1. However, some datasets were represented the tuned loss by changing the C_{RBF} parameter according to the complexity of the data.

As can be observed in these tables, the performance of the new mixing kernel with the single kernel as well as the two-mixed kernels were compared. Moreover, it is clearly shown that there is an insignificant impact on the small-scale samples for the eye (**Table 6.2**) and iris (**Table 6.3**) datasets. Considering that they obtain almost the same amount of accuracy and yield lowest generalisation loss for the testing dataset.

Table 6.2: Classifiers performance on the eye dataset.

Item	RBF	RQK	POLY	RBF RQK	RBF POLY	RQK POLY	3-ConvSvm
Iteration	30	114	172	35	30	173	55
S.Vector	18	12	13	18	18	12	19
Time	0.0315	0.0282	0.0291	0.0294	0.0296	0.0290	0.0306
Training	0.9772	0.8522	0.8863	0.9772	0.9772	0.8863	0.9805
Testing							
C=1, S=0.25	1	1	1	1	1	1	1
Loss	0	0.1467	0	0	0	0	0
Outlier1	0.8809	0.9285	0.7380	0.9523	0.7857	0.8333	0.8095
Outlier2	0.8840	0.5942	0.5797	0.6956	0.6811	0.5797	0.6231
Outlier3	0.8333	0.5196	0.5098	0.5098	0.6568	0.4901	0.5392
Outlier4	0.7829	0.3875	0.4961	0.3333	0.6511	0.4186	0.4651
Outlier5	0.8395	0.2716	0.3456	0.2654	0.5432	0.3950	0.3888
Noise1	0.9375	1	0.8333	1	0.7083	0.9583	0.9583
Noise2	0.6964	0.6250	0.5952	0.4761	0.6666	0.5029	0.6130
Noise3	0.6704	0.4526	0.5511	0.4678	0.5113	0.5435	0.5246
Noise4	0.5979	0.3760	0.5070	0.4929	0.5351	0.5468	0.4242
Noise5	0.5721	0.4220	0.4540	0.4807	0.5381	0.5681	0.4355

Table 6.3: Classifiers performance on the iris dataset.

Item	RBF	RQK	POLY	RBF RQK	RBF POLY	RQK POLY	3-ConvSvm
Iteration	286	34	398	151	158	512	120
S.Vector	69	24	23	38	39	21	30
Time	0.0506	0.0438	0.0490	0.0499	0.0500	0.0463	0.0466
Training	0.9568	0.9537	0.9450	0.9762	0.9731	0.9493	0.9693
Testing							
C=1, S=0.25	1	1	1	1	1	1	1
Loss	0.0500	0.0500	0.0500	0.0500	0.0500	0.0500	0.0500
Outlier1	1	1	1	1	1	1	1
Outlier2	0.6785	0.7276	0.9107	0.8705	0.9017	0.9107	0.9151
Outlier3	0.4694	0.5461	0.7563	0.4371	0.7074	0.6612	0.7586
Outlier4	0.4131	0.2791	0.5296	0.2465	0.4814	0.3128	0.4530
Outlier5	0.4005	0.2446	0.5953	0.2993	0.4227	0.3773	0.4246
Noise1	1	0.9658	0.9658	0.9059	1	1	1
Noise2	0.6517	0.7767	0.6830	0.7187	0.7008	0.6830	0.6383
Noise3	0.5510	0.4913	0.5238	0.4397	0.5162	0.5290	0.4305
Noise4	0.5192	0.4908	0.5247	0.5041	0.5423	0.5659	0.5130
Noise5	0.5197	0.4924	0.4975	0.5196	0.4774	0.4913	0.5218

The aim of this new mixing kernels was to determine the ability of the kernel in reducing losses during testing. In addition, it was also claimed that the kernel is able to handle the future or unseen data for the correct classification purposes. Nevertheless, other factors that tend to have an impact on the kernel which include iteration, support vector, training time, and noise were also observed in this study apart from accuracy and generalisation loss.

On another note, the breast dataset (**Table 6.4**) yields high training and testing accuracy with smallest support vectors due to the adjustment of the C parameter (parameter to control misclassification) in the RBF kernel from 1 to 0.5. However, the test data had the same loss as others.

Table 6.4: Classifiers performance on the breast dataset.

Item	**RBF**	**RQK**	**POLY**	**RBF RQK**	**RBF POLY**	**RQK POLY**	**3-ConvSvm**	**3-ConvSvm (Tune Loss)**
Iteration	199	491	1778	131	145	405	148	173
S.Vector	131	102	98	103	106	99	99	**96**
Train Time	0.2284	0.2134	0.2547	0.2072	0.2068	0.2120	0.2326	0.2213
Training	0.9603	0.9707	0.9736	0.9711	0.9714	0.9732	0.9676	**0.9767**
				Testing				
C=1, S=0.25	0.9853	0.9888	0.9912	0.9855	0.9866	0.9912	0.9872	-
Loss	0.0822	0.0656	0.0334	0.0715	0.0715	0.0334	0.0715	-
C=0.5	0.9872	-	-	0.9918	0.9924	-	-	**0.9929**
Loss	0.0393	-	-	0.0393	0.0393	-	-	**0.0393**
Outlier1	0.9804	0.9181	0.9378	0.9151	0.9335	0.9461	0.9305	0.9388
Outlier2	0.9740	0.8395	0.8643	0.8695	0.8838	0.8679	0.8641	0.8618
Outlier3	0.9229	0.5674	0.6346	0.6162	0.6151	0.6301	0.6695	0.6487
Outlier4	0.8611	0.3515	0.4849	0.4137	0.4870	0.4825	0.4566	0.4752
Outlier5	0.7449	0.1981	0.3267	0.2673	0.3043	0.3490	0.3176	0.3542
Noise1	0.9582	0.9401	0.9612	0.9843	0.9349	0.9793	0.9310	0.9637
Noise2	0.8075	0.8893	0.8306	0.8491	0.8661	0.8125	0.7827	0.8248
Noise3	0.6595	0.6512	0.6856	0.6246	0.6294	0.7048	0.6079	0.6480
Noise4	0.5373	0.5729	0.5011	0.5798	0.5608	0.5932	0.5987	0.5213
Noise5	0.5098	0.5681	0.5435	0.5460	0.5279	0.5496	0.5364	0.5547

In contrast, the losses go down when the C is set to the high value (C=100) on the diabetes dataset (**Table 6.5**).

Table 6.5: Classifiers performance on the diabetes dataset.

Item	**RBF**	**RQK**	**POLY**	**RBF RQK**	**RBF POLY**	**RQK POLY**	**3-ConvSvm**	**3-ConvSvm (Tune Loss)**
Iteration	846	761	8679	1258	1806	5518	1350	**616**
S.Vector	441	432	410	427	422	411	427	462
Train Time	0.3632	0.3752	0.5618	0.3807	0.4029	0.4868	0.4250	0.3839
Training	0.7006	0.6259	0.6057	0.7508	0.7297	0.6075	0.7249	**0.7990**
				Testing				
C=1, S=0.25	0.6022	0.5808	0.6308	0.5821	0.5831	0.6308	0.6200	-
Loss	0.3062	0.3469	0.3162	0.3191	0.3191	0.3225	0.3191	-
C=100	0.6266	-	-	0.6287	0.5947	-	-	**0.6365**
Loss	0.3105	-	-	0.3056	0.3120	-	-	**0.3054**
Outlier1	0.5937	0.5732	0.6194	0.5930	0.5836	0.6237	0.6037	0.6103
Outlier2	0.6152	0.5575	0.6121	0.5556	0.5858	0.6165	0.5788	0.5868
Outlier3	0.6016	0.5257	0.5442	0.5341	0.5723	0.5382	0.5594	0.5610
Outlier4	0.6443	0.5146	0.5094	0.6108	0.5367	0.5111	0.5460	0.4998
Outlier5	0.6477	0.4667	0.4904	0.5587	0.5676	0.4309	0.5187	0.4168
Noise1	0.6055	0.4356	0.6256	0.5948	0.5922	0.6137	0.5953	0.6282
Noise2	0.5752	0.4651	0.5725	0.5226	0.5789	0.6016	0.5541	0.6019
Noise3	0.5807	0.4547	0.5541	0.5587	0.5224	0.5322	0.4695	0.5741
Noise4	0.5247	0.4815	0.5084	0.4725	0.5105	0.5283	0.4752	0.4903
Noise5	0.4786	0.4907	0.5485	0.5327	0.4863	0.5260	0.5042	0.5110

Meanwhile, the PRBF kernel shows a good loss result in the heart dataset (**Table 6.6**). A possible explanation to this might be the complexity of dataset whereby the tuning only works on the training accuracy.

Table 6.6: Classifiers performance on the heart dataset.

Item	**RBF**	**RQK**	**POLY**	**RBF RQK**	**RBF POLY**	**RQK POLY**	**3-ConvSvm**	**3-ConvSvm (Tune Loss)**
Iteration	289	961	1426	353	413	671	420	410
S.Vector	195	200	197	194	194	198	192	230
Train Time	0.1497	0.1758	0.1699	0.1658	0.1655	0.1708	0.1997	0.1817
Training	0.8719	0.6623	0.6672	0.8585	0.8578	0.6674	0.8449	**0.9835**
				Testing				
C=1, S=0.25	0.5230	0.5599	0.5403	0.5115	0.5103	0.5391	0.5046	-
Loss	0.4765	0.4101	0.4998	0.5161	0.5216	0.5142	0.5216	-
C=100	0.4683	-	-	0.5876	0.5749	-	-	0.5726
Loss	0.4419	-	-	0.4280	**0.3938**	-	-	0.4081
Outlier1	0.5151	0.5555	0.5343	0.5151	0.5101	0.5272	0.5070	0.5646
Outlier2	0.5063	0.5446	0.5000	0.5134	0.5033	0.4924	0.5016	0.5488
Outlier3	0.4877	0.5069	0.4456	0.5298	0.4448	0.4734	0.4330	0.4562
Outlier4	0.4834	0.5099	0.3815	0.5105	0.3574	0.4237	0.3483	0.3597
Outlier5	0.4849	0.4930	0.4081	0.5374	0.2681	0.3914	0.2495	0.2483
Noise1	0.5121	0.5780	0.5669	0.5223	0.4969	0.5081	0.4817	0.5638
Noise2	0.4804	0.5802	0.5570	0.5377	0.4787	0.4908	0.5519	0.5377
Noise3	0.5103	0.5266	0.5458	0.4654	0.5066	0.5623	0.4869	0.5302
Noise4	0.5403	0.5027	0.5225	0.5027	0.5199	0.5032	0.4726	0.5274
Noise5	0.4723	0.5137	0.5106	0.4793	0.4888	0.4824	0.5254	0.5017

The tuning parameter is shown to have worked well on the liver dataset (**Table 6.7**) based on the decrease of the losses instead of the accuracy.

Table 6.7: Classifiers performance on the liver dataset.

Item	**RBF**	**RQK**	**POLY**	**RBF RQK**	**RBF POLY**	**RQK POLY**	**3-ConvSvm**	**3-ConvSvm (Tune Loss)**
Iteration	353	473	540	515	716	510	671	550
S.Vector	239	247	244	241	238	243	239	**237**
Train Time	0.1857	0.1726	0.1846	0.1987	0.1791	0.1889	0.1998	0.1993
Training	0.7868	0.6407	0.6610	0.7866	0.7872	0.6609	0.7772	0.7707
				Testing				
C=1, S=0.25	0.5897	0.6172	0.5964	0.6134	0.6020	0.6001	0.6049	-
Loss	0.4055	0.4420	0.4338	0.4297	0.4055	0.4338	0.3812	-
C=0.8	0.6040	-	-	0.6125	0.6096	-	-	**0.6078**
Loss	0.4176	-	-	0.4176	0.3934	-	-	**0.3570**
Outlier1	0.5783	0.5850	0.5658	0.5800	0.5716	0.5683	0.5733	0.5658
Outlier2	0.5647	0.5413	0.5238	0.5371	0.5399	0.5308	0.5413	0.5222
Outlier3	0.5293	0.4175	0.4298	0.4122	0.4682	0.4397	0.4570	0.4466
Outlier4	0.5138	0.3335	0.4265	0.3477	0.3968	0.4234	0.3870	0.4599
Outlier5	0.5042	0.2737	0.3848	0.2676	0.3791	0.4033	0.3913	0.4613
Noise1	0.5960	0.6011	0.5952	0.5909	0.5935	0.5977	0.6292	0.5791
Noise2	0.5162	0.5434	0.5561	0.6049	0.5579	0.4825	0.5271	0.5550
Noise3	0.5318	0.5356	0.5481	0.4673	0.5078	0.5462	0.4895	0.4970
Noise4	0.5372	0.5221	0.4682	0.4942	0.4821	0.4809	0.5245	0.5684
Noise5	0.4946	0.5174	0.4958	0.5205	0.5057	0.4832	0.4880	0.5173

Nevertheless, a satisfying result managed to be obtained in the satellite dataset (**Table 6.8**). In particular, the training and testing accuracy were increased, generalisation loss was reduced, with low training time, and smallest iteration. Therefore, this further envisages that this kernel is able to work well with a large-scale sample dataset.

Table 6.8: Classifiers performance on the satellite dataset.

Item	**RBF**	**RQK**	**POLY**	**RBF RQK**	**RBF POLY**	**RQK POLY**	**3-ConvSvm**	**3-ConvSvm (Tune Loss)**
Iteration	1417	711	633	1573	1377	656	1583	**537**
S.Vector	268	299	279	247	253	288	251	321
Train Time	0.4248	0.3947	0.3882	0.3895	0.3989	0.3992	0.3959	**0.3849**
Training	0.9292	0.9182	0.9337	0.9314	0.9267	0.9334	0.9317	**0.9547**
Testing								
C=1, S=0.25	0.8976	0.9176	0.9026	0.9092	0.9023	0.9074	0.9105	-
Loss	0.1570	0.1603	0.1672	0.1672	0.1570	0.1687	0.1421	-
C=40	0.8627	-	-	0.9030	0.8971	-	-	**0.9125**
Loss	0.1645	-	-	0.1450	0.1430	-	-	**0.1323**
Outlier1	0.6762	0.7403	0.7333	0.6975	0.7010	0.7345	0.7121	0.7234
Outlier2	0.6607	0.7623	0.7247	0.6453	0.7104	0.7419	0.7229	0.7211
Outlier3	0.6471	0.7845	0.7111	0.5945	0.7159	0.7373	0.7487	0.6999
Outlier4	0.5367	0.7600	0.5089	0.3363	0.7045	0.5889	0.7420	0.5955
Outlier5	0.5033	0.7470	0.4434	0.2751	0.6720	0.5615	0.7343	0.5749
Noise1	0.6704	0.7362	0.7234	0.6955	0.6958	0.7240	0.6885	0.7103
Noise2	0.6258	0.6963	0.6764	0.6525	0.6504	0.6917	0.6678	0.6351
Noise3	0.5915	0.5808	0.5910	0.6187	0.5848	0.5933	0.6115	0.5659
Noise4	0.4930	0.5356	0.5184	0.5014	0.5043	0.5116	0.4877	0.5665
Noise5	0.4757	0.4883	0.4959	0.4845	0.4930	0.4953	0.4829	0.5643

Hence, the generalisation ability [129] was tested to ensure a complete analysis of the 3-ConvSvm performance. The heart dataset was selected as a training samples with the previous weight setting. **Figure 6.17** shows data distribution of the heart dataset as a training model, while iris as the test datasets. Next, the other datasets were used as test samples by depending on only one set of parameters model (heart dataset) for training.

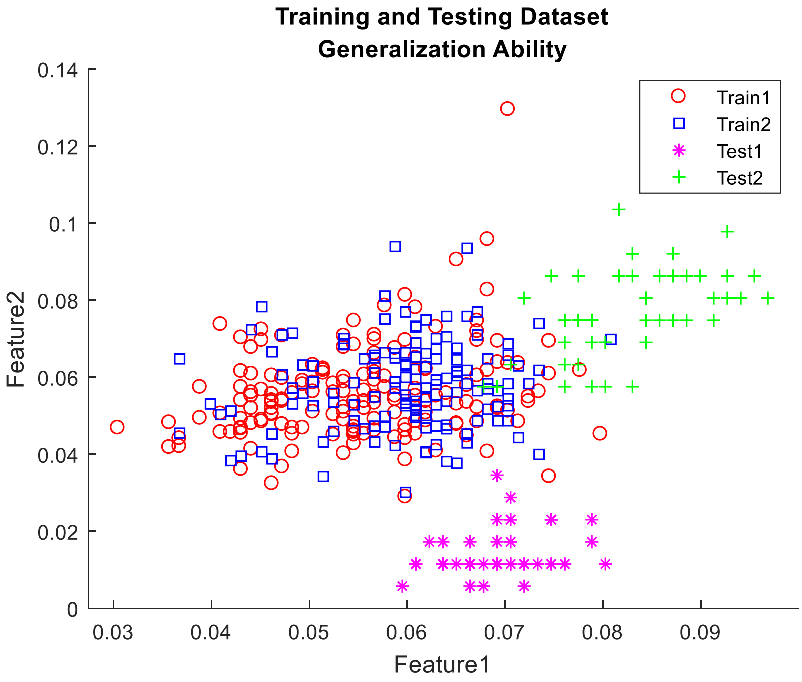

Figure 6.17: Samples distribution of heart dataset as training and iris dataset for testing.

As can be observed in **Table 6.9**, the performance of the new kernel is quite similar with the individuals testing. More importantly diabetes and satellite datasets show better results. Therefore, these results can be considered as an empirically proof of the good generalisation ability.

Table 6.9: Generalisation ability.

Datasets	Accuracy (Group)	Accuracy (Individual)
Training (C=100, S=0.25)		
Heart	0.9845	
Testing		
Eye	0.8506	1
Iris	1	1
Liver	0.5862	0.6049
Breast	0.9481	0.9872
Diabetes	**0.6409**	0.6200
Satellite	**0.9181**	0.9105

Overall, results showed in Table 6.2, 6.3, 6.4, 6.5, 6.6, 6.7, and 6.8 represent datasets of eye, iris, breast, diabetes, heart, liver, and satellite respectively. Seven types of classifiers were compared, and seven attributes were computed to measure the performance of proposed kernel. It is certain that type of kernel used in the SVM affecting the classification accuracy. The complexity of dataset also contributes to the classifier efficiency. Based on the accuracy on the testing dataset, both of eye and iris datasets have shown best accuracy seems the data distribution is less complex.

The setting of parameters was tuned when dataset become more complex as shown in the breast, diabetes, heart, liver, and satellite. Among seven classifiers, it appears that heart dataset has highest complexity based on the lowest accuracy at 0.5726. Therefore, the parameter setting in kernel should change according to the complexity of dataset. The proposed kernel showed has best accuracy on the eye, iris, breast, diabetes, and satellite datasets compared with RBF kernel. Whereas, third best accuracy on the heart and liver datasets.

In addition, accuracy is the preferable measure to study kernel performance with noise. This study is very useful for real-world application that may contain implicit and explicit data processing errors. The proposed kernel showed low accuracy when noise level is increased on the most of datasets. It suggests that the proposed kernel is more sensitive to the noise compared with RBF kernel. Furthermore, the time consumed during the training was similar with others classifiers or sometimes even better despite the fact that the proposed kernel is comprised of more than two kernels.

6.4 Summary

A mixing kernel for SVM classifier has been proposed in this chapter. The model adopts the convex combination on the coefficient weights of a combined kernels in order to solve a non-linear binary classification problem. Moreover, three standard kernels, namely RBF, polynomial, and RQK were combined because they were believed to provide more learning flexibility due to the various parameters setting. The main objective was to reduce the generalisation loss for testing samples, which further envisages that the new kernel is able to work well on the future or unseen dataset.

Apart from that, several numerical experiments were performed on seven different sizes and types of datasets. The purpose of the current experiment was to compare the proposed kernel with the single and 2-convex kernel. In addition, the numerical experiments showed that the new kernel are able to perform similarly and sometimes even better than the standard kernels (RBF, polynomial, RQK). Finally, the performance of 3-ConvSvm obtained in the generalisation error managed to satisfy some of the test problems.

CHAPTER 7

CONCLUSIONS AND FURTHER WORKS

The uniqueness of the cornea with five-layer tissues underneath lies mainly in its transparency. This property poses a huge challenge to clinicians due to the changes that are often fine and subtle, thus serving as a barrier for diagnosis. Over the years, the state of the art in eye diagnostics depends on the optical investigation and diagnosis that are conducted based on medical expert's insights and deep knowledge. Therefore, hyperspectral imaging is described as a new method that has the potential to change the pure human-optical method to a digitally supported optical method.

The image acquired from hyperspectral imaging are capable of producing better result in assessing corneal epithelium injury. In addition, the combination of spatial and spectral features was revealed to be particularly useful in gathering clinical information. Moreover, the different approaches can be employed to identify injury on the images due to the transparent nature of the cornea, with and without fluorescein staining.

On a more important note, the combination of hyperspectral imaging and image processing techniques has the potential to become a viable alternative solution in assessing corneal epithelium injury without having to conduct the traditional contacting methods. Hence, this will not only lead to new insights in eye diagnostics because there is a high possibility that the new approach will affect daily clinical practice, especially in terms of injury assessment processes, eye treatment, and the perspective on the field of eye care on the long run. In this thesis, the three main contributions have been presented and discussed in Chapters 4, 5, and 6.

This chapter draws a number of conclusions about the work that has been presented. The chapter concludes by providing a number of suggestions for future work that may be carried out as a result of the finding in this thesis.

7.1 The 8-SHIE

Following the literature review that was provided in Chapter 2, and the background notions that were presented in Chapter 3, the discussion in Chapter 4 focused on image enhancement based on the hyperspectral images. The preliminary study managed to show the similarity between the reflectance signatures that are retrieved from hyperspectral imaging of both normal and abnormal corneal epithelium tissues of porcine with subtle variances. Hence, this provides confidence to pursue the data collected for further image analyses. Moreover, a total of 25 new hyperspectral data were collected to develop a new image enhancement algorithm in this particular study.

Perhaps the most significant contribution of this thesis is the new image enhancement was presented in Chapter 4. This new image enhancement carried out to differentiate the injured and healthy corneas. As such, the proposed enhancement is known as an 8-Step Hyperspectral Image Enhancement (8-SHIE). Hyperspectral image enhancement had been explored in previous study for the purpose of providing high accuracy in image classification [97]. The steps involved were image pre-processing and image enhancement, as described in Chapter 3, had been performed to improvise distinction and visualisation of both normal and abnormal corneal epithelium.

The results showed that the proposed algorithm is able to clearly illustrate the injured boundary. Apart from that, the algorithm can also be used to monitor the cornea healing process considering that the injured boundary can be viewed from band-to-band. Primarily, this algorithm is designed for cornea images that were gathered for the purpose of this thesis. Hence, this algorithm was further tested on the existing remote-sensing Indian Pines dataset in order to ascertain that it can work well with other hyperspectral images. In the case of this experiment, several parameters were altered to suit the image properties. According to the reflectance signature results, this algorithm is able to discriminates the ten varying classes despite its main purpose of distinguishing only the two classes.

The limitation of this proposed algorithm is on the processing steps. From eight steps that apply for medical application, it become seven steps by eliminates the step-2 when automatic image crop is irrelevant. The parameter setting in step-5 need to change in the morphology process for the structuring element type and size. For example, in medical application 'ball' type is appropriate on the cornea image, whereas 'disk' type is more suitable for satellite image, as shown in this study.

7.2 Mixture Deep-Learning Classification

Image classification is described as the process of labelling predetermined pixels into different classes. Commonly, the purpose of classification in medical application is to classify healthy and unhealthy tissues for the purpose of analysing and diagnosing specific diseases.

Chapter 5 was described and compared the three classification approaches with the purpose of figuring out the best accuracy and low time consumption for the cornea assessment. The three classification approaches were:

1. Histogram feature extraction with SVM-GRBF classifier.
2. Transfer learning using pretrained AlexNet with a fine-tuned model.
3. Feature extraction with pretrained AlexNet (Mixture AlexNet and SVM-Linear).

In this research we adopted feature extraction using a histogram [105] and a deep learning structure made by Alex Krizhevsky (AlexNet), the champion of ImageNet Large Scale Visual Recognition Challenge (ILSVRC2010) as a reference [85].

Recent advances in deep learning made tasks such as image and speech recognition possible. Deep learning is a subset of machine learning algorithms that is very good at recognizing patterns but typically requires a large number of data [130]. Deep learning excels in recognizing objects in images because it is implemented using three or more layers of artificial neural networks whereby each layer is responsible for extracting one or more features of the image.

Overall, it can be concluded that the mixture deep learning AlexNet-SVM is the most suitable technique that can be used for cornea assessment among the three classification approaches based on the accuracy and time consumption. The algorithm proposed which involves the use of optimal classifier can be used for objective measurement (image quantification) in order to help the clinician to identify normal and abnormal tissues automatically.

7.3 The 3-ConvSvm

The experiments that were carried out to produce the results that concluded Chapter 6 highlighted the fact that the SVM classifier was inefficient when implemented using single kernel. A considerable amount of research indicated that combined kernels are able to produce improved classification accuracy compared to the use of a single kernel [116], [117], [118], [119], [120]. As a result, a mixing kernel was needed to make the SVM reduce the generalisation loss.

It is important to realize that real-world data such as images and video are usually complex, redundant, and highly variable. One of the drawbacks in designing a new kernel for the SVM classifier refers to the concern that they cannot be generalised well. Therefore, this has motivated the design of the proposed mixing kernel (3-ConvSvm). More importantly, the modify existing functions with the aim of making new ones are deemed possible provided that the kernel is valid and the combination is admissible [114], [83].

The new model used 3-convex combination on the coefficient weights of a combined kernel has been designed to solve a non-linear binary classification problem. Three standard kernels, namely RBF, polynomial, and RQK were combined in order to provide more learning flexibility due to the various parameter’s settings. The objective was to reduce the generalisation loss for testing samples, which envisages that the new kernel is able to work well with future or unseen dataset. Apart from that, numerical experiments showed that the new kernel has a similar performance or sometimes even better than the standard kernel (RBF, polynomial, RQK).

Overall, it can be concluded that the performance of 3-ConvSvm obtained in generalisation error is able to solve some of the test problems by tuned only one parameter known as C. This proposed kernel has limitation where the kernel parameters need to be setting appropriately based on how complex the dataset is. There are two main parameters are important in order to obtain optimum classification i.e., C parameter (regularization parameter to reduce misclassification) and gamma parameter (defines the support vector).

7.4 Further Works

There are a number of areas that could be developed in order to build upon and extend the ideas and techniques that have been presented in this thesis. First, it is clearly that the input image tested in the new image enhancement (8-SHIE) was porcine eyes were dead tissue. Where the porcine eyes are readily accessible and inexpensive. This could provide a number of advantages if the 8-SHIE could be tested on the live tissue or a best is on to human cornea.

Future works are also recommended to investigate different types of corneal disorder using HSI technique. In this study focuses only on one type of injury i.e., corneal abrasion. The system could be more robust if different size and pattern of injuries are collected. Other than corneal abrasion, different type of injury such as impacts to the eye, foreign bodies, penetrating injuries, chemical burns, and radiation exposure that are produced various effect and shape of injuries on the corneal. It might be more splendid if HSI can capture more details into the cornea for early detection of damage from bacteria that caused to the corneal keratitis. Other than that, corneal disorder such as dry eye where the eyes produce lower quality tears, and corneal dystrophies when corneal lose normal clarity, that commonly undetectable in the early stage. Because, early diagnosis is able to cut treatment costs.

Referring to the mixture deep-learning classification, to the author’s knowledge when submitting this thesis, there was no similar dataset available that could be compared to the method proposed in this thesis for the classification performance. As a result, the classification performance was compared with three different approaches as described in the Chapter 5.

In the future, the proposed method would perhaps be interesting applied to other similar large datasets. By having a large dataset, the neural network can be trained with various injuries pattern and size, as well as with corneal disorder characteristics, such as corneal opacities. This is important for ensure the real-time corneal detection is success with minimum error.

The applications of the 3-ConvSvm have so far focused on the analysis of 2-dimensional image features for binary classification. The standard SVM classifier has been used in a large number of applications involved with multiclass model. Multiclass model could understand more detailed features of each image compare to binary class model. It would be interesting to investigate the improvement in the robustness that is offered in the multiclass model when using the 3-ConvSvm that has been introduced in this thesis.

Multiclass model classification is representing the real-time application where the inputs can be classified as one of many outputs. For example, in binary, system only classify injuries and healthy cornea, in multiclass model, the system can classify type of injuries and the size of injuries such as small, average, or large for corneal abrasion. In addition, the pattern of chemical burn severity could be identified by train the classifier on the first, second, and third-degree burns. The multiclass classification is allowing the model to learn more features and the systems become more intelligent and robust.

Finally, as awareness of the steps involved to the new technology that related to the internet of things (IoT), the proposed algorithm is suggested to be integrated with hyperspectral camera as a mobile application hardware and software. This mobile apps can lead to a greater efficiency in cornea assessment without hassle and make every single task easier.

REFERENCES

1. WHO Visual impairment and blindness. *World Heal. Organ.* 2014.

2. Robaei, D.; Watson, S. Corneal blindness: a global problem. *Clin. Experiment. Ophthalmol.* **2014**, *42*, 213–214, doi:10.1111/ceo.12330.

3. Goetz, A. F. H.; Vane, G.; Solomon, J. E.; Rock, B. N. Imaging spectrometry for Earth remote sensing. *Science* **1985**, *228*, 1147–1153, doi:10.1126/science.228.4704.1147.

4. Hege, E. K.; O'Connell, D.; Johnson, W.; Basty, S.; Dereniak, E. L. Hyperspectral imaging for astronomy and space surveillance. *Opt. Sci. Technol. SPIE's 48th Annu. Meet.* **2004**, *5159*, 380–391, doi:10.1117/12.506426.

5. Huang, H.; Liu, L.; Ngadi, M. O. Recent developments in hyperspectral imaging for assessment of food quality and safety. *Sensors (Basel).* **2014**, *14*, 7248–7276, doi:10.3390/s140407248.

6. García-Allende, P. B.; Conde, O. M.; Mirapeix, J. M.; Cobo, A.; Lopez-Higuera, J. M. Hyperspectral imaging sustains competitiveness. *SPIE Newsroom* **2010**, 2–5, doi:10.1117/2.1201003.002681.

7. Marshall, S.; Kelman, T.; Qiao, T.; Murray, P.; Zabalza, J. Hyperspectral Imaging for Food Applications. In *2015 23rd European Signal Processing Conference (EUSIPCO)*; 2015; pp. 2854–2858.

8. ElMasry, G.; Sun, D. W. *Principles of Hyperspectral Imaging Technology*; 2010; ISBN 9780123747532.

9. Polder, G.; Van Der Heijden, G. W. a. M.; Young, I. T. Spectral Image Analysis for Measuring Ripeness of Tomatoes. *Trans. ASAE* **2002**, *45*, 1155–1161, doi:10.13031/2013.9924.

10. Liang, H. Advances in multispectral and hyperspectral imaging for archaeology and art conservation. *Appl. Phys. A Mater. Sci. Process.* **2012**, *106*, 309–323, doi:10.1007/s00339-011-6689-1.

11. Fabelo, H.; Ortega, S.; Kabwama, S.; Callico, G. M.; Bulters, D.; Szolna, A.; Pineiro, J. F.; Sarmiento, R. HELICoiD project: a new use of hyperspectral imaging for brain cancer detection in real-time during neurosurgical operations. In *Proc. SPIE 9860, Hyperspectral Imaging Sensors: Innovative Applications and Sensor Standards , May 10, 2016*; 2016; Vol. 986002.

12. Calin, M. A.; Parasca, S. V; Savastru, R.; Manea, D. Characterization of burns using hyperspectral imaging technique - A preliminary study. *Burns* **2014**, *41*, 118–124, doi:10.1016/j.burns.2014.05.002.

13. Regeling, B.; Thies, B.; Gerstner, A. O. H.; Westermann, S.; Müller, N. A.; Bendix, J.; Laffers, W. Hyperspectral Imaging Using Flexible Endoscopy for Laryngeal Cancer Detection. *Sensors* **2016**, *16*, 1288, doi:10.3390/s16081288.

14. Kumashiro, R.; Konishi, K.; Chiba, T.; Akahoshi, T.; Nakamura, S.; Murata, M.; Tomikawa, M.; Matsumoto, T.; Maehara, Y.; Hashizume, M. An integrated endoscopic system based on optical imaging and hyper spectral data analysis for colorectal cancer detection. *Anticancer Res.* **2016**, *3932*, 3925–3932.

15. Zakian, C.; Pretty, I.; Ellwood, R. Near-infrared hyperspectral imaging of teeth for dental caries detection. *J. Biomed. Opt.* **2009**, *14*, 064047, doi:10.1117/1.3275480.

16. Kirwan, R. P.; Zheng, Y.; Tey, A.; Anijeet, D.; Sueke, H.; Kaye, S. B. Quantifying Changes in Corneal Neovascularization Using Fluorescein and Indocyanine Green Angiography. *Am. J. Ophthalmol.* **2012**, *154*, 850–858.e2, doi:10.1016/j.ajo.2012.04.021.

17. Jester, J. V.; Li, H. F.; Petroll, W. M.; Parker, R. D.; Cavanagh, H. D.; Carr, G. J.; Smith, B.; Maurer, J. K. Area and depth of surfactant-induced corneal injury correlates with cell death. *Investig. Ophthalmol. Vis. Sci.* **1998**, *39*, 922–936.

18. Kaluzny, B. J.; Kałuzny, J. J.; Szkulmowska, A.; Gorczyńska, I.; Szkulmowski, M.; Bajraszewski, T.; Wojtkowski, M.; Targowski, P. Spectral optical coherence tomography: a novel technique for cornea imaging. *Cornea* **2006**, *25*, 960–965, doi:10.1097/01.ico.0000224644.81719.59.

19. Grulkowski, I.; Gora, M.; Szkulmowski, M.; Gorczynska, I.; Szlag, D.; Marcos, S.; Kowalczyk, A.; Wojtkowski, M. Anterior segment imaging with Spectral OCT system using a high-speed CMOS camera. *Opt. Express* **2009**, *17*, 4842–4858, doi:10.1364/OE.17.004842.

20. Morgan, P. B.; Maldonado-Codina, C. Corneal staining: Do we really understand what we are seeing? *Contact Lens Anterior Eye* **2009**, *32*, 48–54, doi:10.1016/j.clae.2008.09.004.

21. Efron, N. Contact Lens Complications:Corneal Staining. In *Chapter 16, Corneal Epithelium, page:155-166*; Elsevier Ltd, 2012; p. 350 ISBN 0702042692.

22. Ruberti, J. W.; Roy, A. S.; Roberts, C. J. Corneal biomechanics and biomaterials. *Annu. Rev. Biomed. Eng.* **2011**, *13*, 269–295, doi:10.1146/annurev-bioeng-070909-105243.

23. Jonas, T.; Memorial, S. F.; Dohlman, C. H. The function of the corneal epithelium in health and disease. *Invest. Ophthalmol.* **1971**, *10*, 383–407.

24. Steele, C. Corneal wound healing: a review. *Optom. Today* **1999**, 28–32.

25. Hassan, K. M.; Ali, S.; Waris, N.; Swamiraj, S. V; Hussain, S. A. Ocular injury pattern in the university hospital of South India. **2017**, *3*, 234–238,

doi:10.18231/2395-1451.2017.0058.

26. Jacobs, D. S. Diagnosis and Treatment of Ocular Pain: the Ophthalmologist's Perspective. *Curr. Ophthalmol. Rep.* **2017**, *5*, 271–275, doi:10.1007/s40135-017-0152-1.

27. Timoney, P. J.; Breathnach, C. S. I. J. Allvar Gullstrand and the slit lamp 1911. *Ir. J. Med. Sci.* **2013**, doi:doi:10.1007/s11845-012-0873-y.

28. McCarey, B. E.; Edelhauser, H. F.; Lynn, M. J. Review of Corneal Endothelial Specular Microscopy for FDA Clinical Trials of Refractive Procedures, Surgical Devices, and New Intraocular Drugs and Solutions. *Cornea* **2008**, *27*, 1–16, doi:10.1097/ICO.0b013e31815892da.

29. Rio-Cristobal, A.; Martin, R. Corneal assessment technologies: Current status. *Surv. Ophthalmol.* **2014**, *59*, 599–614, doi:10.1016/j.survophthal.2014.05.001.

30. Belin, M. W.; Khachikian, S. S.; McGhee, C. N. J.; Patel, D. New Technology in Corneal Imaging. *Int. Ophthalmol. Clin.* **2010**, *50*, 177–189, doi:10.1097/IIO.0b013e3181e20ac0.

31. Jain, R.; Grewal, S. P. S. Pentacam : Principle and Clinical Applications. *J. Curr. Glaucoma Pract.* **2009**, 20–32.

32. Govender, M.; Chetty, K.; Bulcock, H. A review of hyperspectral remote sensing and its application in vegetation and water resource studies. *waters Water SA* **2007**, *33*, 145–151, doi:10.4314/wsa.v33i2.49049.

33. Adam, E.; Mutanga, O.; Rugege, D. Multispectral and hyperspectral remote sensing for identification and mapping of wetland vegetation: A review. *Wetl. Ecol. Manag.* **2010**, *18*, 281–296, doi:10.1007/s11273-009-9169-z.

34. van der Meer, F. D.; van der Werff, H. M. A.; van Ruitenbeek, F. J. A.; Hecker, C. A.; Bakker, W. H.; Noomen, M. F.; van der Meijde, M.; Carranza, E. J. M.; de Smeth, J. B.; Woldai, T. Multi- and hyperspectral geologic remote sensing: A review. *Int. J. Appl. Earth Obs. Geoinf.* **2012**, *14*, 112–128, doi:10.1016/j.jag.2011.08.002.

35. Underwood, E.; Ustin, S. L.; DiPietro, D. Mapping nonnative plants using hyperspectral imagery. *Remote Sens. Environ.* **2003**, *86*, 150–161, doi:10.1016/S0034-4257(03)00096-8.

36. Sun, D. W. *Hyperspectral Imaging for Food Quality Analysis and Control*; Elsevier Inc.: Oxford, UK, 2010; ISBN 978-0-12-373642-0.

37. Polak, A.; Kelman, T.; Murray, P.; Marshall, S.; Stothard, D. J. M.; Eastaugh, N.; Eastaugh, F. Hyperspectral imaging combined with data classification techniques as an aid for artwork authentication. *J. Cult. Herit.* **2017**, *26*, 1–11, doi:10.1016/j.culher.2017.01.013.

38. Geladi, P. L. M.; Grahn, H. F.; Burger, J. E. Multivariate Images, Hyperspectral Imaging: Background and Equipment. *Tech. Appl. Hyperspectral Image Anal.* **2007**, 1–15, doi:10.1002/9780470010884.ch1.

39. Li, Q.; He, X.; Wang, Y.; Liu, H.; Xu, D.; Guo, F. Review of spectral imaging technology in biomedical engineering: achievements and challenges. *J. Biomed. Opt.* **2013**, *18*, 100901, doi:10.1117/1.JBO.18.10.100901.

40. Smith, R. B. Introduction to Remote Sensing of Environment. *www.microimages.com* **2001**.

41. Qin, J.; Kim, M.; Chao, K.; Chan, D.; Delwiche, S.; Cho, B.-K. Line-Scan Hyperspectral Imaging Techniques for Food Safety and Quality Applications. *Appl. Sci.* **2017**, *7*, 125, doi:10.3390/app7020125.

42. Sawyer, T. W.; Luthman, A. S.; Bohndiek, S. E. Evaluation of illumination system uniformity for wide-field biomedical hyperspectral imaging. *J. Opt. (United Kingdom)* **2017**, *19*, doi:10.1088/2040-8986/aa6176.

43. Islam, K.; Ploschner, M.; Goldys, E. M. Multi-LED light source for hyperspectral imaging. *Opt. Express* **2017**, *25*, 32659, doi:10.1364/OE.25.032659.

44. Nielsen, O. H. A.; Dahl, A. L.; Larsen, R.; Møller, F.; Nielsen, F. D.; Thomsen, C. L.; Aanæs, H.; Carstensen, J. M. Supercontinuum light sources for hyperspectral subsurface laser scattering: Applications for food inspection. *Lect. Notes Comput. Sci. (including Subser. Lect. Notes Artif. Intell. Lect. Notes Bioinformatics)* **2011**, *6688 LNCS*, 327–337, doi:10.1007/978-3-642-21227-7_31.

45. Manea, D.; Calin, M. A. Hyperspectral imaging in different light conditions. *Imaging Sci. J.* **2015**, *63*, 214–219, doi:10.1179/1743131X15Y.0000000001.

46. Katrašnik, J.; Pernuš, F.; Likar, B.; Górski, K. M.; Hivon, E.; Banday, A. J.; Wandelt, B. D.; Hansen, F. K.; Reinecke, M.; Bartelmann, M. A method for characterizing illumination systems for hyperspectral imaging. *Opt. EXPRESS 4841 Intell. Lab* **2013**, *21*, 209–217, doi:10.1364/OE.21.004841.

47. Grant, J.; Kenney, M.; Shah, Y. D.; Escorcia-Carranza, I.; Cumming, D. R. S. CMOS compatible metamaterial absorbers for hyperspectral medium wave infrared imaging and sensing applications. *Opt. Express* **2018**, *26*, 10408, doi:10.1364/OE.26.010408.

48. Lu, G.; Fei, B. Medical hyperspectral imaging: a review. *J. Biomed. Opt.* **2014**, *19*, 10901, doi:10.1117/1.JBO.19.1.010901.

49. Schaare, P. N.; Fraser, D. G. Comparison of reflectance, interactance and transmission modes of visible-near infrared spectroscopy for measuring internal properties of kiwifruit (Actinidia chinensis). *Postharvest Biol. Technol.* **2000**, *20*, 175–184, doi:10.1016/S0925-5214(00)00130-7.

50. Noor, S. S. M.; Michael, K.; Marshall, S.; Ren, J.; Tschannerl, J.; Kao, F. J. The properties of the cornea based on hyperspectral imaging: Optical biomedical engineering perspective. *Int. Conf. Syst. Signals, Image Process.* **2016**, *2016–June*, 4–7, doi:10.1109/IWSSIP.2016.7502710.

51. Ding, H.; Chang, R. C. Comparison of photometric stereo and spectral analysis for visualization and assessment of burn injury from hyperspectral imaging. In *2015 IEEE International Conference on Computational Intelligence and Virtual Environments for Measurement Systems and Applications, CIVEMSA 2015*; 2015.

52. Tetschke, F.; Markgraf, W.; Gransow, M.; Koch, S.; Thiele, C.; Kulcke, A.; Malberg, H. Hyperspectral imaging for monitoring oxygen saturation levels during normothermic kidney perfusion. *J. Sensors Sens. Syst.* **2016**, *5*, 313–318, doi:10.5194/jsss-5-313-2016.

53. Khoobehi, B.; Beach, J. M.; Kawano, H. Hyperspectral Imaging for Measurement of Oxygen Saturation in the Optic Nerve Head. *Invest. Ophthalmol. Vis. Sci.* **2004**, *45*, 1464–72, doi:10.1167/iovs.03-1069.

54. Mordant, D. J.; Al-Abboud, I.; Muyo, G.; Gorman, a; Sallam, a; Ritchie, P.; Harvey, a R.; McNaught, a I. Spectral imaging of the retina. *Eye (Lond).* **2011**, *25*, 309–320, doi:10.1038/eye.2010.222.

55. Li, Q.; Xue, Y.; Xiao, G.; Zhang, J. New microscopic pushbroom hyperspectral imaging system for application in diabetic retinopathy research. *J. Biomed. Opt.* **2007**, *12(6),0640*, doi:ISSN: 1083-3668.

56. Desjardins, M.; Sylvestre, J. P.; Jafari, R.; Kulasekara, S.; Rose, K.; Trussart, R.; Arbour, J. D.; Hudson, C.; Lesage, F. Preliminary investigation of multispectral retinal tissue oximetry mapping using a hyperspectral retinal camera. *Exp. Eye Res.* **2016**, *146*, 330–340, doi:10.1016/j.exer.2016.04.001.

57. Li, H.; Liu, W.; Dong, B.; Kaluzny, J. V.; Fawzi, A. A.; Zhang, H. F. Snapshot hyperspectral retinal imaging using compact spectral resolving detector array. *J. Biophotonics* **2017**, *10*, 830–839, doi:10.1002/jbio.201600053.

58. Dontu, S.; Miclos, S.; Savastru, D.; Tautan, M. Combined spectral-domain optical coherence tomography and hyperspectral imaging applied for tissue analysis: Preliminary results. *Appl. Surf. Sci.* **2017**, *417*, 119–123, doi:10.1016/j.apsusc.2017.03.175.

59. Mahapatra, D.; Bozorgtabar, B. Retinal Vasculature Segmentation Using Local Saliency Maps and Generative Adversarial Networks For Image Super Resolution. **2017**, 118–125, doi:10.1007/978-3-319-66185-8.

60. Reynaud, J.; Beuerman, R. W.; Khoobehi, B.; Beach, J.; Lanoue, M.; Schwarz, M.; Galloway-Dawkins, R. Confocal Hyperspectral Imaging of the Cornea. *Invest. Ophthalmol. Vis. Sci.* **2003**, *44(13):360.*

61. Press, D. Quantitative evaluation of corneal epithelial injury caused by n-heptanol using a corneal resistance measuring device in vivo. **2012**, 585–593.

62. Qin, J. Hyperspectral Imaging Instruments. In *Hyperspectral Imaging for Food Quality Analysis and Control*; Elsevier, 2010; pp. 129–172 ISBN 9780123747532.

63. Elsheikh, A.; Alhasso, D.; Rama, P. Biomechanical properties of human and porcine corneas. *Exp. Eye Res.* **2008**, *86*, 783–790, doi:10.1016/j.exer.2008.02.006.

64. Lee, G. A.; Chiang, M. Y. M.; Shah, P. Pig eye trabeculectomy - A wet-lab teaching model. *Eye* **2006**, *20*, 32–37, doi:10.1038/sj.eye.6701784.

65. Isaac, B. *Handbook of Medical Image Processing and Analysis*; Second.; Elsevier Inc.: Oxford, UK, 2009; ISBN 978-0-12-373904-9.

66. Gonzalez, W. *Digital Image Processing*; Third.; Pearson Prentice Hall: Upper Saddle River,New Jersey, 2008;

67. Dong, B.; Yang, J.; Hao, S.; Zhang, X. Research on an Improved Medical Image Enhancement Algorithm Based on P-M Model. *Open Biomed. Eng. J.* **2015**, *0*, 209–213.

68. Irgenfried, S.; Hock, J. Acquisition and storage of multispectral material signatures. In *2nd International Conference on Optical Characterization of Material*; Karlsruhe, Germany, 2015; pp. 123–135.

69. Lounnaci, K.; Idlahcen, S.; Sedarsky, D.; Roze, C.; Blaisot, J.-B.; Demoulin, F.-X. Image Processing Techniques for Velocity, Interface Complexity, and Droplet Production Measurement in the Near-Nozzle Region of a Diesel Spray. *At. Sprays* **2015**, *25*, 753–775, doi:10.1615/atomizspr.2015011054.

70. Chazette, L.; Becker, M.; Szczerbicka, H. Basic algorithms for bee hive monitoring and laser-based mite control. *2016 IEEE Symp. Ser. Comput. Intell. SSCI 2016* **2017**, doi:10.1109/SSCI.2016.7850001.

71. Adams, R. Radial Decomposition of Disks and Spheres. *CVGIP Graph. Model. Image Process.* **1993**, *55*, 325–332, doi:10.1006/cgip.1993.1024.

72. Sternberg, S. R. Grayscale morphology. *Comput. Vision, Graph. Image Process.* **1986**, *35*, 333–355, doi:10.1016/0734-189X(86)90004-6.

73. Verma, R.; Mehrotra, R.; Bhateja, V. An Improved Algorithm for Noise Suppression and Baseline Correction of ECG Signals. In *Advances in Intelligent Systems and Computing*; 2013; Vol. 327, pp. 733–739 ISBN 9783319119328.

74. Firoz, R.; Ali, M. S.; Khan, M. N. U.; Hossain, M. K.; Islam, M. K.; Shahinuzzaman, M. Medical Image Enhancement Using Morphological Transformation. *J. Data Anal. Inf. Process.* **2016**, *04*, 1–12,

doi:10.4236/jdaip.2016.41001.

75. Marr, B. Y. D. Theory of edge detection. *Proc. R. Soc. B* **1980**, *217*, 187–217.

76. Mallick, A.; Roy, S.; Chaudhuri, S. S.; Roy, S. Optimization of Laplace of Gaussian (LoG) filter for enhanced edge detection: A new approach. *Int. Conf. Control. Instrumentation, Energy Commun. CIEC 2014* **2014**, *2*, 658–661, doi:10.1109/CIEC.2014.6959172.

77. Eid, M.; Abougabal, A. Subtraction images: A really helpful tool in non-vascular MRI. *Egypt. J. Radiol. Nucl. Med.* **2014**, *45*, 909–919, doi:10.1016/j.ejrnm.2014.04.013.

78. Juan, A. De; Ferrer, A. Multivariate image analysis: A review with applications. *Chemom. Intell. Lab. Syst.* **2011**, *107*, 1–23, doi:10.1016/j.chemolab.2011.03.002.

79. Rodarmel, C.; Shan, J. Principal Component Analysis for Hyperspectral Image Classification. *Surv. L. Inf. Syst.* **2002**, *62*, 115–123, doi:10.1109/IGARSS.2001.976068.

80. Zabalza, J.; Ren, J.; Zheng, J.; Han, J.; Zhao, H.; Li, S.; Marshall, S. Novel Two-Dimensional Singular Spectrum Analysis for Effective Feature Extraction and Data Classification in Hyperspectral Imaging. *Geosci. Remote Sensing, IEEE Trans.* **2015**, *53*, 4418–4433.

81. Zabalza, J.; Ren, J.; Ren, J.; Liu, Z.; Marshall, S. Structured covariance principal component analysis for real-time onsite feature extraction and dimensionality reduction in hyperspectral imaging. *Appl. Opt. 53 (20), 4440-4449* **2014**, *53*, 4440–4449.

82. Zabalza, J.; Ren, J.; Yang, M.; Zhang, Y.; Wang, J.; Marshall, S.; Han, J. Novel Folded-PCA for improved feature extraction and data reduction with hyperspectral imaging and SAR in remote sensing. *ISPRS J. Photogramm. Remote Sens.* **2014**, *93*, 112–122, doi:10.1016/j.isprsjprs.2014.04.006.

83. Rasmussen, C. E.; Williams, C. K. I. *Gaussian Processes for Machine Learning*; Massachusetts Institute of Technology, 2006;

84. Melgani, F.; Bruzzone, L. Classification of Hyperspectral Remote Sensing. *IEEE Trans. Geosci. Remote Sens.* **2004**, *42*, 1778–1790.

85. Krizhevsky, A.; Sutskever, I.; Hinton, G. ImageNet Classification with Deep Convolutional Neural Networks. In *Advances in Neural Information Processing Systems 25*; 2012; pp. 1097–1105.

86. Nogueira, R. F.; de Alencar Lotufo, R.; Machado, R. C. Fingerprint Liveness Detection using Convolutional Networks. *Ieee Trans. Inf. Forensics Secur.* **2016**, *11*, 1206–1213, doi:10.1109/TIFS.2016.2520880.

87. Oquab, M.; Bottou, L.; Laptev, I.; Sivic, J. Learning and Transferring Mid-Level Image Representations using Convolutional Neural Networks. *IEEE Conf. Comput. Vis. Pattern Recognit.* **2014**, 1717–1724, doi:10.1109/CVPR.2014.222.

88. Chen, Y.; Jiang, H.; Li, C.; Jia, X.; Ghamisi, P. Deep Feature Extraction and Classification of Hyperspectral Images Based on Convolutional Neural Networks. *IEEE Trans. Geosci. Remote Sens.* **2016**, *54*, 6232–6251, doi:10.1109/TGRS.2016.2584107.

89. Elleuch, M.; Maalej, R.; Kherallah, M. A New design based-SVM of the CNN classifier architecture with dropout for offline Arabic handwritten recognition. *Procedia Comput. Sci.* **2016**, *80*, 1712–1723, doi:10.1016/j.procs.2016.05.512.

90. Matsuyama, E.; Tsai, D.-Y. Automated Classification of Lung Diseases in Computed Tomography Images Using a Wavelet Based Convolutional Neural Network. *J. Biomed. Sci. Eng.* **2018**, *11*, 263–274, doi:10.4236/jbise.2018.1110022.

91. Teikari, P.; Santos, M.; Poon, C.; Hynynen, K. Deep Learning Convolutional Networks for Multiphoton Microscopy Vasculature Segmentation. **2016**.

92. Pauly, L.; Peel, H.; Luo, S.; Hogg, D.; Fuentes, R. Deeper Networks for Pavement Crack Detection. *Proc. 34th Int. Symp. Autom. Robot. Constr.* **2017**, doi:10.22260/isarc2017/0066.

93. Soriano, D.; Aguilar, C.; Ramirez, M. I.; Tusa, E.; Rivas, W.; Pinta, M. Mammogram Classification Schemes by Using Convolutional Neural Networks. **2018**, *798*, 71–85, doi:10.1007/978-3-319-72727-1.

94. Endice, F. D. Improving the Performance of Hyperspectral Pushbroom Imaging Spectrometers for Specific Science Applications. *Archives* 215–220.

95. Bron, A.; Evans, V. E.; Smith, J. A. Grading of corneal and conjunctival staining in the context of other dry eye tests. *Cornea* **2003**, 1–5.

96. Chun, Y. S.; Yoon, W. B.; Kim, K. G.; Park, I. K. Objective Assessment of Corneal Staining Using Digital Image Analysis. *Invest. Ophthalmol. Vis. Sci.* **2014**, *55*, 7896–7903, doi:10.1167/iovs.14-15618.

97. Khandelwal, A. Hyperspectral Image Enhancement Based on Sensor Simulation and Vector Decomposition. **2011**, 1234–1239.

98. Md Noor, S. S.; Md Tahir, N. Fusion of license plate and face recognition for secure parking. *J. Teknol. (Sciences Eng.* **2013**, *61*, 21–29, doi:10.11113/jt.v61.1618.

99. Wang, B.; Wang, X.; Chen, Z. Spatial entropy based mutual information in hyperspectral band selection for supervised classification. *Int. J. Numer. Anal. Model.* **2012**, *9*, 181–192.

100. Baumgardner, M. F., Biehl, L. L., Landgrebe, D. A. 220 Band AVIRIS Hyperspectral Image Data Set: June 12, 1992 Indian Pine Test Site 3. *Purdue Univ. Res. Repos.* **2015**, doi:10.4231/R7RX991C.

101. Fu, W.; Li, S.; Fang, L.; Jon, A. B. Contextual Online Dictionary Learning for Hyperspectral Image Classification. *IEEE Trans. Geosci. Remote Sens.* **2017**, *56*, 1–12, doi:10.1109/TGRS.2017.2761893.

102. Esteva, A.; Kuprel, B.; Novoa, R. A.; Ko, J.; Swetter, S. M.; Blau, H. M.; Thrun, S. Dermatologist-level classification of skin cancer with deep neural networks. *Nature* **2017**, *542*, 115–118, doi:10.1038/nature21056.

103. Lu, D.; Weng, Q. A survey of image classification methods and techniques for improving classification performance. *Int. J. Remote Sens.* **2007**, *28*, 823–870, doi:10.1080/01431160600746456.

104. Cihlar, J.; Xiao, Q.; Chen, J.; Beaubien, J.; Fung, K.; Latifovic, R. Classification by progressive generalization: A new automated methodology for remote sensing multichannel data. *Int. J. Remote Sens.* **1998**, *19*, 2685–2704, doi:10.1080/014311698214451.

105. Malik, F.; Baharudin, B. Analysis of distance metrics in content-based image retrieval using statistical quantized histogram texture features in the DCT domain. *J. King Saud Univ. Inf. Sci.* **2013**, *25*, 207–218, doi:10.1016/j.jksuci.2012.11.004.

106. Selvarajah, S.; Kodituwakku, S. R. Analysis and Comparison of Texture Features for Content Based Image Retrieval. *Int. J. Latest Trends Comput.* **2011**, *2*, 108–113.

107. Aggarwal, N.; Agrawal, R. K. First and Second Order Statistics Features for Classification of Magnetic Resonance Brain Images. *J. Signal Inf. Process.* **2012**, *03*, 146–153, doi:10.4236/jsip.2012.32019.

108. Fawcett, T. ROC Graphs: Notes and Practical Considerations for Data Mining Researchers ROC Graphs : Notes and Practical Considerations for Data Mining Researchers. *HP Inven.* **2003**, 27, doi:10.1.1.10.9777.

109. Bettinger, R. Cost-sensitive classifier selection using the ROC convex hull method. *SAS Inst.* **2003**, 1–12.

110. Zulpe, N. S. Statistical Approach for MRI Brain Tumor Quantification. *Int. J. Comput. Appl.* **2011**, *35*, 13–16.

111. Khan, S.; Yong, S. P. A comparison of deep learning and hand crafted features in medical image modality classification. *2016 3rd Int. Conf. Comput. Inf. Sci. ICCOINS 2016 - Proc.* **2016**, 633–638, doi:10.1109/ICCOINS.2016.7783289.

112. Sargano, A.; Angelov, P.; Habib, Z. A Comprehensive Review on Handcrafted and Learning-Based Action Representation Approaches for Human Activity

Recognition. *Appl. Sci.* **2017**, *7*, 110, doi:10.3390/app7010110.

113. Nanni, L.; Ghidoni, S.; Brahnam, S. Handcrafted vs. non-handcrafted features for computer vision classification. *Pattern Recognit.* **2017**, *71*, 158–172, doi:10.1016/j.patcog.2017.05.025.

114. Gómez-Chova, L.; Muñoz-Marí, J.; Laparra, V.; Malo-López, J.; Camps-Valls, G. *A Review of Kernel Methods in Remote Sensing Data Analysis*; 2011; ISBN 3496354402.

115. Rondina, J. M.; Ferreira, L. K.; de Souza Duran, F. L.; Kubo, R.; Ono, C. R.; Leite, C. C.; Smid, J.; Nitrini, R.; Buchpiguel, C. A.; Busatto, G. F. Selecting the most relevant brain regions to discriminate Alzheimer's disease patients from healthy controls using multiple kernel learning: A comparison across functional and structural imaging modalities and atlases. *NeuroImage Clin.* **2018**, *17*, 628–641, doi:10.1016/j.nicl.2017.10.026.

116. Manik, V.; Bodla, R. B. More generality in efficient multiple kernel learning. *Proc. 26th Annu. Int. Conf. Mach. Learn. - ICML '09* **2009**, *2009*, 1–8, doi:10.1145/1553374.1553510.

117. Fu, Z.; Robles-Kelly, A.; Zhou, J. Mixing linear SVMs for nonlinear classification. *IEEE Trans. Neural Networks* **2010**, *21*, 1963–1975, doi:10.1109/TNN.2010.2080319.

118. Cheng, K.; Lu, Z.; Wei, Y.; Shi, Y.; Zhou, Y. Mixed kernel function support vector regression for global sensitivity analysis. *Mech. Syst. Signal Process.* **2017**, *96*, 201–214, doi:10.1016/j.ymssp.2017.04.014.

119. Huanrui, H. New Mixed Kernel Functions of SVM Used in Pattern Recognition. *Cybern. Inf. Technol.* **2016**, *16*, 5–14, doi:10.1515/cait-2016-0047.

120. Zhongda, T.; Shujiang, L.; Yanhong, W.; Xiangdong, W. Mixed-kernel least square support vector machine predictive control based on improved free search algorithm for nonlinear systems. *Trans. Inst. Meas. Control* **2018**, doi:10.1177/0142331217748193.

121. Bergstra, J.; Bengio, Y. Random Search for Hyper-Parameter Optimization. *J. Mach. Learn. Res.* **2012**, *13*, 281–305, doi:10.1162/153244303322533223.

122. Tang, S.; Ke, F.; Hao, C. Kernel Support Vector Machine based on Convex Optimization and Applications. **2017**, *55*, 605–611.

123. Lin, Z.; Yan, L. A support vector machine classifier based on a new kernel function model for hyperspectral data. *GIScience Remote Sens.* **2016**, *53*, 85–101, doi:10.1080/15481603.2015.1114199.

124. Smits, G. F.; Jordaan, E. M. Improved SVM regression using mixtures of kernels. *Proc. 2002 Int. Jt. Conf. Neural Networks. IJCNN'02* **2002**, *3*, 2785–2790, doi:10.1109/IJCNN.2002.1007589.

125. Clarke, F. Functional Analysis, Calculus of Variations and Optimal Control. **2013**, *264*, 27–47, doi:10.1007/978-1-4471-4820-3.

126. Dheeru, D.; Karra, T. UCI Machine Learning Repository Available online: http://archive.ics.uci.edu/ml.

127. MIT Critical Data Secondary Analysis of Electronic Health Records. In; 2016; pp. 163–183 ISBN 978-3-319-43740-8.

128. Chambrier, A. G. De; Figueroa, N.; Lamotte, D. Advanced Machine Learning Practical 3 : Classification (SVM , RVM & AdaBoost).

129. Dioş, L.; Oltean, M.; Rogozan, A.; Pecuchet, J.-P. Improving SVM Performance Using a Linear Combination of Kernels. *Adapt. Nat. Comput. Algorithms* **2007**, 218–227, doi:10.1007/978-3-540-71629-7_25.

130. Lecun, Y.; Bengio, Y.; Hinton, G. Deep learning. *Nature* **2015**, *521*, 436–444, doi:10.1038/nature14539.

PUBLICATIONS BY THE AUTHOR

Below is a list of papers which have resulted from the work that has been described in this thesis:

1. Noor, S. S. M.; Michael, K.; Marshall, S.; Ren, J, "Spatial and spectral analysis of corneal epithelium injury using hyperspectral images," Proc. SPIE 10613, **2017** International Conference on Robotics and Machine Vision, 106130A (19 December 2017);

2. Noor, S. S. M.; Michael, K.; Marshall, S.; Ren, J. Hyperspectral image enhancement and mixture deep-learning classification of corneal epithelium injuries. *Sensors (Switzerland)* **2017**, *17*, doi:10.3390/s17112644.

3. Michael, K.; Noor, S. S. M.; Marshall, S.; Ren, J.; Tschannerl, 'The Properties of the Cornea Based on Hyperspectral Imaging'. Investigative Ophthalmology and Visual Science (**2017**), vol. 58, no. 8, 2439. Baltimore, Maryland. Published in ARVO journal – Abstract.

4. Noor, S. S. M.; Michael, K.; Marshall, S.; Ren, J.; Tschannerl, J.; Kao, F. J. The properties of the cornea based on hyperspectral imaging: Optical biomedical engineering perspective. *Int. Conf. Syst. Signals, Image Process.* **2016**, *2016–June*, 4–7, doi:10.1109/IWSSIP.2016.7502710.